CR160111

(NASA-CR-160111) SHUTTLE GLOBAL POSITIONING SYSTEM (GPS) SYSTEM DESIGN STUDY Final Report (Axiomatix, Los Angeles, Calif.) 180 p HC A09/MF A01 CSCL 17G

N79-17903

Unclas
G3/16 14179

Axiomatix

SHUTTLE GLOBAL POSITIONING SYSTEM (GPS) SYSTEM DESIGN STUDY

FINAL REPORT

Contract No. NAS 9-15387C

Prepared for

NASA Lyndon B. Johnson Space Center
Houston, Texas 77058

Prepared by

Peter W. Nilsen

Contributions by

Nagwa Bakir
Gaylord K. Huth
Marvin K. Simon
Sergei Udalov

Axiomatix
9841 Airport Boulevard, Suite 912
Los Angeles, California 90045

Axiomatix Report No. R7901-4
January 20, 1979

TABLE OF CONTENTS

Appendix

LIST OF TABLES

LIST OF FIGURES

Page

Page

1.0 INTRODUCTION AND SUMMARY

This report documents the analyses and investigations performed by Axiomatix under Contract NAS 9-15387C for NASA Johnson Space Center. This report and its companion report performed under Contract NAS 9-15387B present the results of work performed to analyze areas of a GPS navigation system to be implemented on the Shuttle that would have the greatest impact on performance. Also, this report presents results of the investigation of the integration problems. The various aspects of GPS receiver design trade-offs that were evaluated as part of the analyses and investigations are included in this report.

The analysis of the Shuttle/GPS link is of foremost importance. It is necessary to demonstrate a sufficiently high signal-to-noise ratio for this link at this pont in time so that a high degree of confidence can be established for meeting performance requirements when the flight system is implemented. The approximately 3 dB of minimum margin found in the link analysis satisfies this goal.

Since the Shuttle GPS antennas must be located remotely from the receiver, a preamplifier is necessary. This preamplifier determines the system noise temperature and thus strongly influences the link margin. Consequently, trade-offs and performance for Shuttle GPS application has been investigated. Furthermore, performance of the system as influenced by redundancy switching considerations has been analyzed.

A discussion of several GPS receiver architecture trade-offs is presented. The discussion is centered on the sequential receiver, which is recommended as the baseline receiver architecture. Three receiver frequency conversion plans are discussed and double conversion is highlighted as an attractive choice.

The Shuttle GPS system must operate in a complex RF environment, in which several on-board RF emitters may operate simultaneously. Consequently, and RFI/EMI analysis has been performed which evaluates the Shuttle RF harmonics and intermods that fall within the GPS receiver bandwidth. The analysis shows that no serious RFI/EMI problems exist. An analysis of TACAN/GPS EMC has shown that 28 dB of isolation between the TACAN antenna and the GPS antenna is desirable. It is pointed out that if the requirement for ionospheric delay correction is relaxed, the isolation can be smaller since only the L2 frequency is affected. Operational procedures can also relax the isolation requirement.

The GPS PN code acquisition has been analyzed extensively. This analysis has used the results of the link budget analysis to optimize the type of acquisition technique (sequential) and to optimize the receiver parameters such as bandwidth and threshold that affect the acquisition time.

The GPS signal carrier must be acquired for data detection and pseudo range rate measurements. In the low GPS signal level environment of the Shuttle, it is important that the receiver processing be optimized for fast carrier acquisition. A technique for potentially improving the carrier acquisition performance for the Shuttle GPS is presented and analyzed in detail. An improvement over conventional coherent receiver techniques is shown.

Since the receiver clock strongly affects both GPS carrier and code acquisition performance, a clock model has been developed and analyzed. This model is useful in specifying the performance for the Shuttle GPS receiver clock.

The Shuttle GPS system performance will, to a large extent, depend on elements of the overall GPS system beyond the control of NASA. For this reason, an interface control document (ICD) between NASA and the GPS Joint Program Office is necessary. A preliminary outline of this ICD is presented.

2.0 GPS/SHUTTLE LINK BUDGETS

Summary

The link budgets for the GPS satellite to the Space Shuttle (nominal orbit) have been calculated. Tables 1 through 12 are the detailed budgets for ranging, carrier tracking and data detection for L1 and L2 frequencies and P and C/A codes. In general, the parameter values are either worst-case specified values, best engineering predictions based on breadboard measurements, or survey of available equipment or components. The system effective noise temperature is discussed in detail below but, since it is so strongly influenced by preamp performance, Section 3.0 has been devoted to preamplifier design and analysis.

The link margins are summarized in Table 13. In general, the in-atmosphere performance should be essentially the same since the SS-GPS-2000 System Specification for the NAVSTAR Global Positioning System specifies L1 and L2 signal levels at the earth's surface of -163 and -166 dBW for a 0 dB circularly polarized antenna. These signal levels are within 0.4 dB of the GPS/Shuttle link for a -4 dB antenna gain. An explanation of some of the budget parameter values follows below.

Satellite EIRP

These values are for the edge of earth coverage as specified in the GPS Space Segment Specification CID-SV-10H. The actual performance of the two on-orbit spacecraft has been reported to be better than the specification values.

Space Loss

Two space loss numbers of -184.6 and -182.4 dB for L1 and L2, respectively, are based on the orbital geometry shown in Figure 1. From Figure 1, the line of sight (LOS) is given by:

$$R = 26{,}650 \cos \theta = 26{,}659 \cos \left[\sin^{-1} \frac{6698}{26{,}650} \right]$$

$$= 25{,}795 \text{ km}$$

The space loss is given by $L = 92.45 + 20 \log f \text{ (GHz)} + \log R \text{ (km)}$

$$= 92.45 + 20 \log 1.575 + 20 \log 25{,}795$$

$$= 184.6 \text{ dB}.$$

Table 1. Baseline Link Budget for Range Measurement, L1-P

Link L1-P, Range
Upper Antenna
Orbital Geometry: Path Tangential to Orbit

Parameter	Value	Explanation
Satellite EIRP	23.8 dBW	EOE, Spec. CID-SV-10H
Space Loss	-184.6 dB	Path Tangent to Orbit
Pointing Loss	- 0.4 dB	
Polarization Loss	- 0.4 dB	
Atmospheric Loss	0	
Shuttle Antenna Gain	- 4.0 dB	
Received Power	-165.6 dBW	At Antenna Terminals
System Noise Temperature	28.5 dBK	T_{sys} = 705°K (at antenna terminals)
Boltzmann's Constant	-228.6 dB-W/K/Hz	
Noise Spectral Density	-200.1 dB-W/Hz	
C/N_0	34.5 dB-Hz	
Required C/N_0 (Theoretical)	29.6 dB-Hz	$\sigma_{Range} = 5'$
Implementation Loss	2.0 dB	
Required C/N_0	31.6 dB-Hz	
Link Margin	2.9 dB	

Table 2. Baseline Link Budget for Range Measurement, L1-C/A

Link L1-C/A, Range
Upper Antenna
Orbital Geometry: Path Tangential to Orbit

Parameter	Value	Explanation
Satellite EIRP	26.8 dBW	EOE, Spec. CID-SV-10H
Space Loss	-184.6 dB	Path Tangent to Orbit
Pointing Loss	- 0.4 dB	
Polarization Loss	- 0.4 dB	
Atmospheric Loss	0	
Shuttle Antenna Gain	- 4.0 dB	
Received Power	-162.6 dBW	At Antenna Terminals
System Noise Temperature	28.5 dBK	T_{sys} = 705°K (at antenna terminals)
Boltzmann's Constant	-228.6 dB-W/K/Hz	
Noise Spectral Density	-200.1 dB-W/Hz	
C/N_0	37.5 dB-Hz	
Required C/N_0 (Theoretical)	29.6 dB-Hz	σ_{Range} = 50'
Implementation Loss	2.0 dB	
Required C/N_0	31.6 dB-Hz	
Link Margin	5.9 dB	

Table 3. Baseline Link Budget for Range Measurement, L2-P

Link L2-P, Range
Upper Antenna
Orbital Geometry: Path Tangential to Orbit

Parameter	Value	Explanation
Satellite EIRP	19.1 dBW	EOE, Spec. CID-SV-10H
Space Loss	-182.4 dB	Path Tangent to Orbit
Pointing Loss	- 0.4 dB	
Polarization Loss	- 0.4 dB	
Atmospheric Loss	0	
Shuttle Antenna Gain	- 4.0 dB	
Received Power	-168.1 dBW	At Antenna Terminals
System Noise Temperature	28.5 dBK	T_{sys} = 705°K (at antenna terminals)
Boltzmann's Constant	-228.6 dB-W/K/Hz	
Noise Spectral Density	-200.1 dB/W/Hz	
C/N_0	32.0 dB-Hz	
Required C/N_0 (Theoretical)	27.5 dB-Hz	σ_{Range} = 7'
Implementation Loss	2.0 dB	
Required C/N_0	29.5 dB	
Link Margin	2.5 dB	

Table 4. Baseline Link Budget for Range Measurement, L2-C/A

Link L2-C/A, Range
Upper Antenna
Orbital Geometry: Path Tangential to Orbit

Parameter	Value	Explanation
Satellite EIRP	19.1 dBW	EOE, Spec. CID-SV-10H
Space Loss	-182.4 dB	Path Tangent to Orbit
Pointing Loss	- 0.4 dB	
Polarization Loss	- 0.4 dB	
Atmospheric Loss	0	
Shuttle Antenna Gain	- 4.0 dB	
Received Power	-168.1 dBW	At Antenna Terminals
System Noise Temperature	28.5 dBK	T_{sys} = 705°K (at antenna terminals)
Boltzmann's Constant	-228.6 dB-W/K/Hz	
Noise Spectral Density	-200.1 dB-W/Hz	
C/N_0	32.0 dB-Hz	
Required C/N_0 (Theoretical)	27.5 dB-Hz	σ_{Range} = 70'
Implementation Loss	2.0 dB	
Required C/N_0	29.5 dB-Hz	
Link Margin	2.5 dB	

Table 5. Baseline Link Budget for Carrier Tracking, L1-P

Link L1-P, Carrier
Upper Antenna
Orbital Geometry: Path Tangential to Orbit

Parameter	Value	Explanation
Satellite EIRP	23.8 dBW	EOE, Spec. CID-SV-10H
Space Loss	-184.6 dB	Path Tangent to Orbit
Pointing Loss	- 0.4 dB	
Polarization Loss	- 0.4 dB	
Atmospheric Loss	0	
Shuttle Antenna Gain	- 4.0 dB	
Received Power	-165.6 dBW	At Antenna Terminals
System Noise Temperature	28.5 dBK	T_{sys} = 705°K (at antenna terminals)
Boltzmann's Constant	-228.6 dB-W/K/Hz	
Noise Spectral Density	-200.1 dB-W/Hz	
C/N_0	34.5 dB-Hz	
Required C/N_0 (Theoretical)	28.5 dB-Hz	σ_{Jitter} = 15°
Implementation Loss	1.5 dB	
Required C/N_0	29.5 dB-Hz	
Link Margin	5.0 dB	

Table 6. Baseline Link Budget for Carrier Tracking, L1-C/A

Link L1-C/A, Carrier
Upper Antenna
Orbital Geometry: Path Tangential to Orbit

Parameter	Value	Explanation
Satellite EIRP	26.8 dBW	EOE, Spec, CID-SV-10H
Space Loss	-184.6 dB	Path Tangent to Orbit
Pointing Loss	- 0.4 dB	
Polarization Loss	- 0.4 dB	
Atmospheric Loss	0	
Shuttle Antenna Gain	- 4.0 dB	
Received Power	-162.6 dBW	At Antenna Terminals
System Noise Temperature	28.5 dBK	T_{sys} = 70°K (at antenna terminals)
Boltzmann's Constant	-228.6 dB-W/K/Hz	
Noise Spectral Density	-200.1 dB-W/Hz	
C/N_0	37.5 dB-Hz	
Required C/N_0 (Theoretical)	28.0 dB-Hz	$\sigma_{Jitter} = 15°$
Implementation Loss	1.5 dB	
Required C/N_0	29.5 dB-Hz	
Link Margin	8.0 dB	

Table 7. Baseline Link Budget for Carrier Tracking, L2-P

Link L2-P, Carrier
Upper Antenna
Orbital Geometry: Path Tangential to Orbit

Parameter	Value	Explanation
Satellite EIRP	19.1 dBW	EOE, Spec. CID-SV-10H
Space Loss	-182.4 dB	Path Tangent to Orbit
Pointing Loss	- 0.4 dB	
Polarization Loss	- 0.4 dB	
Atmospheric Loss	0	
Shuttle Antenna Gain	- 4.0 dB	
Received Power	-168.1 dBW	
System Noise Temperature	28.5 dBK	T_{sys} = 705°K (at antenna terminals)
Boltzmann's Constant	-228.6 dB-W/K/Hz	
Noise Spectral Density	-200.1 dB-W/Hz	
C/N_0	32.0 dB-Hz	
Required C/N_0 (Theoretical)	28.0 dB-Hz	σ_{Jitter} = 15°
Implementation Loss	1.5 dB	
Required C/N_0	29.5 dB-Hz	
Link Margin	2.5 dB	

Table 8. Baseline Link Budget for Carrier Tracking, L2-C/A

Link L2-C/A, Carrier
Upper Antenna
Orbital Geometry: Path Tangential to Orbit

Parameter	Value	Explanation
Satellite EIRP	19.1 dBW	EOE, Spec. CID-SV-10H
Space Loss	-182.4 dB	Path Tangent to Orbit
Pointing Loss	- 0.4 dB	
Polarization Loss	- 0.4 dB	
Atmospheric Loss	0	
Shuttle Antenna Gain	- 4.0 dB	
Received Power	-168.1 dBW	
System Noise Temperature	28.5 dBK	T_{sys} = 705°K (at antenna terminals)
Boltzmann's Constant	-228.6 dB/W/K/Hz	
Noise Spectral Density	-200.1 dB-W/Hz	
C/N_0	32.0 dB-Hz	
Required C/N_0 (Theoretical)	28.0 dB-Hz	$\sigma_{Jitter} = 15°$
Implementation Loss	1.5 dB	
Required C/N_0	29.5 dB-Hz	
Link Margin	2.5 dB	

Table 9. Baseline Link Budget for Data Detection, L1-P

Link L1-P, Data Detection
Upper Antenna
Orbital Geometry: Path Tangential to Orbit

Parameter	Value	Explanation
Satellite EIRP	23.8 dBW	EOE, Spec. CID-SV-10H
Space Loss	-184.5 dB	Path Tangent to Orbit
Pointing Loss	- 0.4 dB	
Polarization Loss	- 0.4 dB	
Atmospheric Loss	0	
Shuttle Antenna Gain	- 4.0 dB	
Received Power	-165.6 dBW	At Antenna Terminals
System Noise Temperature	28.5 dBK	T_{sys} = 705°K (at antenna terminals)
Boltzmann's Constant	-228.6 dB-W/K/Hz	
Noise Spectral Density	-200.1 dB-W/Hz	
C/N_0	34.5 dB-Hz	
Required C/N_0 (Theoretical)	26.6 dB-Hz	BER = 10^{-5}
Implementation Loss	2.0 dB	
Required C/N_0	28.6 dB	
Link Margin	5.9 dB	

Table 10. Baseline Link Budget for Data Detection, L1-C/A

Link L1-C/A, Data Detection
Upper Antenna
Orbital Geometry: Path Tangential to Orbit

Parameter	Value	Explanation
Satellite EIRP	26.8 dBW	EOE, Spec. CID-SV-10H
Space Loss	-184.6 dB	
Pointing Loss	- 0.4 dB	
Polarization Loss	- 0.4 dB	
Atmospheric Loss	0	
Shuttle Antenna Gain	- 4.0 dB	
Received Power	-162.6 dBW	At Antenna Terminals
System Noise Temperature	28.5 dBK	T_{sys} = 705°K (at antenna terminals)
Boltzmann's Constant	-228.6 dB-W/K/Hz	
Noise Spectral Density	-200.1 dB-W/Hz	
C/N_0	37.5 dB-Hz	
Required C/N_0 (Theoretical)	26.6 dB-Hz	BER = 10^{-5}
Implementation Loss	2.0 dB	
Required C/N_0	28.6 dB-Hz	
Link Margin	8.9 dB	

Table 11. Baseline Link Budget for Data Detection, L2-P

Link L2-P, Data Detection
Upper Antenna
Orbital Geometry: Path Tangential to Orbit

Parameter	Value	Explanation
Satellite EIRP	19.1 dBW	EOE, Spec. CID-SV-10H
Space Loss	-182.4 dB	Path Tangent to Orbit
Pointing Loss	- 0.4 dB	
Polarization Loss	- 0.4 dB	
Atmospheric Loss	0	
Shuttle Antenna Gain	- 4.0 dB	
Received Power	-168.1 dBW	At Antenna Terminals
System Noise Temperature	28.5 dBK	T_{sys} = 705°K (at antenna terminals)
Boltzmann's Constant	-228.6 dB-W/K/Hz	
Noise Spectral Density	-200.1 dB-W/Hz	
C/N_0	32.0 dB-Hz	
Required C/N_0 (Theoretical)	26.6 dB-Hz	BER = 10^{-5}
Implementation Loss	2.0 dB	
Required C/N_0	28.6 dB-Hz	
Link Margin	3.4 dB	

Table 12. Baselink Link Budget for Data Detection, L2-C/A

Link L2-C/A, Data Detection
Upper Antenna
Orbital Geometry: Path Tangential to Orbit

Parameter	Value	Explanation
Satellite EIRP	19.1 dBW	EOE, Spec. CID-SV-10H
Space Loss	-182.4 dB	Path Tangent to Orbit
Pointing Loss	- 0.4 dB	
Polarization Loss	- 0.4 dB	
Atmospheric Loss	0	
Shuttle Antenna Gain	- 4.0 dB	
Received Power	-168.1 dBW	At Antenna Terminals
System Noise Temperature	28.5 dBK	T_{sys} = 705°K (at antenna terminals)
Boltzmann's Constant	-228.6 dB-W/K/Hz	
Noise Spectral Density	-200.1 dB-W/Hz	
C/N_0	32.0 dB-Hz	
Required C/N_0 (Theoretical)	26.6 dB-Hz	BER = 10^{-5}
Implementation Loss	2.0 dB	
Required C/N_0	28.6 dB-Hz	
Link Margin	3.4 dB	

Table 13. Baseline System Configuration, On-Orbit Link Margin Summary

Link		Link Margin by Function Ranging (dB)	 Carrier (dB)	 Data (dB)
Lower Antenna*				
L1	P	3.3	5.4	6.3
	C/A	6.3	8.4	9.3
L2	P	2.9	2.9	3.8
	C/A	2.9	2.9	3.8
Upper Antenna				
L1	P	2.9	5.0	5.9
	C/A	5.9	8.0	8.9
L2	P	2.5	2.5	3.4
	C/A	2.5	2.5	3.4

*OV102 lower antenna margins are 1.3 dB lower.

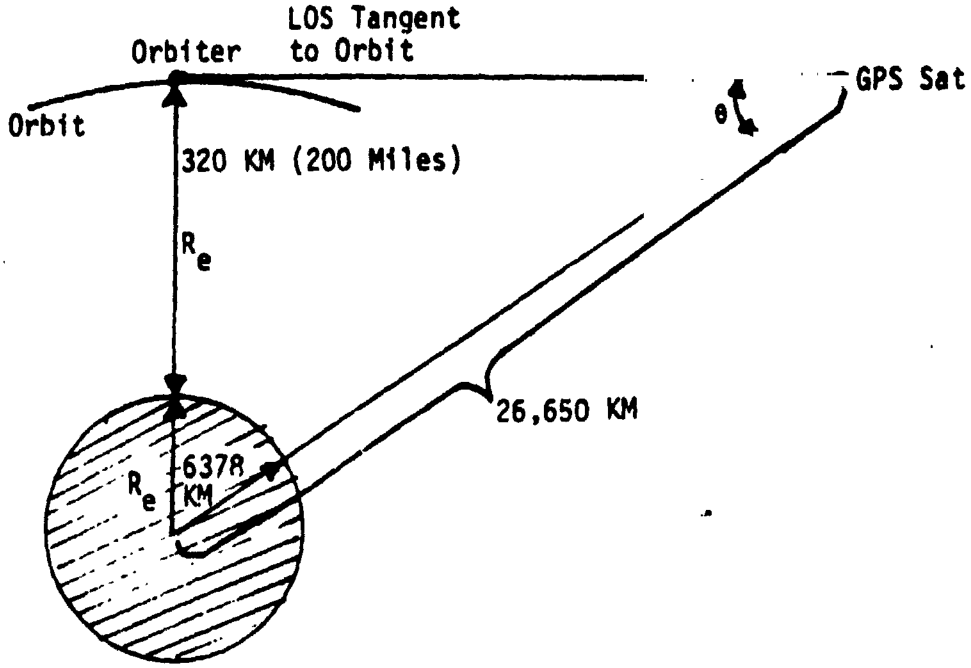

Figure 1. Geometry for Shuttle/GPS Link Space Loss Calculation

This geometry, called LOS tangent-to-orbit, is considered a nominal baseline case. Some links, such as the overhead viewing links, will have less space loss; and other links, such as those where the Orbiter may be in higher orbits and viewing tangent to the earth (or earth's atmosphere), will have greater loss.

Pointing Loss

The pointing loss value of -0.4 dB occurs because the GPS satellite antenna coverage is designed to provide maximum radiated power at the edge of the earth. Since the Orbiter is some 200 miles above the edge of the earth, there is a reduction in EIRP. The GPS satellite antenna pattern for FSV #1 has a gain slope of approximately 0.5 dB/degree. From Figure 2, the angle seen by the GPS satellite antenna is 0.72 degree for the 200-mile Shuttle orbit. Thus, the EIRP loss is equal to 0.5 dB/degree x 0.72 degree ≈ 0.4 dB.

Polarization Loss

The polarization loss occurs because the GPS antenna and the Orbiter GPS antenna are not perfectly circular-polarized. GPS satellite antenna test data indicates an axial ratio of approximately 1.2 dB at the edge of the earth. Assuming a Shuttle antenna axial ratio of 4 dB and referring to Figure 3, which gives polarization loss between two elliptically polarized antennas, the loss is seen to be approximately 0.4 dB.

Antenna Gain

The -4 dB gain is with respect to perfect RHCP and has been chosen by Rockwell to give the desired angular coverage. It is based on breadboard antenna measurements and is subject to change. It should be noted that a decrease in overall actual antenna gain can translate into a decrease in antenna coverage volume rather than a decrease in link margin.

Circuit Loss

The circuit losses used for the link budget calculations have been provided by Rockwell and are given in Table 14. Two types of losses are given: the loss from the antenna to the preamplifier and the loss from the preamplifier to the receiver. The latter loss includes a 6 dB power splitting loss for adding a third-string receiver. Even though the baseline design is a two-string system, it is cost effective to install and

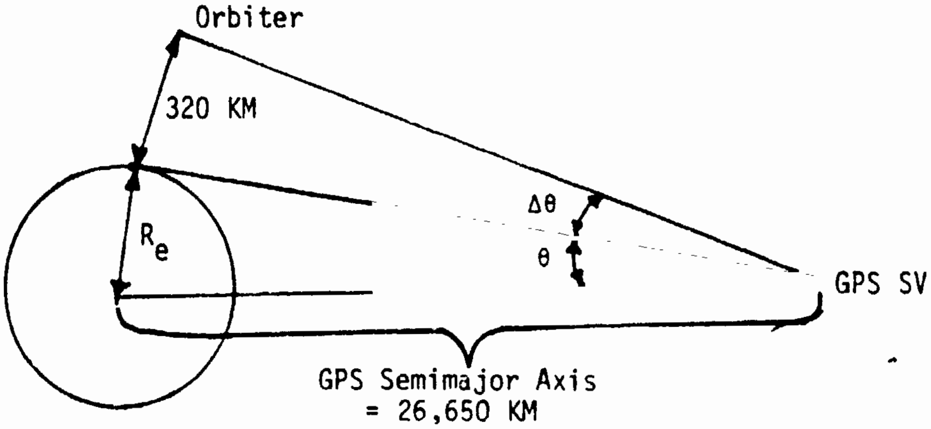

$$\Delta\theta = \tan^{-1}\left[\frac{320 \tan\theta}{R_e}\right]$$

$$\theta = \sin^{-1}[R_e/26{,}650]$$

$$\Delta\theta \cong .72 \text{ deg}$$

Figure 2. Derivation of Off Axis Pointing Error for Orbiter in 200 Mile Orbit

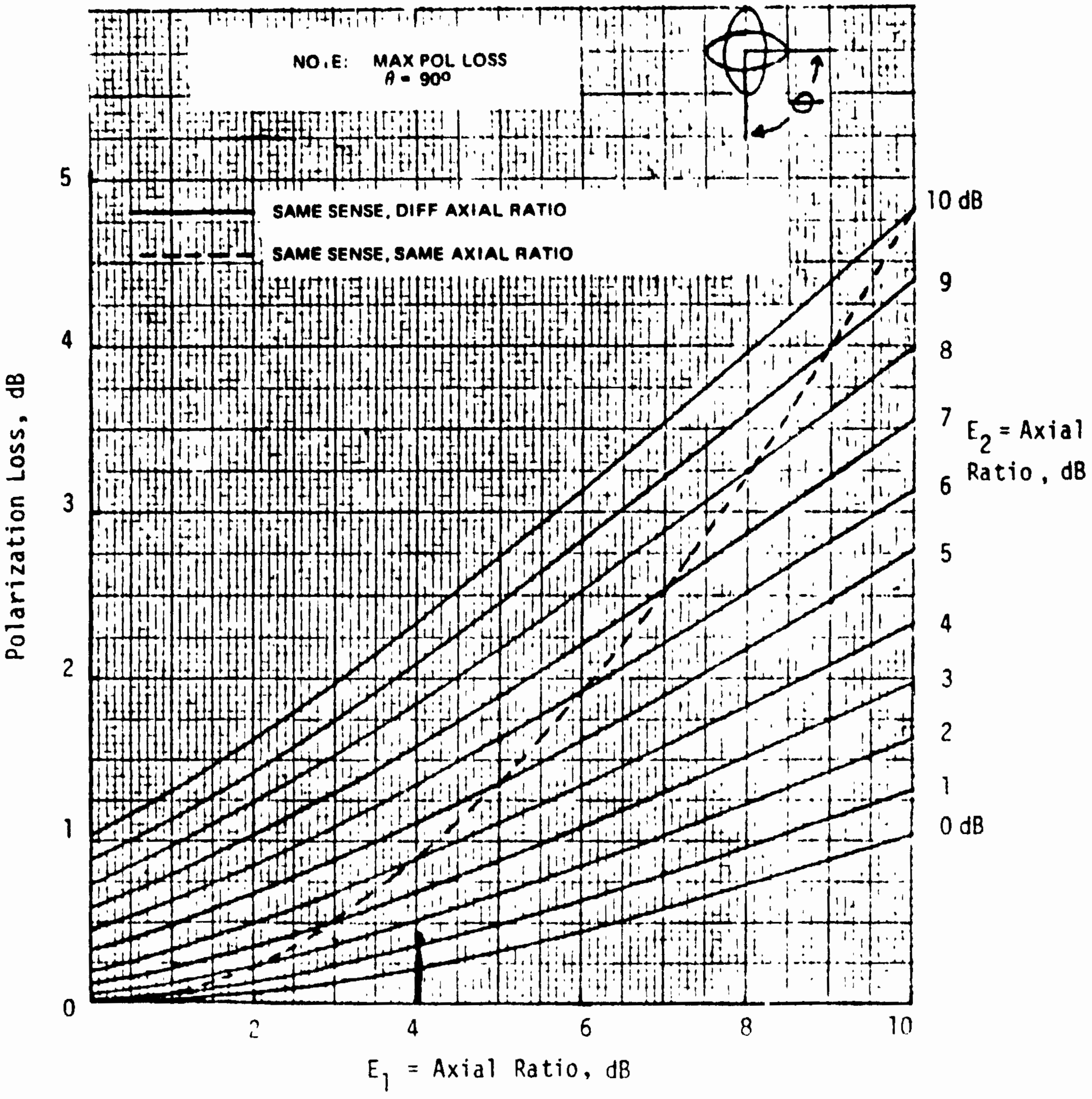

Figure 3. Polarization Loss Between Two Elliptically Polarized Antennas

connect the necessary power splitters for a three-string system.

Circuit Antenna	Antenna Circuit (L_1) (dB)	PA/RPA Circuit (L_2) (dB)
Upper Antenna	1.66	11.22
Lower Antenna	1.36	11.88
(OV 102)	(2.42)	(11.88)

Table 14. RF Circuit Loss

System Noise Temperature

The signal-to-noise ratio required for all GPS receiver processing functions is proportional to C/kT_e (C/N_0) where C is the available signal power, k is Boltzmann's constant, and T_e is the effective noise temperature. Since the Shuttle GPS receiving system is comprised of a cascade of elements, it is necessary to derive the effective noise temperature T_e for the desired point for definition of C/KT_e.

The Shuttle GPS system is modeled in the block diagram shown in Figure 4. As will be shown, it is inconsequential as to which point is picked as a reference point for definition of C/N_0 since the ratio is constant, i.e., independent of the point in the circuit. A generalized model of a cascaded system is used to illustrate this point. This model is shown in Figure 5. The effective noise temperature at the input to the cascade, T_e, is given by

$$T_e = T_1 + \frac{T_2}{G_1} + \frac{T_3}{G_1G_2} + \frac{T_4}{G_1G_2G_3} + \cdots$$

and the input signal power is C. Now, to find the system effective noise temperature at point ② , T_e', we note that noise at ② from the input to the first box will have been increased by the gain of this box, G_1. Thus,

$$\begin{aligned} T_e' &= G_1T_e \\ &= T_1G_1 + T_2 + \frac{T_3}{G_2} + \frac{T_4}{G_2G_3} + \cdots \end{aligned}$$

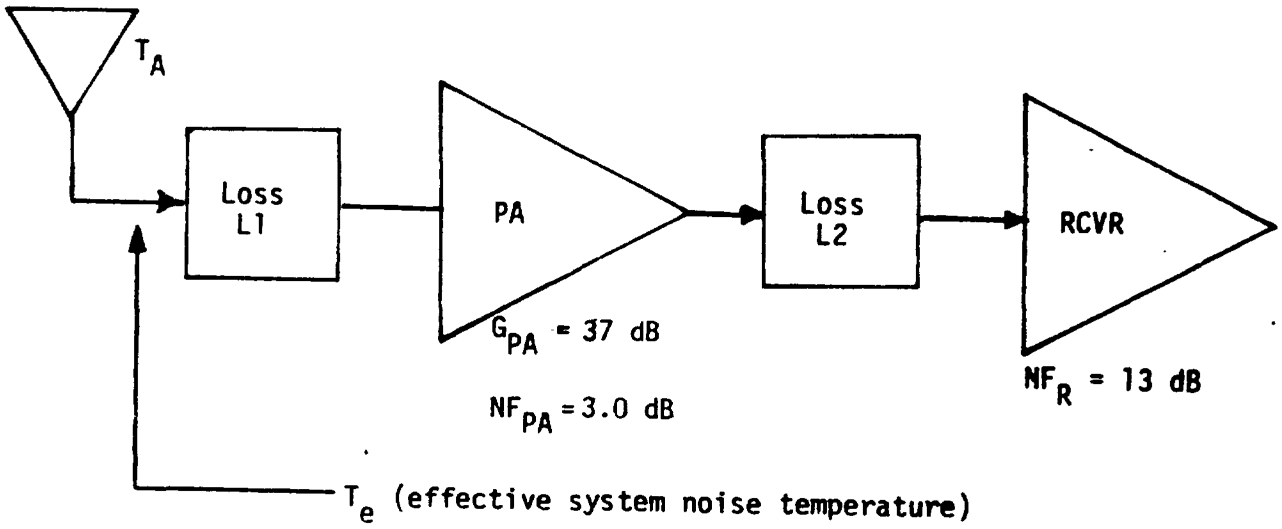

Figure 4. System Block Diagram for Calculation of System Noise Temperature

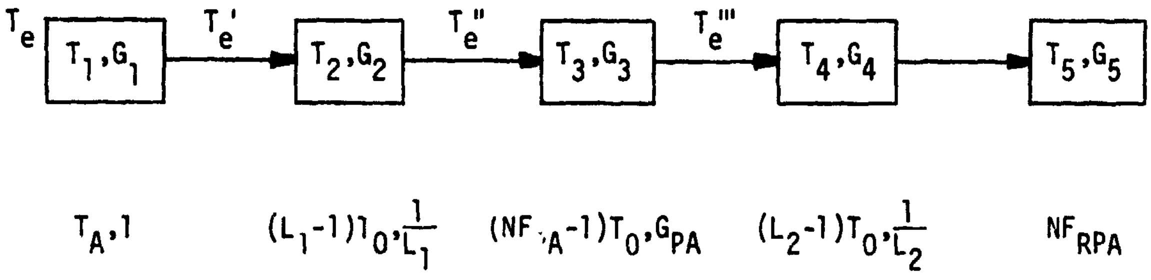

$$T_e = T_1 + \frac{T_2}{G_1} + \frac{T_3}{G_1G_2} + \frac{T_4}{G_1G_2G_3} + \cdots$$

$$T_e' = T_1G_1 + T_2 + \frac{T_3}{G_2} + \frac{T_4}{G_2G_3} + \cdots$$

Figure 5. General Mode of System Noise Temperature for Cascaded Elements

Similarly, the signal power at ② is increased by G_1 so that

$$C' = G_1 C$$

and the signal-to-noise ratio is given by

$$\frac{C'}{KT_e'} = \frac{G_1 C}{KG_1 T_e}$$

$$= \frac{C}{KT_e}$$

which, of course, is the same as the signal-to-noise ratio at the input to the cascade. The same reasoning can be applied to show that the signal-to-noise ratio at ③ is also the same by multiplying both signal and noise at ② by gain G_3. The noise temperature at ③ is given by

$$T_e'' = T_1 G_1 G_2 + T_2 G_2 + T_3 + \frac{T_4}{G_3} + \ldots$$

The generalized model of Figure 5 is now applied to the Shuttle GPS system. Box 1 is taken as the antenna with temperature T_A, box 2 is the loss between the antenna and preamp, L_1, box 3 is the preamp, box 4 is the loss between the preamp and the receiver, L_2, and box 5 is the receiver. The equivalent noise temperature of an active element of noise figure NF and gain G is given by

$$T = (NF-1)\ T_0$$

where T_0 is the reference temperature (290°K). The noise temperature of a passive element of loss L and gain G = 1/L is given by

$$T = (L-1)T_0$$

Thus the equivalent noise temperature of the GPS system at the antenna terminal (T_e') is given by

$$T = T_A + (L_1-1)T_0 + \frac{(NF_{PA}-1)T_0}{1/L_1} + \frac{(L_2-1)T_0}{1/L_1\ G_{PA}} + \frac{(NF_{RPA}-1)T_0}{1/L_1\ 1/L_2\ G_{PA}}$$

The system noise temperature and the signal power in the link budgets which follow are referenced to the GPS antenna terminals. Therefore, the system signal power-to-noise density ratio is written as

$$\frac{C}{N_0} = \frac{C}{kT_0\left[\frac{T_A}{T_0} + (L_1-1) + L_1(NF_{PA}-1) + L_1\,\frac{(L_1-1)}{G_{PA}} + \frac{L_1L_2(NF_{RPA}-1)}{G_{PA}}\right]}$$

The system equivalent noise temperatures for the GPS system have been calculated for the various antenna and loss combinations using the parameters

NF_{PA} = 3.0 dB
G_{PA} = 37 dB
NF_{RPA} = 13 dB
L_1, L_2 = values given in Table 14.

Table 15 presents a summary of the system equivalent noise temperatures, both in degrees kelvin and in dB-°K.

Table 15. Summary of Effective System Noise Temperature (at antenna terminals)

Antenna	Effective Temperature (includes antenna temperature = 125°K)	
	Degrees kelvin	dB-°K
Upper	705	28.5
Lower	650	28.1
(OV102)	876	29.4

It should be noted that OV102 lower antenna circuit noise is higher than the other two cases shown in Table 15 due to the diplexer loss as a result of sharing the antenna feed cable with the S-band antenna.

Required C/N_0 and Implementation Loss

The required C/N_0 for ranging is based on a range measurement accuracy of σ = 5 feet for L1-P and σ = 7 feet for L2-P. The L2 requirement is relaxed because L2 is needed only for ionospheric correction and its measurement is effectively averaged over several samples in the correction process. The derivation of the 29.6/27.5 dB, as well as the 2 dB implementation loss, is documented in [1]. In addition, the carrier tracking requirement of 28 dB is based on an allowable RMS phase jitter of 15°, and the data detection requirement of 26.6 dB is based on a 10^{-5} BER for the 50 bps data. These parameters are also documented in [1].

3.0 SHUTTLE GPS PREAMPLIFIFR DESIGN

The Shuttle GPS system requires an RF preamplifier mounted close to each antenna to control the overall system noise figure. This is due to the fact that there is a long length of feedline between each antenna and the GPS receiver processor assembly (RPA), in addition to other loss elements such as RF switches. An equivalent block diagram of this system is given in Figure 6. The equivalent noise temperature of the system, referenced to the input of the RPA is given by

$$T_{EF} = (L_1 - 1)T_0 + \frac{(NF_{PA} - 1)T_0}{1/L_1} + \frac{(L_2 - 1)T_0}{(1/L_1)G_{PA}} + \frac{(NF_{RPA} - 1)T_0}{(1/L_1L_2)G_{PA}} .$$

Thus, it is obvious that in addition to minimizing the antenna feed loss it is most important to minimize the preamp noise figure, NF_{PA}, while at the same time maximizing the gain so as to minimize the noise contributions of loss L_2 and the RPA front end.

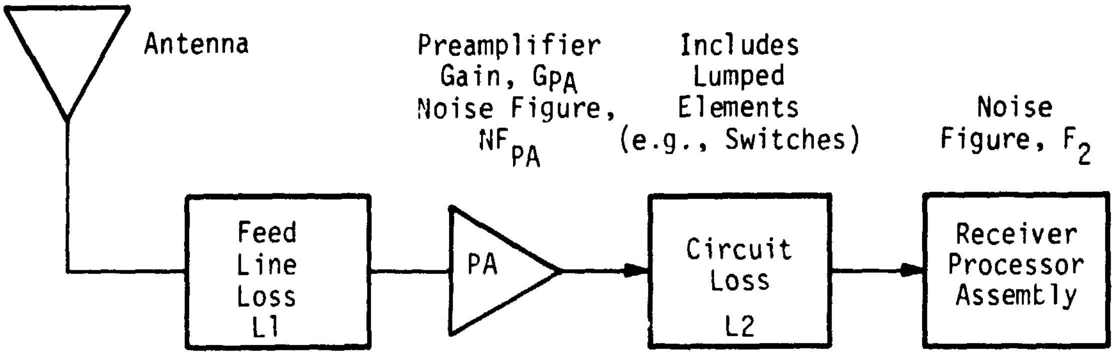

Figure 6. Model of GPS Receiving System for Calculation of Equivalent Noise Temperature

A recommended candidate Shuttle GPS preamplifier design is shown in block diagram form in Figure 7. Each of the elements in Figure 7 will be discussed for the purpose of evaluating the feasible performance for this GPS preamplifier. An alternate preamplifier configuration is shown in Figure 8. This configuration functionally performs the same; however, it does not offer the redundancy advantage that the configuration of Figure 7 offers. The advantage of Figure 8 is that it eliminates one

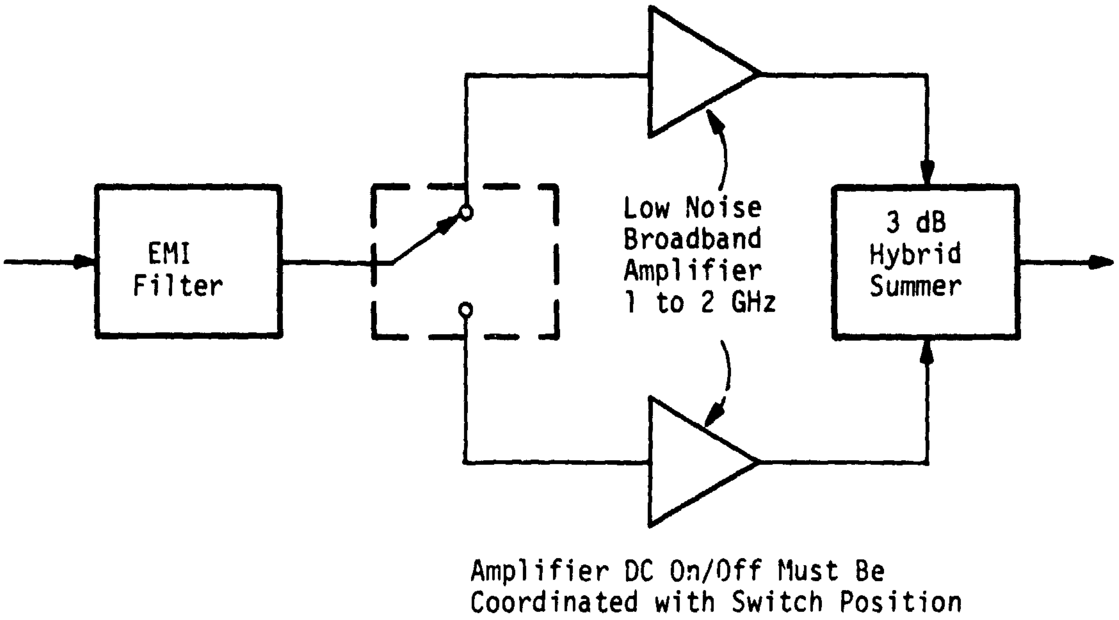

Figure 7. Recommended Redundant Preamplifier Configuration

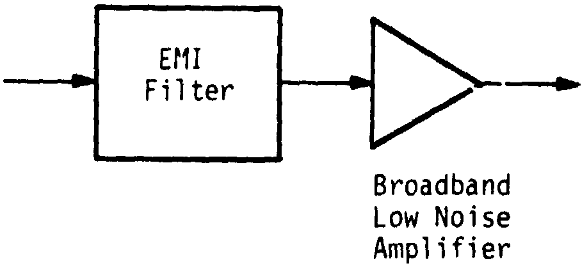

Figure 8. Recommended Nonredundant Preamplifier Configuration

amplifier, the switch, and the summer. The major disadvantage of the Figure 8 preamplifier configuration is the lack of redundancy. If the amplifier fails, the antenna to which the preamplifier is connected is no longer useable for the Shuttle GPS navigation system. Of course, in the case of the redundant preamplifier, if the antenna itself fails, the preamplifier redundancy is of no use in providing the signal reception. One argument, however, in favor of the redundant preamplifier configuration is that the MTBF of the antenna is several orders of magnitude greater than an active electronic circuit. This is the reason why communication satellites, and most scientific spacecraft, almost always use redundant transponders (and preamplifiers, when preamplifiers are used), even when there is a single antenna.

Yet another preamplifier configuration is shown in Figure 9. This is the configuration used in the Phase 1 GPS developmental receivers. It offers the advantage of dual redundancy without having to utilize a switch. The redundancy gained is not as powerful as the redundancy provided by the Figure 7 configuration, since in the case of Figure 9 one preamplifier channel is dedicated to the L1 frequency and the other channel is dedicated to the L2 frequency. Thus, a failure of one channel would constrain operation (with the associated antenna) to the unaffected frequency. A further drawback to this configuration is that the diplexer used to separate the L1/L2 channels adds significantly to the cost and size of the preamplifier.

The broadband amplifier shown in Figure 7 is the one element which most strongly determines the performance of the preamplifier. It is desirable for this amplifier to have as low a noise figure as possible, along with high gain, but consistent with reasonable cost. In order to determine reasonable performance specification requirements for the Shuttle GPS preamplifier, a survey has been taken of some of the off-the-shelf commercial low noise GaAs, FET, and bi-polar amplifiers. A summary of amplifier characteristics for amplifiers covering a wide frequency range is given in Table 16. The circled line represents the amplifier most closely satisfying the Shuttle GPS requirements. The two parameters of greatest significance are the noise figure of 2.5 dB and the 38 dB gain. It must be stressed that these values are the minimum values over the frequency range of the amplifier. Typical variation with frequency is illustrated in Figure 10. The preamplifier performance is not entirely determined by

Table 16. Typical Broadband Bi-Polar and GaAs FET Low Noise Amplifiers

FREQ. RANGE (MHz)	NOISE FIGURE (dB) MAX.	GAIN (dB) MIN.	P_0 (dBm) MIN @ 1 dB COMP	GAIN FLAT NESS (±dB)	INTERCEPT POINT (dBm) TYP	VSWR MAX IN	VSWR MAX OUT	DC POWER +15 VDC @ (mA)NOM
950-1250	2.2	24	+ 5	0.5	+16	2.0	1.5	23
1030-1090	2.2	24	+ 5	0.3	+16	2.0	1.5	23
1100-1400	2.2	30	+10	1.0	+21	2.0	2.0	30
1060-1550	2.6	38	+10	1.0	+21	2.0	2.0	40
1430-1540	2.5	24	+ 5	0.3	+16	2.0	1.5	23
1500-2000	3.0	50	+15	1.0	+26	2.0	2.0	65
1750-1850	2.8	33	+10	0.3	+21	2.0	2.0	35
1400-2400	3.5	28	+10	1.0	+21	2.0	2.0	35
1400-2400	5.0	28	+13	1.0	+24	2.0	2.0	45
1700-2400	3.5	28	+10	0.8	+21	2.5	1.8	35
2100-2400	3.3	28	+ 9	0.5	+20	2.5	1.5	35
2200-2300	3.1	28	+ 9	0.3	+20	2.5	1.3	35
2200-2300	3.3	28	+ 9	0.3	+20	1.3	1.3	35
2100-2400	4.3	28	+ 9	0.5	+20	1.5	1.5	35
2400-2700	3.5	29	+10	0.8	+21	2.0	2.0	40
2500-2580	1.8	30	+ 9	0.3	+20	1.3	1.4	80
2500-2580	2.2	30	+ 9	0.3	+20	1.3	1.4	80
2700-2900	3.5	24	+11	0.5	+22	2.0	2.0	40
2700-2900	5.5	24	+12	0.5	+23	2.0	2.0	45
2700-3100	3.7	24	+10	0.5	+21	2.0	1.7	40
3100-3500	4.3	30	+10	0.5	+21	2.0	2.0	50
3100-3500	6.0	30	+10	0.5	+21	2.0	2.0	50

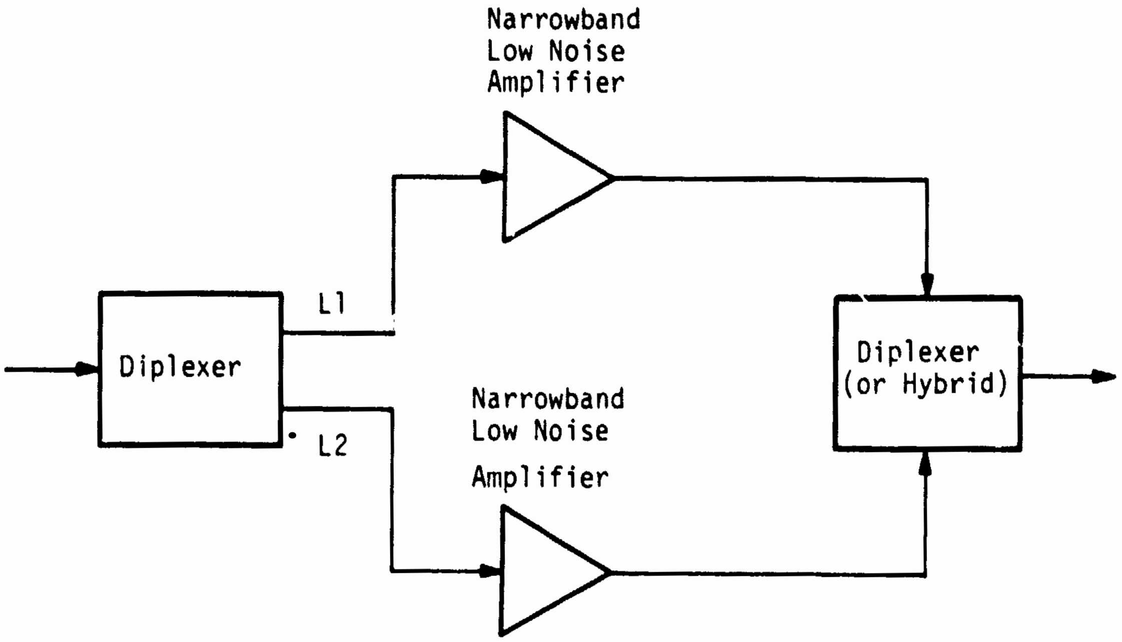

Figure 9. Preamplifier Configuration Used for Phase I GPS Receivers

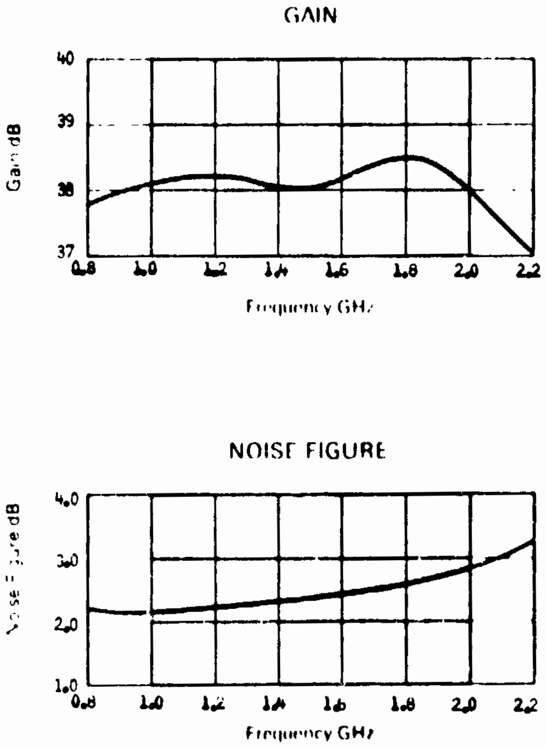

Figure 10. Typical Low Noise Amplifier Gain and Noise Figure Variation with Frequency

the low noise amplifier performance due to the additional elements. The effect of these elements is now discussed.

The purpose of the EMI filter is to prevent strong unwanted signals that are outside the GPS frequency bands from saturating the preamplifier. The simplest form of filter is the bandpass filter that passes both L1 and L2 frequencies, as shown in Figure 11a. The disadvantage of this filter is that interfering signals that fall in the 300 MHz spectral region between L1 and L2 can potentially saturate the preamplifier. To eliminate this problem, the filter would need to be a double tuned filter, peaked at the L1 and L2 frequency of 1575 MHz and 1227 MHz, respectively, as shown in Figure 11b. The insertion loss for this filter will be somewhat greater than that for the bandpass filter case.

Since the filter precedes the low noise amplifier, as does the switch, insertion loss from these sources directly degrades the preamplifier overall noise figure. Thus, a tradeoff exists between filter selectivity, which is obtained by adding more sections and thus increasing the insertion loss, and overall preamplifier noise figure. The selectivity of the bandpass filter as a function of the number of sections is illustrated in Figure 12, and the insertion loss of the filter as a function of the number of sections is given by

$$\text{IL} = \text{Insertion Loss} = \frac{(\text{Loss Constant})(\text{Number of Sections} + 1/2)}{\text{Percent 3 dB BW}} + 0.2 .$$

Thus, for a three-section filter, a reasonable compromise that has a 3 dB bandwidth of 400 MHz (centered on $\frac{1575 - 1227}{2} + 1227 = 1400$ MHz), the insertion loss is found to be given by

$$\begin{aligned}\text{IL} &= \frac{(1.2)(3 + 0.5)}{(400/1400)100} + 0.2 \\ &= 0.35 \text{ dB} .\end{aligned}$$

From Figure 12, it is seen that the filter response is down 20 dB at frequencies of 680 MHz and 2120 MHz. Since this roll-off is probably slower than the amplifier roll-off, a four-section filter is chosen. This gives an insertion loss of 0.39 dB, and a response 20 dB down at approximately 880 MHz and 1920 MHz.

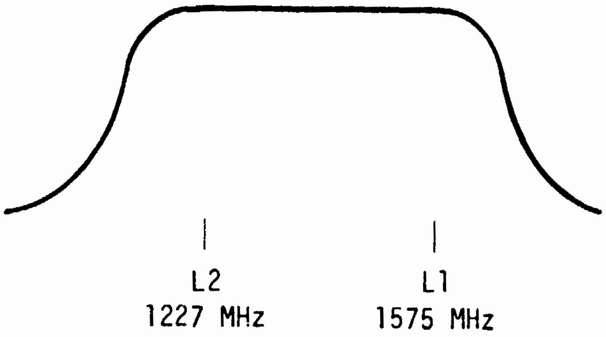

a. Bandpass Filter Shape with No EMI Between L1 and L2

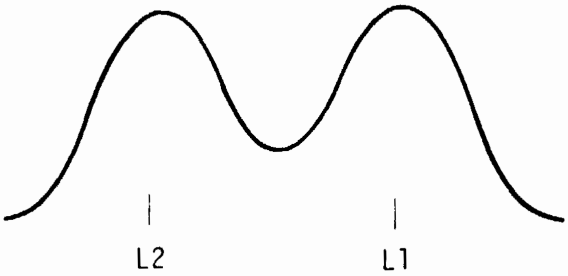

b. Bandpass Filter Shape with EMI Threat Between L1 and L2

Figure 11. GPS Preamplifier Bandpass Filter Shapes

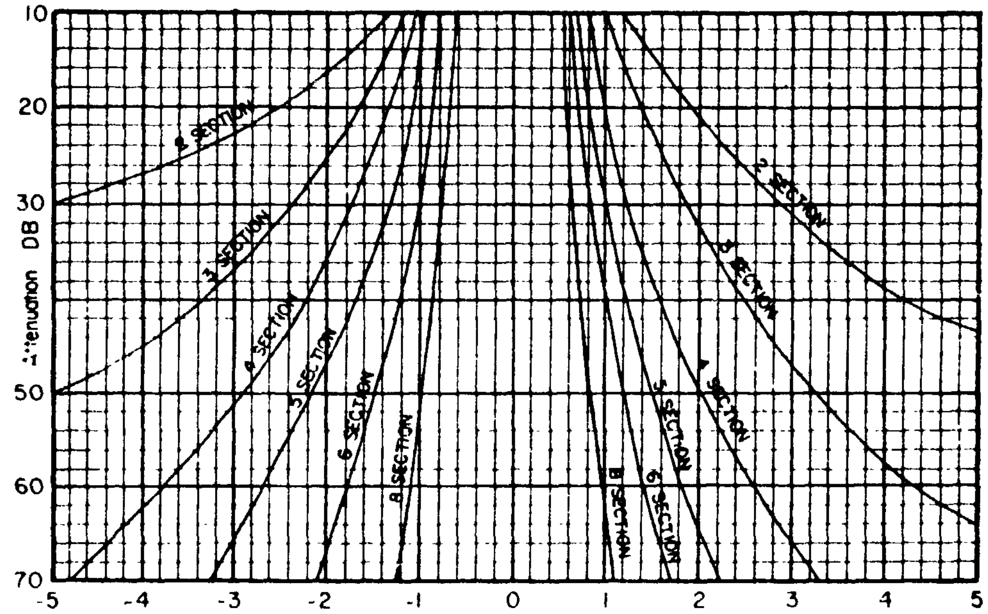

Figure 12. Bandpass Filter Attenuation Characteristics

The RF switch shown in Figure 7 is implemented as a magnetic latching switch. This means that the switch is normally deenergized and in one of the two stable positions. To switch, a short pulse is applied to the appropriate switching coil. This pulse is typically approximately 15 milliseconds in duration and about 2 watts. The outline drawing for a typical low-loss coaxial switch is shown in Figure 13. The significant performance parameter for the switch is the insertion loss of 0.2 dB.

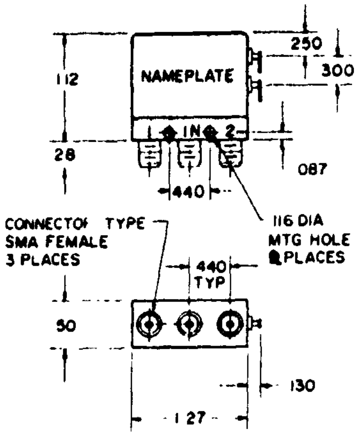

Figure 13. Outline Drawing for Typical Low Loss Coaxial Microwave Switch

The signal summer shown following the broadband amplifiers in Figure 7 is a 3 dB hybrid power summer. Use of a summer for this element means that the unused amplifier must be turned off (DC power turned off) to avoid a 3 dB degradation in preamplifier noise figure. To avoid turning off the unused amplifier, another switch can be substituted for the 3 dB hybrid.

The overall noise temperature of the preamplifier, considering the elements discussed above, is given by

$$T_{PA} = (L_1 - 1)T_0 + \frac{(NF - 1)T_0}{1/L_1} + \frac{(L_2 - 1)T_0}{1/L_1 G} ,$$

where L_1 = combined loss of input selection switch and input filter
NF = noise figure of low noise amplifier
G = gain of low noise amplifier
L_2 = loss of output switch or 3 dB hybrid .

The effective noise figure of the preamplifier is given by

$$NF_{PA} = \frac{T_e}{T_0} + 1$$

$$= NF\,L_1 + \frac{(L_2 - 1)L_1}{G} .$$

From the survey of available commercial components, the following parameter values are appropriate:

$NF = 2.4$ dB
$G = 38$ dB
$L_1 = 0.2 + 0.4$ dB $= 0.6$ dB
$L_2 = 0.2$ dB (switch) $= 3.2$ dB (hybrid) .

Thus, the overall noise figure for the preamplifier is found to be 3 dB. It should be noted that the choice of either the switch or the hybrid for the output selection affects the overall noise figure so insignificantly that it is not a factor in the preamplifier design configuration decision nor in the overall system performance.

Since the preamplifier noise figure is so critical to system performance, techniques for testing this parameter are discussed here.

Using a test set-up such as shown in Figure 14, the receiver is adjusted to the desired NF measurement frequency. The noise figure meter input selector is set to the receiver IF output frequency.

The variable attenuator is used to optimize the input level to the NF meter.

Precautions should be taken when using a gas tube noise source to assure that large voltage "spikes" will not be applied to the amplifier input, with resultant damage or erroneous results. Also, where necessary, the noise figure reading obtained should be corrected for noise source variances (from nominal specified excess noise ratio) and for second stage (receiver or post amplifier) contributions. When such precautions and corrections are adhered to, good correlation is obtained between various commercial noise figure measuring equipments.

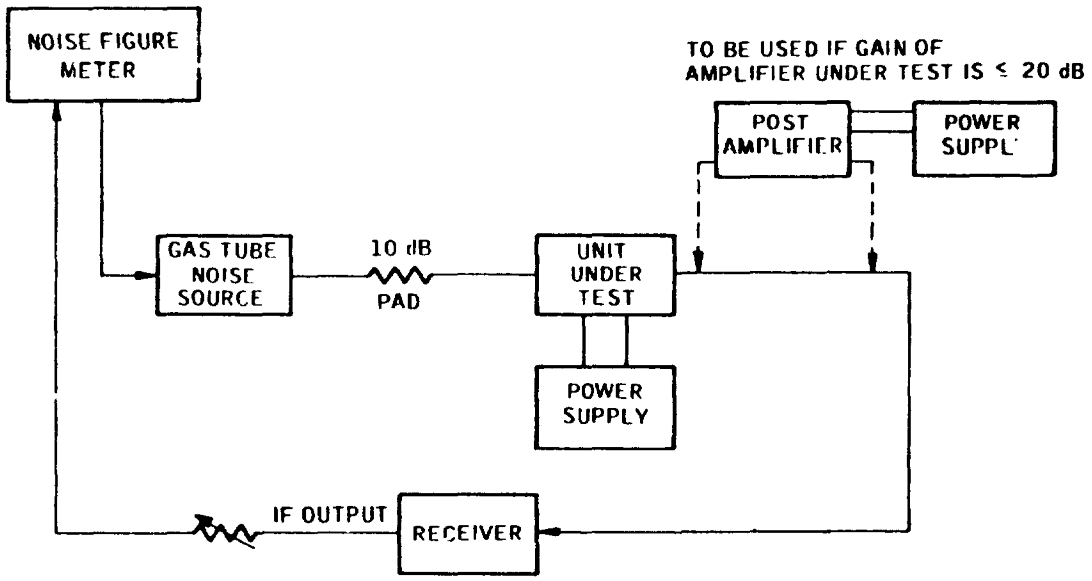

Figure 14. Preamplifier Noise Figure Test Set-Up

Since the method of selecting between redundant preamplifiers is an electromechanical switch, as shown in Figure 7, it is of interest to consider alternate methods of selecting the preamplifier. One such alternate, which at first appears attractive, is a 3 dB hybrid power splitter. The analysis which follows shows that this can lead to a 3 dB signal-to-noise degradation and is thus not a satisfactory choice. Furthermore, an analysis is presented which shows that a switch rather than a hybrid should be used at the receiver to select between the upper and lower antennas.

The simplest way to provide dual redundancy for the preamplifiers is to parallel them by using 3 dB hybrid power splitters/summers, as shown in Figure 15. The equivalent noise model is shown in Figure 16. The amplitude of the output (input to ideal summer) of the upper arm is given by

$$\frac{g\,s(t)}{\sqrt{2}\,\sqrt{2}} + \frac{g\,n_1(t)}{\sqrt{2}}$$

and the output of the lower arm is

$$\frac{g\,s(t)}{\sqrt{2}\,\sqrt{2}} + \frac{g\,n_2(t)}{\sqrt{2}} ,$$

so that the output of the summer is given by

$$v_0(t) = g\left[s(t) + \frac{n_1(t)+n_2(t)}{2}\right].$$

The signal power is $g^2 s(t)^2 = g^2 P$, and the noise power is given by

$$\begin{aligned} N &= \frac{g^2\,\overline{\left[n_1(t)+n_2(t)\right]}^{\,2}}{2} \\ &= g^2\left[\frac{\overline{n_1(t)^2}}{2} + \frac{\overline{n_2(t)^2}}{2}\right] \\ &= g^2\left[\frac{\sigma_1^2}{2} + \frac{\sigma_2^2}{2}\right] \\ &= g^2\sigma^2 , \end{aligned}$$

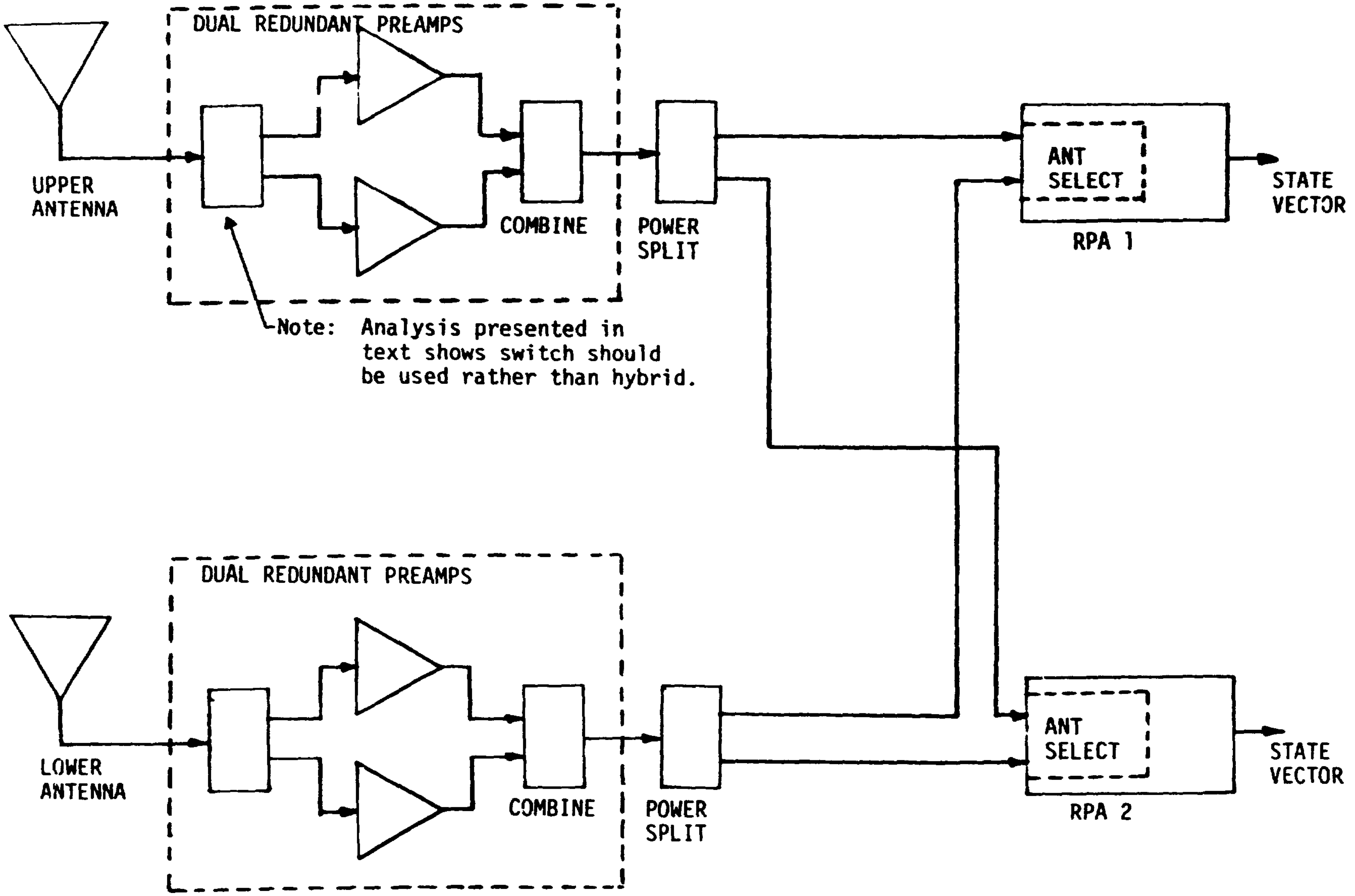

Note: Analysis presented in text shows switch should be used rather than hybrid.

Figure 15. Shuttle/GPS RF System Block Diagram

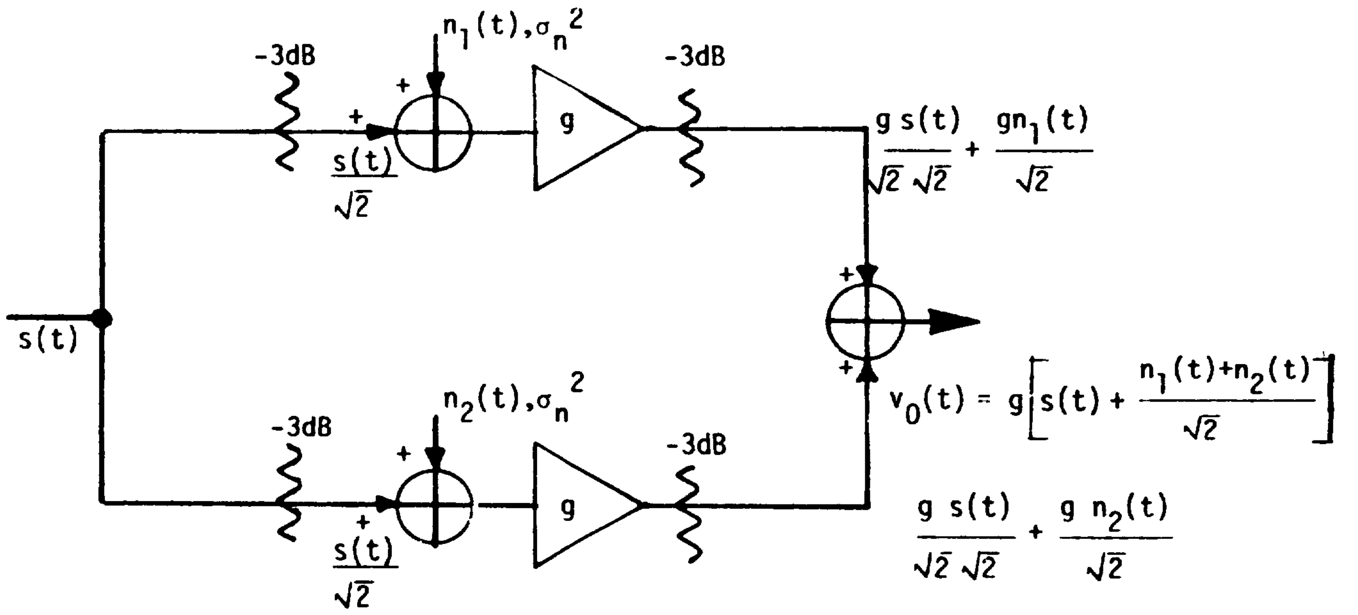

Figure 16. Noise Model of Two Preamplifiers in Parallel by Means of Input and Output 3 dB Hybrids

so that the output signal-to-noise ratio is $S/N = P/\sigma^2$, which is the same signal-to-noise ratio found at the output of the single preamplifier without the power splitter. Thus, there is no loss in SNR in parallelling two preamplifiers with hybrid power splitters/summers. However, this is not the case if one of the preamplifiers fails. In this case, the output of the upper arm is still

$$\frac{g\,s(t)}{\sqrt{2}\,\sqrt{2}} + \frac{g\,n_1(t)}{\sqrt{2}},$$

but the output of the lower arm is zero, by setting the gain $g = 0$. Thus, the output of the summer is

$$v_0(t) = \frac{g\,s(t)}{\sqrt{2}\,\sqrt{2}} + \frac{g\,n_1(t)}{\sqrt{2}},$$

and the signal power is

$$\frac{g^2\,\overline{s(t)^2}}{4} = \frac{g^2 P}{4}$$

and the noise power is given by

$$N = \frac{g^2\,\overline{n_1(t)^2}}{2} = g^2\frac{\sigma^2}{2},$$

so that the output signal-to-noise ratio is $S/N = P/2\sigma^2$. Thus, if one of the parallel preamplifiers fails, there is a 3 dB loss in SNR due to the 3 dB signal loss in the input power splitter. This loss is avoided by replacing that splitter with a SPDT switch.

The signal-to-noise ratio that results from feeding one receiver from two antenna/preamplifiers via a hybrid summer can be found by rearranging the model in Figure 16 into the model shown in Figure 17. There is no signal in the lower arm since only one antenna at a time picks up the desired GPS signal. The output of the upper arm is

$$\frac{g\,s(t)}{\sqrt{2}} + \frac{g\,n_1(t)}{\sqrt{2}}$$

and the output of the lower arm is

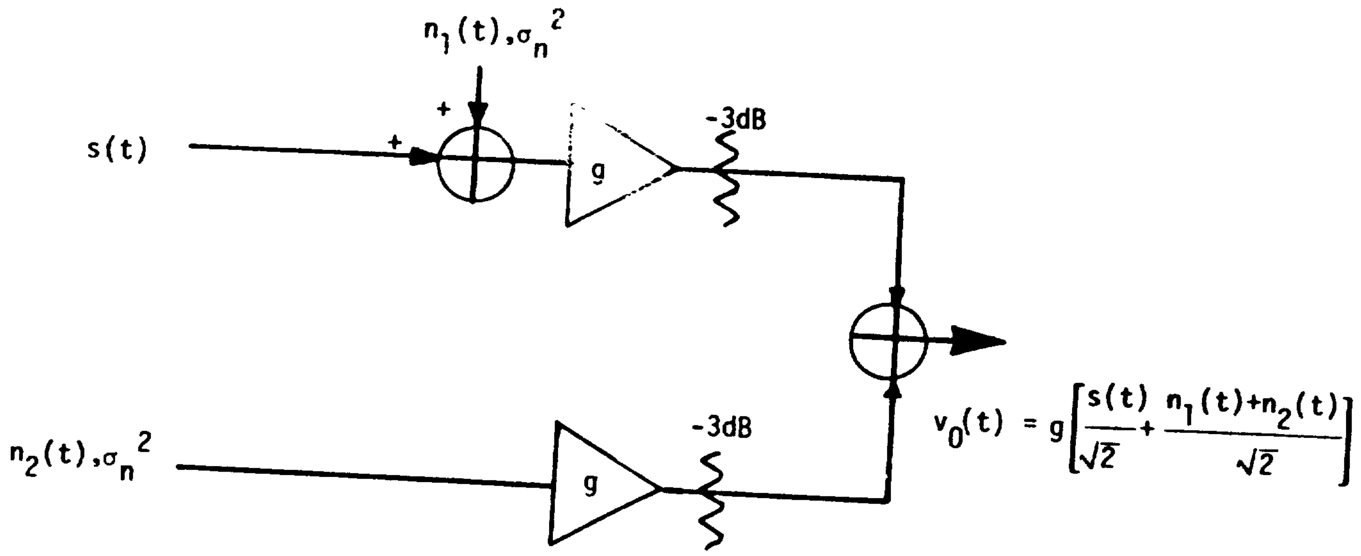

Figure 17. Noise Mode for Summing Upper and Lower Signal Paths at RPA Input

$$\frac{g\,n_2(t)}{\sqrt{2}},$$

so that the summer output is

$$\frac{g\,s(t)}{\sqrt{2}} + g\left[\frac{n_1(t)}{\sqrt{2}} + \frac{n_2(t)}{\sqrt{2}}\right].$$

The output signal-to-noise ratio is

$$\begin{aligned} SNR &= \frac{g^2\left[\frac{s(t)}{\sqrt{2}}\right]^2}{g^2\left[\frac{n_1(t)}{\sqrt{2}} + \frac{n_2(t)}{\sqrt{2}}\right]^2} \\ &= \frac{P}{2\sigma^2}. \end{aligned}$$

Thus, there is a 3 dB loss in signal-to-noise ratio if a hybrid summer is used to sum the upper and lower antenna inputs at the RPA. For this reason, a switch must be used for the antenna management function.

4.0 SHUTTLE GPS RECEIVER ARCHITECTURE

There are two basic GPS receiver architectures that have been considered for the Shuttle GPS receiver. They are the parallel channel receiver and the sequential receiver. Examples of the parallel channel receiver are the X set and the Collin's GDM set. A functional block diagram of the X set is shown in Figure 18. Examples of sequential receivers are the manpack receiver and the GPSPAC receiver. A functional block diagram of the GPSPAC is shown in Figure 19.

The major generic difference between the parallel channel receiver and the sequential receiver is a simple one. The sequential receiver time multiplexes one channel among four or more satellite signals in a serial manner. In the parallel channel receiver, four or more parallel hardware channels simultaneously process the satellite signals. Somewhat better performance and platform dynamics capability are the advantages gained by the parallel channel set. However, this is at the expense of almost four times the hardware complexity of the sequential receiver. This translates into greater volume, weight, power consumption and cost for the parallel channel set. Of great significance in the decision process for choosing the baseline Shuttle GPS receiver is that no existing parallel receiver would fit within the volume constraints of the avionics equipment bay.

On the other hand, the size of the existing sequential receivers was found to be compatible with the Shuttle volume constraints. Furthermore, analysis has shown that the navigation performance of the sequential receiver meets the requirements of a Shuttle GPS navigation system. Analysis has also shown that the sequential receiver will track the Shuttle signal dynamics. Consequently, a sequential receiver architecture has been chosen for the baseline Shuttle GPS receiver. A second channel for the sequential receiver is recommended to provide faster acquisition (time to first fix) and a measure of redundancy.

It should be noted that this choice should not rule out consideration of future parallel channel receivers that take advantage of technology to meet the strict volume constraints of the Shuttle.

The remainder of this section presents a discussion of some of the more detailed trade-offs that can be made within the sequential receiver architecture; first, however, a generalized review of the sequential

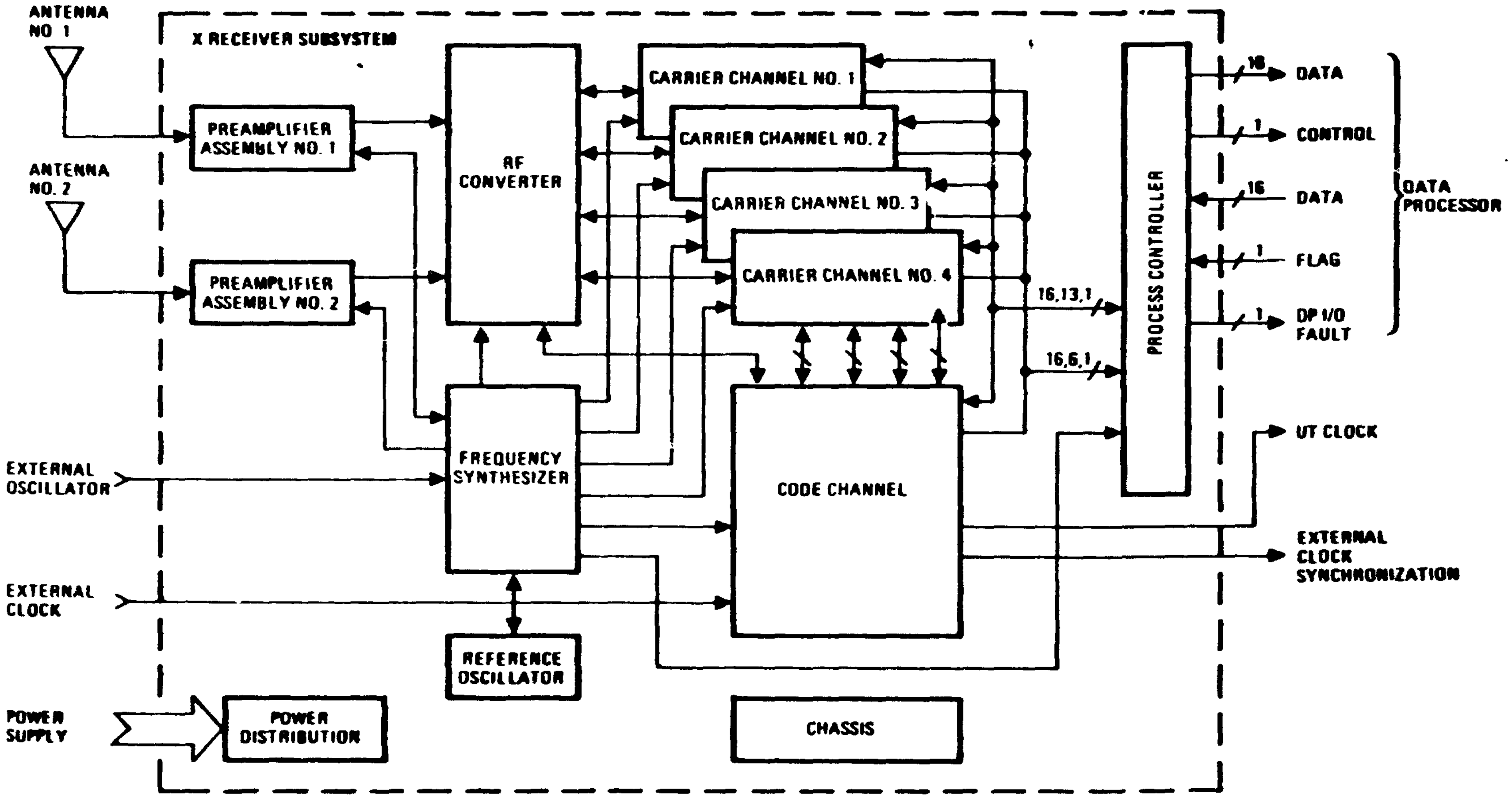

Figure 18. Functional Block Diagram of X Set Parallel Channel GPS Receiver

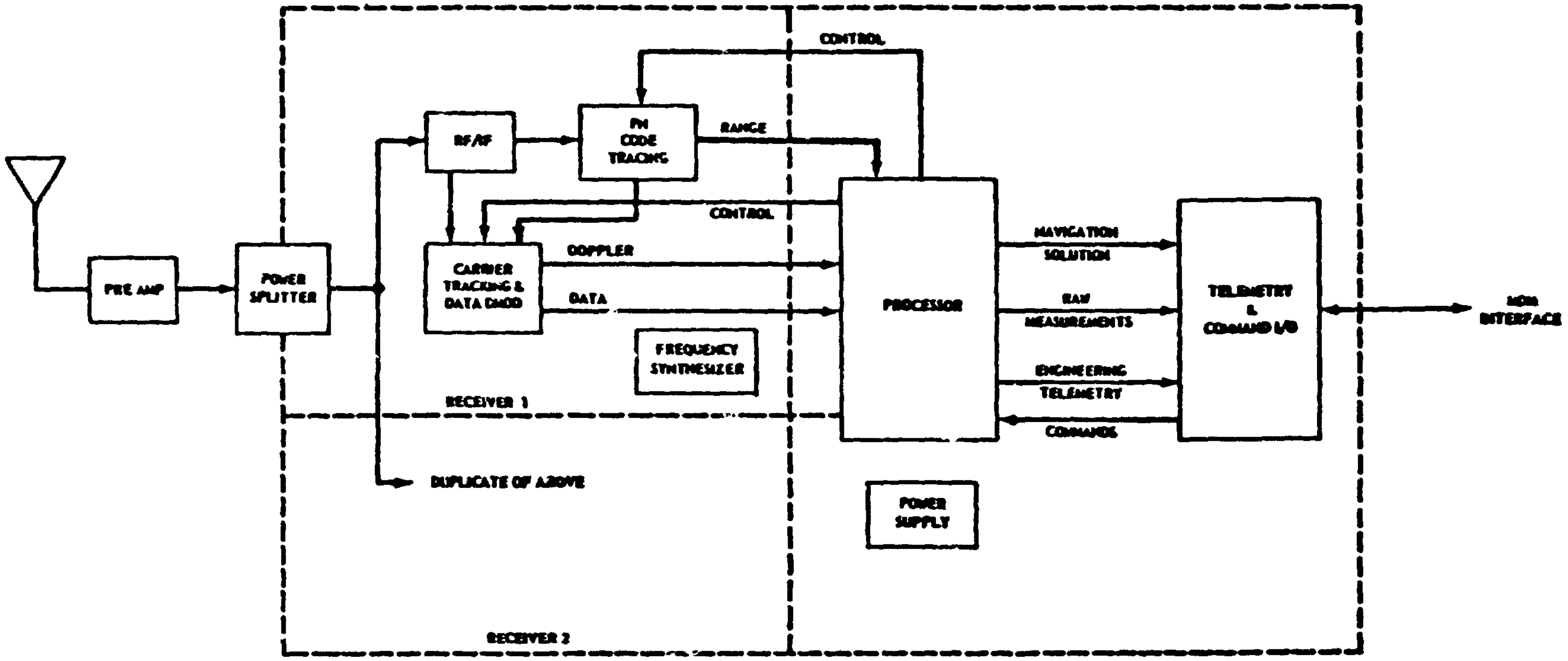

Figure 19. GPSPAC Receiver Functional Block Diagram

receiver concept is presented.

A simplified functional block diagram of a single-channel sequential receiver is shown in Figure 20. The salient feature of this type of receiver is a single RF/IF chain that is time-multiplexed among satellite measurements. Time-multiplexing is also utilized for tracking loops, and the other baseband functions such as data detection, acquisition and synchronization detection, etc. A typical sequence of operations for this type of receiver is shown in Figure 21. The basic time element of this approach is the frame which is divided into satellite slots. Each satellite slot is divided into an L1 and an L2 slot and these slots are divided into the receiver process intervals. Typically, two seconds are sufficient for an L1 or L2 slot so that, for processing four satellite signals, a 16-second frame is required. If two parallel receiver channels are used so that an L1 and L2 can be processed simultaneously, the frame time can be halved, i.e., an 8-second frame. However, it has been shown that a shorter frame time does not provide any beneficial navigation performance for the Shuttle GPS system. A parallel L2 channel would increase receiver complexity and cost and is thus a poor trade-off. It should be noted, however, that parallel channels in the sequential receiver may be desirable from the redundancy and initial acquisition time (time to first fix) viewpoint.

The first receiver-processing interval is used to search and acquire the P code. This involves prepositioning, or slewing, the coder to the predicted code phase for the particular satellite to be acquired. This phase information is calculated and stored by the receiver processor (microcomputer) for each satellite on a frame-to-frame basis. Once the coder is slewed to the proper phase, it goes into a limited automatic search mode wherein it searches out the few code chips of uncertainty (see Section 6.0 for code acquisition discussion). At this same time, the receiver AFC is enabled. As the correct code phase is reached, the code search stops and the signal-to-noise ratio increases due to correlation so that the AFC loop starts to pull the receiver VCO to the correct frequency.

In the second receiver-processing slot, the code loop is enabled and starts to pull into phase lock, thereby decreasing the correlation error to a small fraction of a chip. The AFC pulls in the frequency more rapidly due to the increase in S/N.

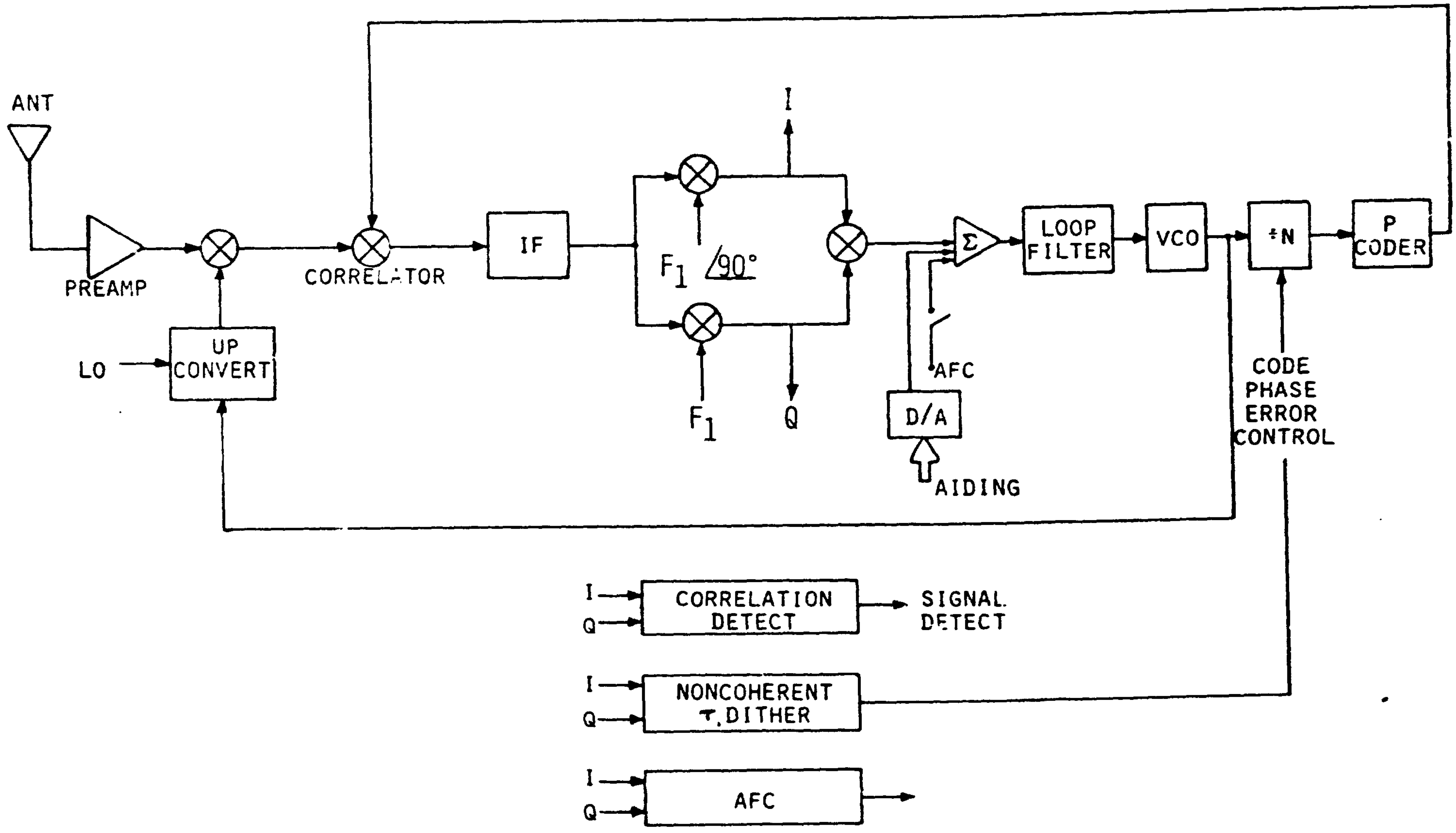

Figure 20. Sequential Receiver Functional Block Diagram

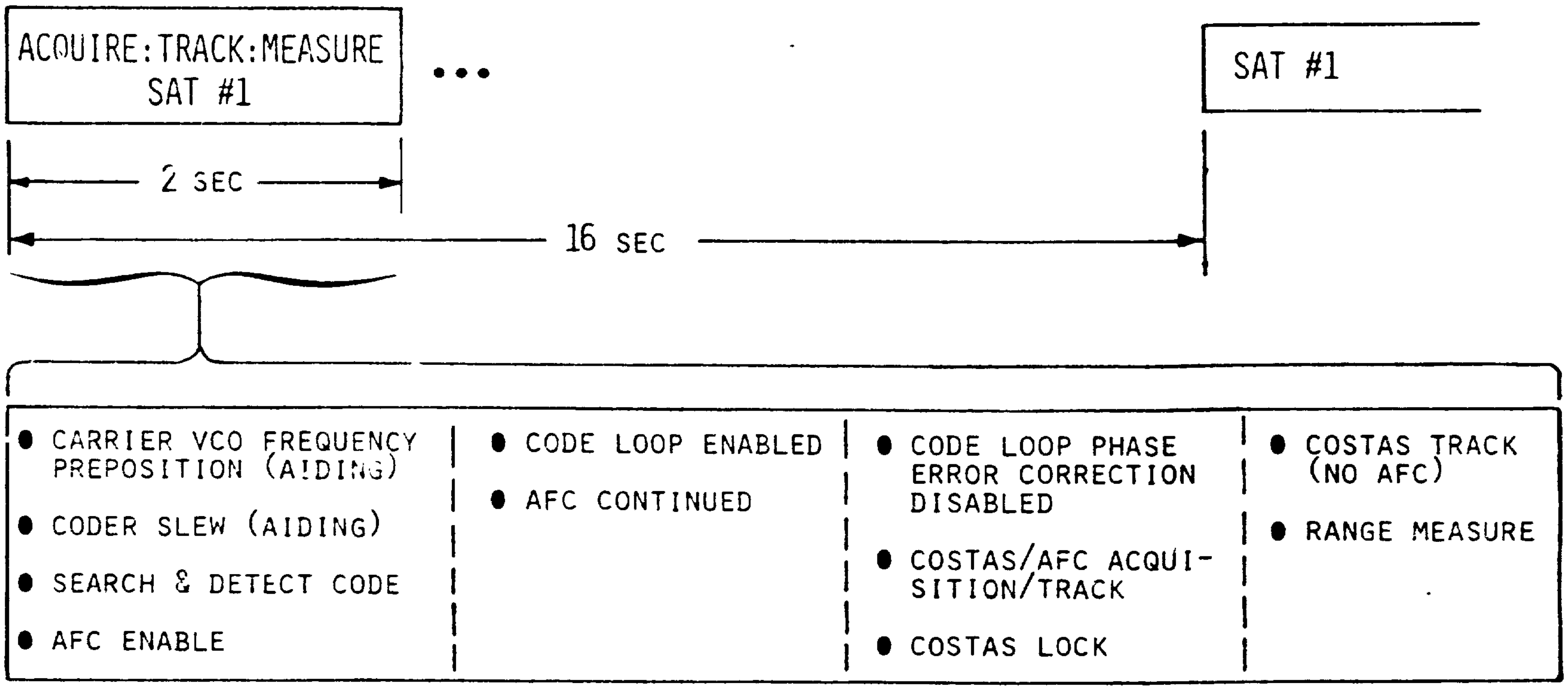

Figure 21. Sequential Receiver Timing

During the third receiver-processing slot, the Costas loop is enabled and starts to pull in. In addition, the code loop is disabled since, by this time, the loop has pulled the code phase error into an acceptable error. Since the PN code is coherent with the carrier, the Costas loop VCO can be scaled by the frequency ratio (1575.42/10.23) and used as a clock source to drive the coder.

Finally, in the fourth slot, with the Costas loop tracking in steady state, the pseudo range and delta range (range rate from carrier times interval) measurements are made.

The sequential receiver process is highly dependent on microprocessor control. Figure 22 illustrates the interfaces between the receiver microprocessor and the other receiver functions. In this particular architectural scheme, the carrier-tracking function is implicit in the synthesizer wherein the phase and frequency of an appropriate local oscillator (LO) is adjusted by the rate multiplier/incremental phase modulator (RM/IPM). The RM/IPM is, in turn, controlled by the Costas loop error signal developed in the microprocessor. All the tracking error signals are developed in the microprocessor by appropriate processing of the I and Q signals. The I and Q signals are at baseband and the A-to-D converter that converts these signals to digital words is the major interface between the analog and digital portion of the receiver. It should be pointed out that it may not be practical to implement the RM/IPM function digitally for the Shuttle GPS receiver due to the high doppler offsets. An analog VCO might be needed. Whether a digital VCO or analog VCO is used, the loop filtering and error control are via the microprocessor.

The RF/IF frequency scheme has particularly strong impact on overall receiver architecture due to the impact on synthesizer complexity. The general issue is whether single conversion, double conversion or even triple conversion from RF to IF to baseband should be used. From an overall receiver complexity consideration, single conversion provides the least complex receiver. On the other hand, this type of receiver presents the greatest design risk due to the large gain required at a single frequency. In the discussions of frequency conversion trade-offs that follow, translation to baseband (I and Q channels) via coherent LO is not treated as a frequency conversion in the traditional sense but, rather,

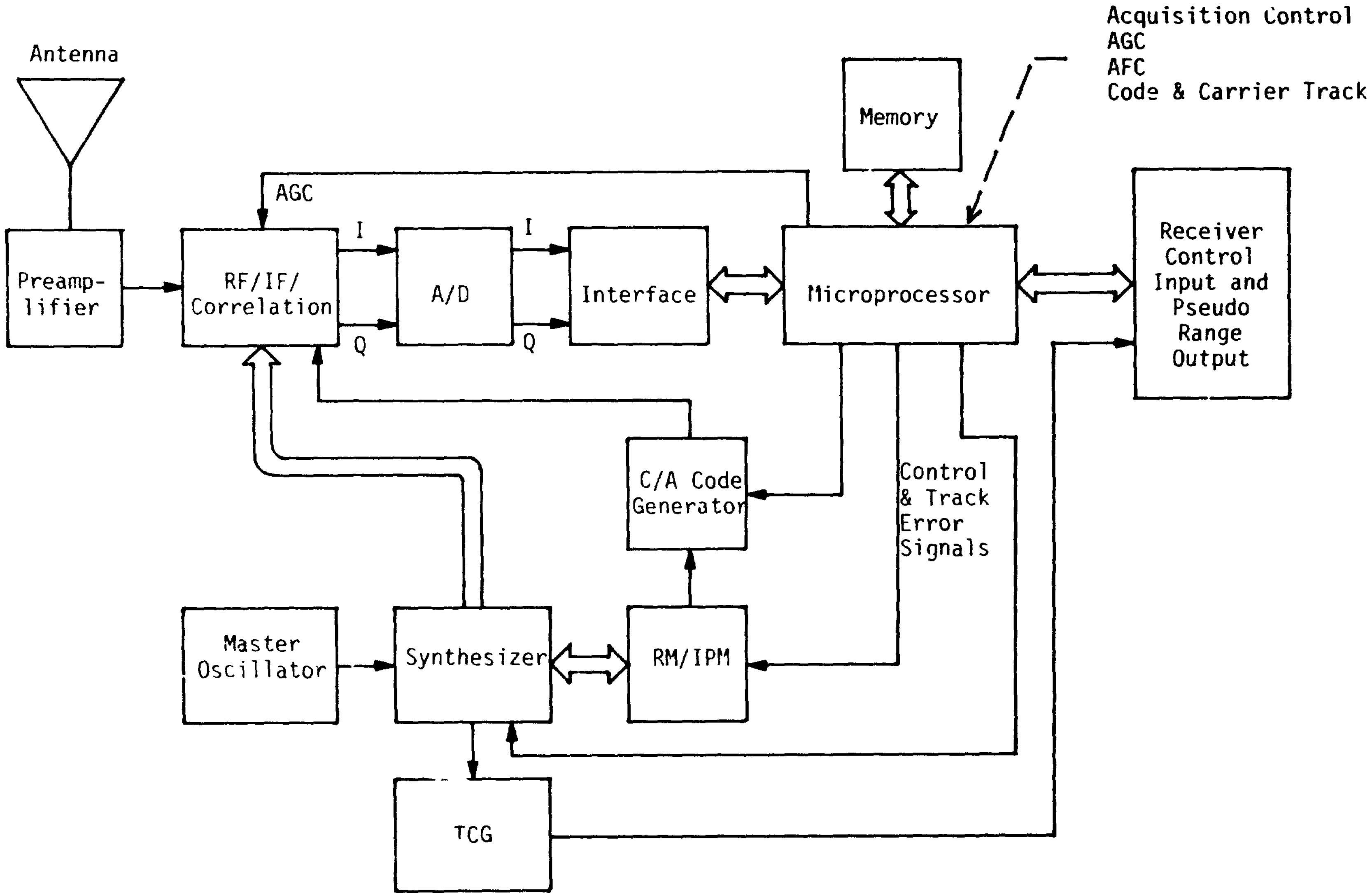

Figure 22. Digital GPS Receiver Interfaces

as part of the traditional demodulation process.

The frequency conversion plan for a single-conversion GPS receiver that is designed to minimize volume and cost is shown in Figure 23. Both the first LO and the coherent reference for translation to I and Q are derived from the same VCO which is part of the carrier tracking loop. This receiver architecture is simple and straightforward and has a similarly simple frequency synthesizer; however, this receiver requires approximately 120 dB to 140 dB gain at the single IF frequency of 71.61 MHz. This much gain at a single IF frequency is counter to traditional receiver design practices. Careful evaluation of the detailed receiver design is required to assess the design risk.

At the opposite extreme of receiver design is the triple-conversion approach to GPS receiver design, as shown in Figure 24. This frequency plan distributes the gain at three IF frequencies; it uses three local oscillators in addition to the coherent translation to I and Q baseband channels. This receiver architecture has been used in the manpack and GPSPAC receivers with good performance results. As might be expected, however, it results in a complex frequency synthesizer.

A potential compromise between the single- and triple-conversion GPS receiver architectures is the double-conversion receiver, as shown in Figure 25. The receiver design is of moderate complexity and offers the advantage of distributing receiver gain at two IF frequencies. A possible frequency synthesizer plan for this receiver is shown in Figure 26. The plans in Figures 25 and 26 are presented as possibilities. Detailed studies of potential spurs and image frequency problems are necessary before an actual design of the double-conversion receiver can be recommended.

As a result of the investigation of the basic trade-offs among single-, double-, and triple-conversion receiver architectures, it appears that double-conversion represents a good choice. This, of course, must be weighed against any existing receiver designs which have proved successful and which are presented for Shuttle application on a competitive performance, volume, and cost basis.

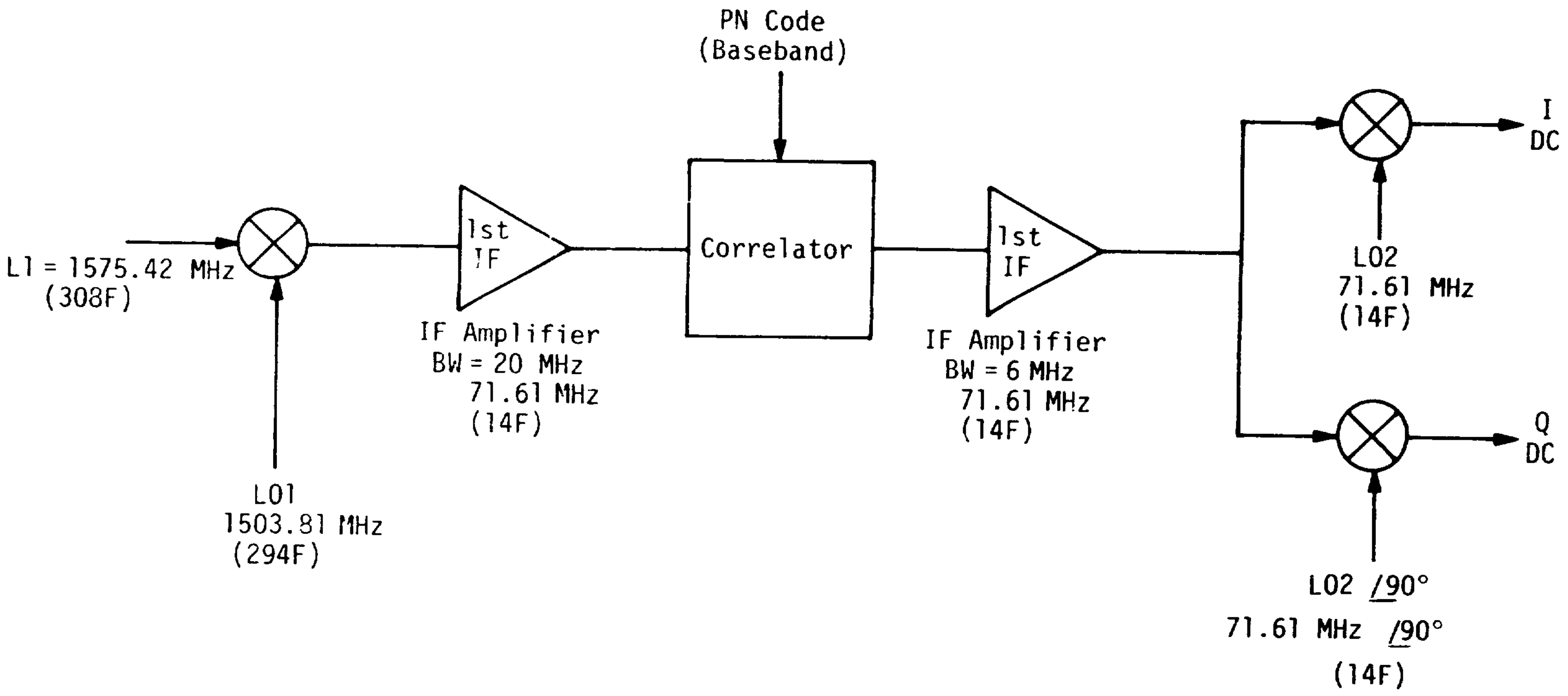

Figure 23. Single Conversion GPS Receiver Frequency Conversion Plan

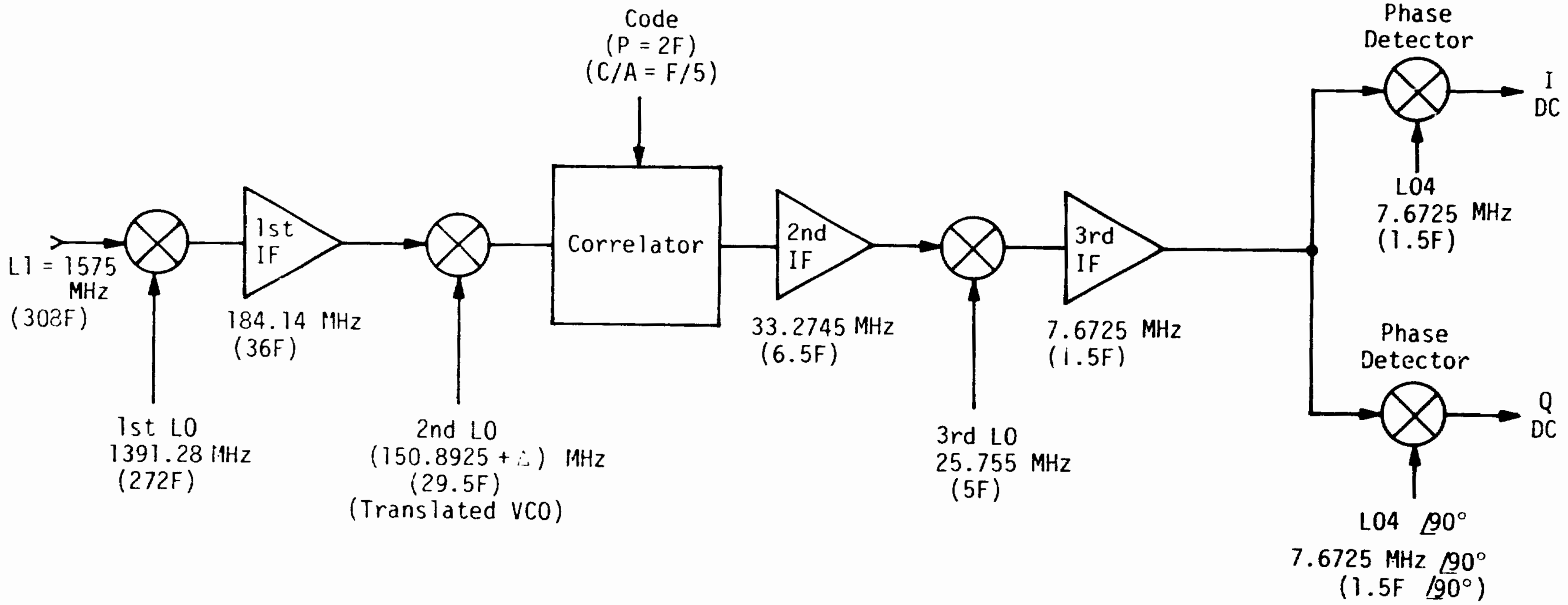

Figure 24. Triple Conversion GPS Receiver Frequency Conversion Plan

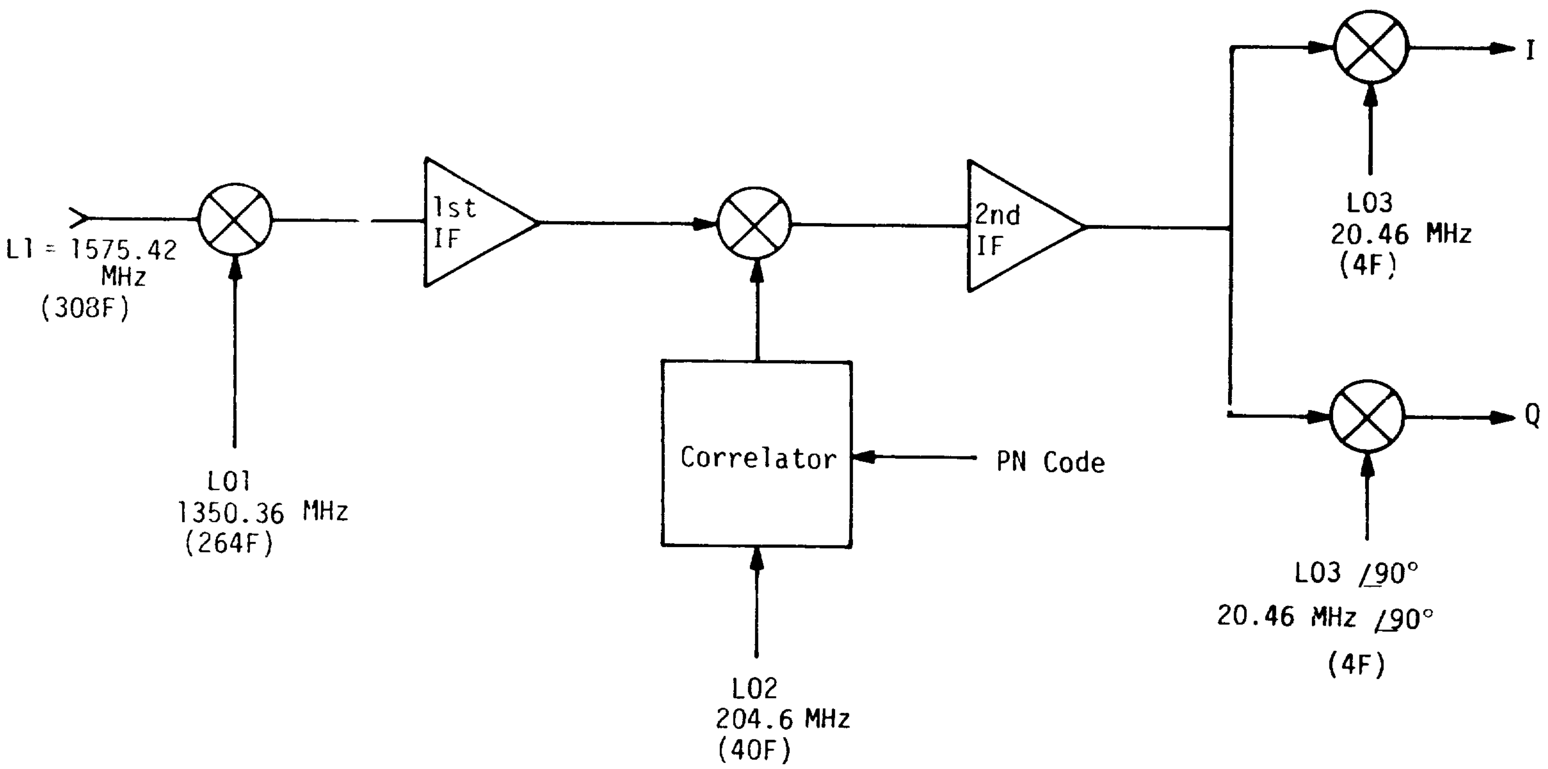

Figure 25. Double Conversion GPS Receiver Frequency Conversion Plan

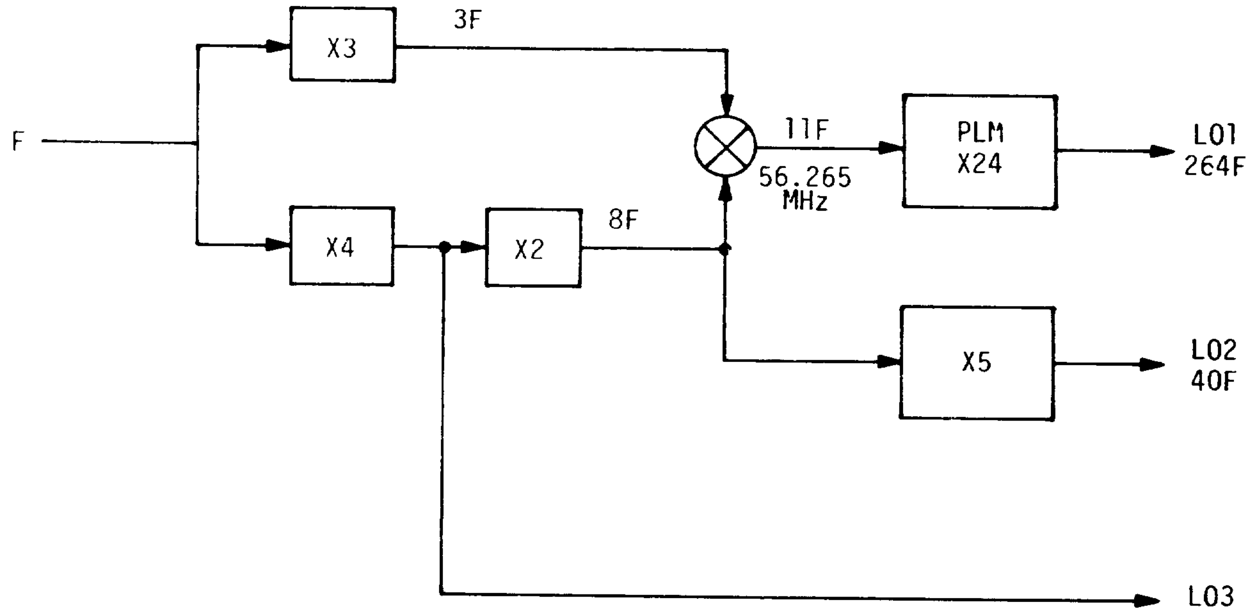

Figure 26. Possible Frequency Synthesizer Plan for Double Conversion GPS Receiver

5.0 SHUTTLE GPS EMI/RFI ISSUES

This section discusses the analyses of Shuttle emitter RF harmonics and intermods interfering with GPS. It also examines the antenna isolation required between the TACAN antenna and GPS antenna to minimize degradation to the GPS navigation system. The conclusions of both analyses are that there is no interference problem.

5.1 Evaluation of Intermodulation Interference

Because the Shuttle has several RF emitters on board capable of radiating simultaneously, there is a possibility of intermods falling within the GPS frequency bands. Furthermore, there is also the possibility of harmonics of the lower frequency emitters either falling on GPS or mixing with other emitters and falling on GPS. Since this problem is not amenable to simple analytical techniques due to the large number of possible frequency combinations, a JSC computer program is used. This program, operated by Art Reubens, is shown in a functional diagram in Figure 27. As can be seen, the basic inputs are transmitter characteristics, receiver characteristics and antenna characterisics. The program calculates all harmonics up to the fifth harmonic and all intermods up to the fifth order. After calculating the antenna coupling factors involved, the program searches the intermods and harmonics for ones that fall within the specified bandwidth, in this case, 30 MHz centered about L1 and L2 GPS frequencies. Furthermore, it only prints those intermods that fall above a specified minimum power level in this case of -130 dBm. A sample output summary of the program is given in Table 17.

A majority of the interference found can occur only at the launch pad since the intermods are a result of mixing Shuttle emissions with KSC C-Band and/or weather radars. Axiomatix recommends that this form of interference not be taken into account in the Shuttle/GPS design trade-offs. This is because, should this interference actually exist, operational procedures can be used which will enable a launch pad GPS navigation fix to be obtained prior to launch. Furthermore, this interference is relatively insensitive to GPS antenna locations. For obvious reasons, those interferences which are "not operationally possible" have not been considered further. The only interferences of possible concern are those labeled as "significant products." Each of these products,

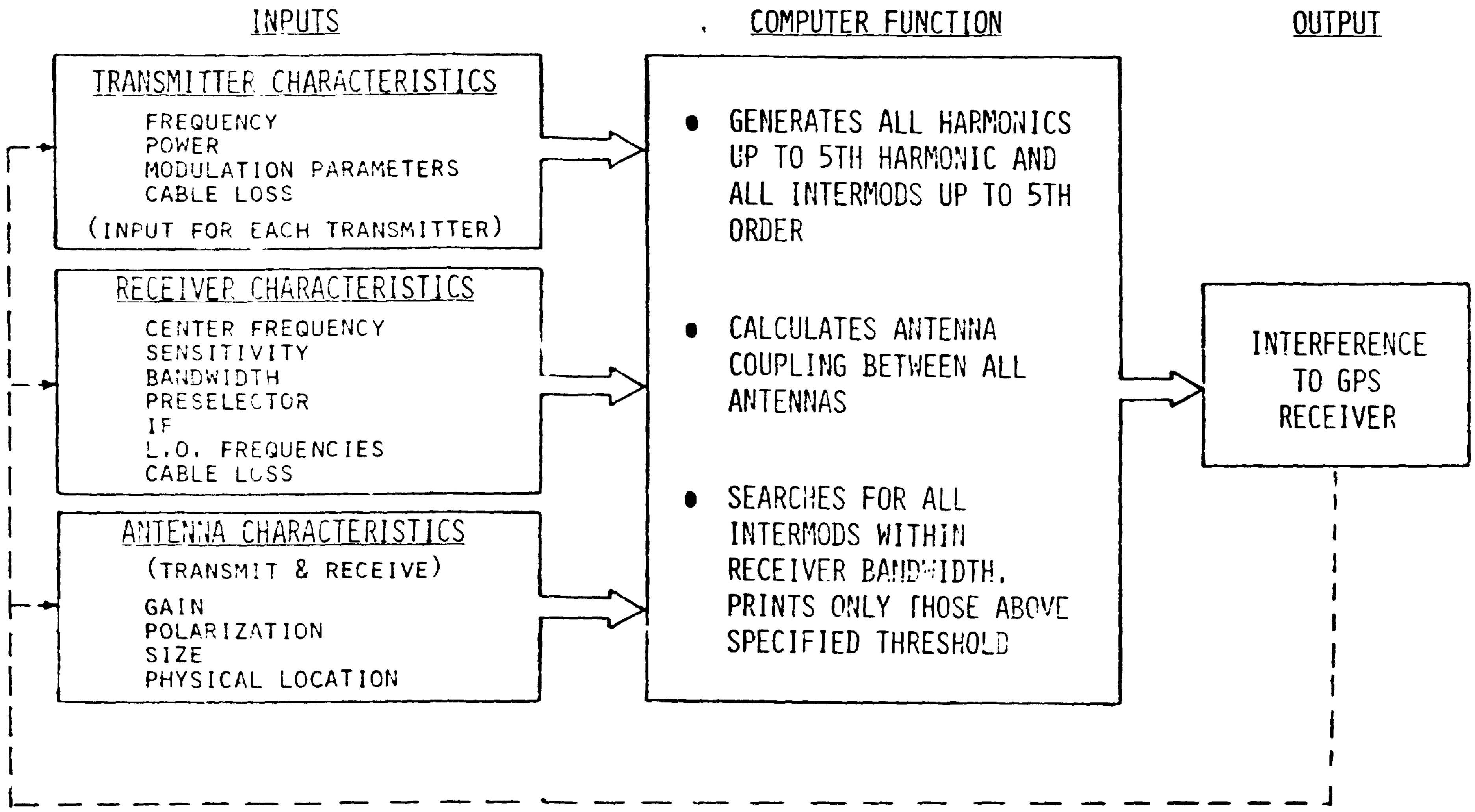

Figure 27. Computer Evaluation of Intermodulation Interference Functional Diagram

Table 17. Computer Evaluation of Intermodulation Interference, Sample Output

Source	Frequency	Harmonic	Beat Frequency	Power Level
TACAN Channel 35X Return to Landing Site at Kennedy	1,059 MHz	2nd		
UHF	296.8 MHz	3rd		
			1,227.6 MHz	-144.5 dBm

GPS L2 → 1,227.6 MHz

a total of 134, has been examined by Axiomatix. All but four of them are a result of mixing at least two Orbiter TACAN emissions with another Orbiter emission, with each TACAN operating on a separate, specific channel. Thus Axiomatix recommends against considering these interference sources in the Shuttle/GPS design trade-offs since it should be relatively easy to plan an operational "work-around" for obtaining a GPS navigation fix when two or more TACANs happen to be transmitting simultaneously. The four cases which can be considered potential operational sources of interference are summarized in Table 18. It should be noted that those four cases are all with the same basic set of emitters, the variables being antenna locations. Thus the frequency of the intermods summarized in Table 18 is constant, while the amplitude varies as a function of antenna geometry. The worst case is number 2, with the interfering intermod having a power level of -112 dBm. The effect of this intermod on the GPS signal processing is to raise the effective thermal noise level. Since the 10 megachip PN correlation process spreads the intermod power into an effective noise bandwidth of 10 MHz, the noise density of the "spread intermod" is then -112.9 - 10 log (10 MHz) = -182.9 dBm/Hz. The natural thermal noise density of nominally -171 dBm/Hz so that the interfering noise is 11.8 dB lower and effectively adds about 0.3 dB to the overall system noise. The L1 and L2 P code links can easily accommodate this degradation. Furthermore, since the intermod analysis is a worst-case analysis, the actual interference will probably not be as strong. Since the intermod spectrum is wider (approximately 5 MHz) than the 1 megachip C/A code signal, the power spectrum density for the C/A interference case is -112.9 - 10 log (5 MHz) = -179.9 dBm/Hz which results in approximately 0.6 dB degradation. The C/A link can support this degradation but, more importantly, since the radar altimeter is used below 2500 feet altitude, the GPS receiver will be operating with the P links in order to have navigation accuracies compatible with the low altitudes.

5.2 GPS/TACAN Antenna Isolation Requirements

5.2.1 Summary

The required isolation between the GPS antenna and the Shuttle TACAN antenna has been analyzed and found to be 28 dB. The analysis is

Table 18. Possible Intermodulation Products as Interference Sources

CASE	EMITTER COMBINATION	GPS ANTENNA LOCATION	INTERMOD LEVEL (dBm)
1	TACAN, RADAR ALTIMETER, UHF	CO-LOCATED WITH LOWER HEMI	-117.6
2	SAME AS 1, BUT DIFFERENT RADAR ALTIMETER/ANTENNA	SAME AS 1	-112.9
3	SAME AS 1	19" ABAFT LOWER HEMI	-119.5
4	SAME AS 2	SAME AS 3	-114.5

based on extrapolating the TACAN transmitter output spectrum measurements made by JSC.

5.2.2 Discussion

The requirements for GPS antenna isolation from the Orbiter TACAN antennas has been analyzed in light of the information contained in JSC report EEG-12/77-189, "TACAN Transmitter Pulse Characteristics." This antenna isolation is based on the desire to have the TACAN wideband modulation sideband energy falling in the GPS RF bandwidth to contribute less than 0.5 dB to the receiver overall noise figure. Since the TACAN PRF is relatively low (150 pps max) and the GPS precorrelator RF bandwidth is relatively wide (10 to 20 MHz) and separated from the TACAN center frequency by at least 77 MHz, the TACAN energy will appear as uncorrelated, wideband noise.

The natural noise spectral density for the Orbiter GPS receiver is approximately -171 dBm/Hz. Thus, if the spectral density of the TACAN interference in the GPS bandwidth is limited to -181 dBm/Hz, the degradation to the total signal-to-noise ratio will be less than 0.5 dB. Consequently, the difference between the actual TACAN interference spectral density and -181 dBm/Hz will be the required antenna isolation.

The effective noise bandwidth B_0 of the TACAN signal can be found from numerical integration of the measured spectrum, as shown in Figure 28. Thus,

$$B_0 = \frac{1}{S_0} \int_0^\infty S(f)\, df = \frac{1}{S_0} \sum_{i=1}^{N} S_i \, \Delta f = 0.7 \text{ MHz},$$

and the effective spectral density of the 1 kW (+60 dBm) TACAN pulse is 60 dBm - 10 log 0.7×10^6 = +1.5 dBm/Hz. Since the dynamic range of most spectrum analyzers is on the order of 60 dB and since it is necessary to determine power density levels approximately 180 dB below the TACAN density level, extrapolation techniques must be used to determine the TACAN spectral density at f_0 + 77 MHz (GPS L2 center frequency).

The first step is to compare the measured TACAN power spectrum with the TACAN specification. According to the specification, the power in a 0.5 MHz bandwidth centered ±0.8 MHz from f_0 (center frequency) and ±2 MHz from f_0 shall be 23 dB and 38 dB, respectively, below the power in a

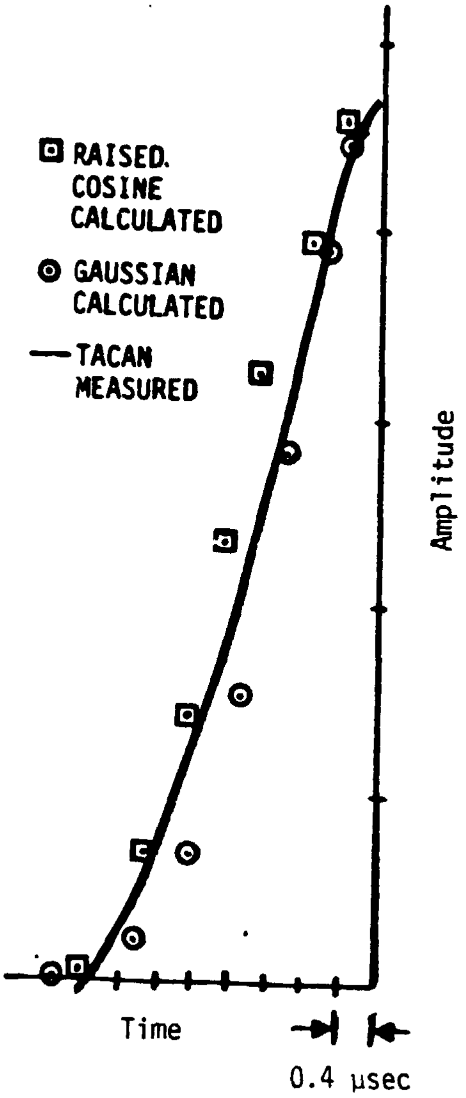

Figure 28. Measured TACAN Pulse Shape Compared With Calculated Pulse Shapes

0.5 MHz bandwidth centered at f_0. By using numerical integration of the measured TACAN power spectrum, the power at ±0.8 MHz is found to be 46 dB below that at f_0, and the power at ±2 MHz is at least 60 dB (analyzer limit) below that at f_0. Thus the actual performance of the TACAN, in terms of spectral shape, is at least 22 dB better than the specification. The problem now is to extrapolate this performance to f_0 + 77 MHz. This is accomplished by utilizing time domain information. Examination of the measured time response of the TACAN pulse, as shown in Figure 28, indicates that the actual pulse shape is between a Gaussian pulse and a raised cosine pulse. In terms of spectral response, the raised cosine pulse is the worst-case interference source. The spectrum of the raised cosine pulse is given by

$$F(\omega) = V\tau \frac{\sin \omega\tau}{\omega\tau \, [1 + (\omega\tau)^2]}$$

so that the power envelope falls off as the square of ω^3, or

$$\frac{P_1}{P_2} = 60 \log \left(\frac{\omega_1}{\omega_2}\right) .$$

Thus, since the power in 0.5 MHz at f_0 is found by numerical integration to be 58.7 dBm, the power density in 0.5 MHz at 77 MHz, by extrapolation, is found to be

$$\begin{aligned} P &= 58.7 \text{ dBm} - 60 - 60 \log \left(\frac{77}{2}\right) - 10 \log (0.5\text{x}10^6) \\ &= -153 \text{ dBm/Hz}. \end{aligned}$$

The required antenna isolation is thus

$$\text{Ant Iso} = 181 - 153 = 28 \text{ dB}.$$

Several points should be noted. First, this analysis does not treat spurs which the TACAN transmitter might generate, since Axiomatix has not received a diagram of the TACAN frequency generator to analyze the potential spur emission problem. Second, this analysis has concentrated on the L2 GPS frequency. Since L1 is 450 MHz away from the upper TACAN frequency, the wideband modulation sideband interference will not affect the L1 GPS performance from a signal-to-noise standpoint. However, the GPS preamplifier must be designed so that the high peak power TACAN pulses do not create serious intermodulations due to saturation of the preamplifier. Thus, if the 28 dB antenna isolation presents a serious implementation problem, Axiomatix recommends ignoring the requirement and not using the L2 frequency for ionospheric correction when the TACAN is operating in the upper portion of the band. Furthermore, ongoing studies may find that the ionospheric delay correction is unnecessary in the context of the Shuttle navigation accuracy requirements. If this is the case, the TACAN wideband interference to L2 is a moot point.

A description of the TACAN measurements made by JSC is given in Appendix A.

6.0 GPS PN CODE ACQUISITION

The GPS signal structure utilizes an acquisition code, the C/A code, to enable signal acquisition to occur in a reasonably short time. Nonetheless, since the acquisition code itself is a PN code, of length 1023 chips, the Shuttle GPS receiver must utilize a code search procedure to find the correct phase of the code for code acquisition. Two candidate code search and acquisition procedures for the Shuttle GPS receiver are discussed and analyzed here. The second of these procedures, the sequential search technique, is found to offer a performance advantage over the first technique, the fixed step search. Consequently, the performance of the sequential search technique is optimized by optimum selection of the detector parameters. Furthermore, the effect of the Shuttle doppler on the search time is analyzed.

6.1 PN Acquisition Time Performance of the Shuttle/GPS Receiver in the Presence of Shuttle Signal Dynamics With a Fixed Step Size Search

6.1.1 Introduction

The Shuttle/GPS receiver is responsible for extracting the range and range rate data from the GPS transmitted signals. This is accomplished by cross-correlating the received signal plus noise with locally generated reference codes and searching for the position of maximum correlation. Upon receiving an indication of this maximum correlation position, the receiver then enters a search/lock strategy during which time a code tracking loop is enabled to complete the acquisition process and begin tracking the code. After removing the C/A and P codes from the received signal, the two L-band carriers can then be acquired and tracked by some form of suppressed carrier tracking loop (e.g., an AFC aided Costas loop). Finally, when both carrier and codes have been acquired and the corresponding loops are tracking, the data may be detected.

The complete acquisition/track sequence (code and carrier) for each satellite on each L-band carrier must be performed in the presence of various Shuttle signal dynamics (e.g., center of gravity (CG) dynamics and dynamics about the pitch axis). The first question that must be answered is whether or not aiding is required and, if so, how much.

This report begins an attempt to specify the required aiding by focusing on the code acquisition aspect of the acquisition/track problem. In particular, the PN code acquisition process is modeled as a single dwell time system as in [2], and expressions for the mean time to acquire code phase in the presence of doppler, doppler rate, and finite duration jerk (doppler acceleration) are developed. A single dwell time system is one in which only a single fixed time integration (dwell time) is utilized in the code search process, as opposed to a double dwell time search [2] which has two integration periods—one to quickly search for the correct code phase and the second to provide an improved estimate of whether the correct code phase has been found. The next section briefly reviews the Markov chain model of the single dwell time system developed in great detail in [2].

6.1.2 Markov Chain Acquisition Model of the Single Dwell Time System

Consider the simple model of a single dwell time PN acquisition system illustrated in Figure 29. Since the PN code is acquired without knowledge of the carrier phase, the model employs a standard type, noncoherent (square-law) detector. Briefly, the received signal-plus-noise is amplified and then correlated with a local replica of the PN code, the correlation being performed by a multiplier followed by a bandpass filter. The filter output is then square-law detected with the detector output being integrated for a fixed time duration τ_D (the "dwell time") in an integrate-and-dump circuit.

The Markov chain nature of the acquisition model stems from the way in which the integrate-and-dump (I&D) output is processed. In particular, if the I&D output is above a preset threshold, then a "hit" is declared and the system enters a verification mode. If this hit represents a true hit (i.e., the correct code phase has been determined), then the system has officially acquired and the search comes to an end. If the hit is a false alarm, then verification cannot be consummated and the search must continue. In either case, we shall assume (as in [2]) that the verification is characterized by an extended dwell time (e.g., $k\tau_D$ sec; $k \gg 1$) and an entering into the code tracking loop mode. Understanding that a true hit corresponds to a single code phase position and this can only occur once per search through the code, we can regard the time interval $k\tau_D$ sec as the "penalty" of obtaining a false alarm, since a false alarm can occur on any code phase position. If the I&D output falls below the preset threshold, then the local PN code generator steps to its next position and the search proceeds. Thus, at each test position (aside from the single true code phase position), one of two events can occur, each characterized by a probability of occurrence; namely, a false alarm can occur with probability P_{FA}, causing a penalty of $k\tau_D$ sec, or no false alarm occurs with probability $(1 - P_{FA})$, resulting in only a single dwell time of τ_D sec—hence, the Markov chain model.

The time to acquire T, i.e., the time to declare a true hit, is a random variable and, in general, depends on the initial (at the beginning of the search) code phase position of the local PN generator relative to that of the received code. Since the probability distribution of T is difficult to obtain in practice, one ordinarily is content with determining

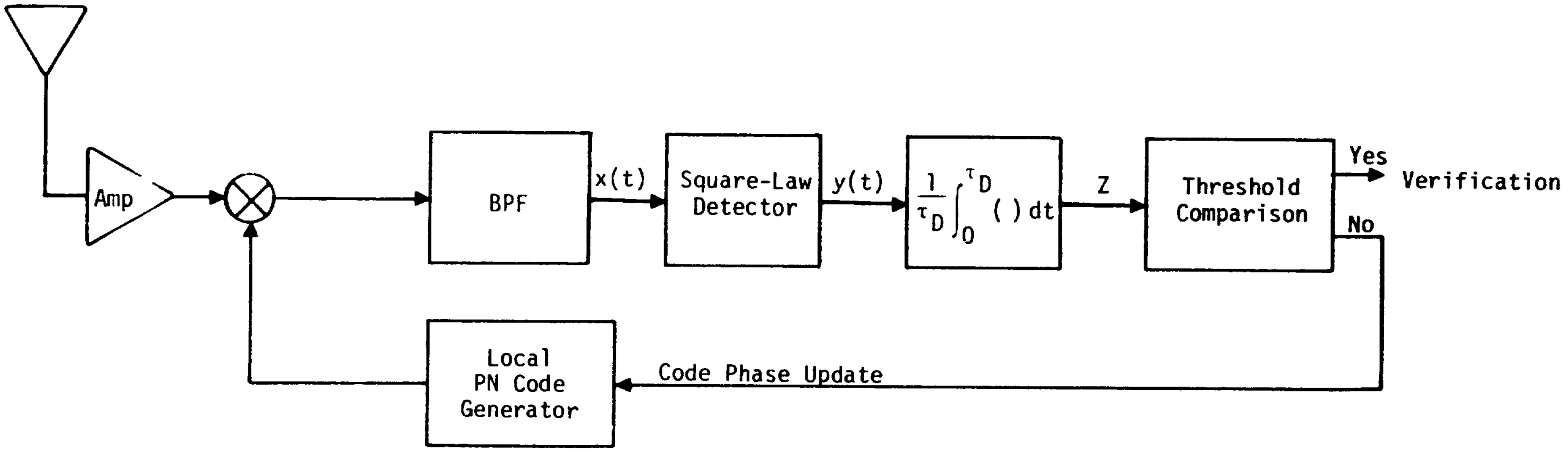

Figure 29. Block Diagram of a Single Dwell Time PN Acquisition System

the mean acquisition time $\bar{T}$ and, in the absence of a priori knowledge concerning the relative code phase positions of the received and locally generated codes, the local PN generator is assumed to start the search at any code phase position with equal probability. Stated in mathematical terms, letting q denote the number of cells (phase update positions of the local code replica) to be searched, then the probability P_1 of having the signal present (true hit) in the first cell searched is 1/q, and the probability of it not being present there is 1 - 1/q. For example, if the number of code chips to be searched is denoted by N and the search proceeds in half-chip increments, then $q = 2N$ and $P_1 = 1/2N$. More generally, if it has been determined that the signal is not present in the first k-1 cells, then the a priori probability P_k of finding it present in the kth cell is $1/(q+1-k)$, where $(q+1-k)$ is obviously the number of remaining cells to be searched, each possessing an equal probability of having the signal present.

6.1.3 Mean Acquisition Time Performance

a. No Code Doppler

Using the above Markov chain model, the mean acquisition time of the single dwell system is determined in [2], with the result (for large q):

$$\bar{T} = \frac{(2 - P_D)(1 + K P_{FA})}{2 P_D} q \tau_D , \qquad (1)$$

where P_D is the probability of detection (determining a true hit when, in fact, the local code replica is at the correct code phase position). Furthermore, the result in (1) assumes that no code doppler is present and that P_D is time invariant. Although idealized insofar as its assumptions, the result in (1) can be modified to reflect actual hardware or software systems. These modifications are discussed in [2] and are also germane to the extensions which follow.

b. Code Doppler

When code doppler is present, the acquisition time performance of the system of Figure 29 is affected in two ways. First, the code doppler causes the relative code phase between received and locally generated PN codes to be time varying during the dwell time of the integrate-and-dump. This has the effect of increasing or decreasing the probability of detection P_D, depending on whether the code doppler is causing the relative code phase to increase or decrease. The second and potentially more dominant effect is that code doppler affects the average search rate. In fact, if the code phase shift caused by the doppler over a single dwell time is equal to the step size (phase update) of the search, then the average search rate is reduced to zero.

To take both of these effects into account when computing mean acquisition time is indeed a difficult, if not impossible, analytical task. However, it is possible to account for just the effect of doppler on average search rate in a way which represents an obvious extension of the result in (1). Letting Δf_c denote the code doppler in chips/sec and T_c the chip interval in sec, then the mean search (code phase) update μ in chips is given by [2]:

$$\mu = \frac{\Delta T_c}{T_c} + \Delta f_c \tau_D + \Delta f_c K \tau_D P_{FA} , \tag{2}$$

where $\Delta T_c/T_c$ represents the search update in the absence of doppler or, equivalently, the step size of the search in fractions of a chip; $\Delta f_c \tau_D$ is the code phase shift due to doppler during the dwell time; and $\Delta f_c K \tau_D$ is the code phase shift during verification caused by a false alarm. Thus, replacing q by N/μ in (1) gives an expression for mean acquisition time in the presence of code doppler, namely [2],

$$\bar{T} = \frac{(2 - P_D)(1 + K P_{FA})\, N \tau_D}{2 P_D \left[\frac{\Delta T_c}{T_c} + \Delta f_c \tau_D (1 + K P_{FA})\right]} . \tag{3}$$

Since Δf_c can be either positive or negative, then depending upon its sign, the code doppler can either speed up or slow down the search. With regard to the magnitude of the code doppler, we shall assume that $|\Delta f_c| \tau_D (1 + K P_{FA}) \ll \Delta T_c/T_c$, so that the denominator of (3) never approaches zero and the search always proceeds in the direction dictated by the code phase update provided by the local PN generator. Finally, note that, when $\Delta f_c = 0$, then $\Delta T_c/T_c = N/q$ and (3) reduces to (1) as it should.

c. Code Doppler and Doppler Rate

The way in which code doppler is accounted for in extending the result of (1) to that given in (3) can also be applied to further extend (1) to include the effect of code doppler rate. In particular, we shall compute the mean search update analogous to (2) and again replace q by N/μ in the expression for mean acquisition time.

When code doppler alone was present, we observed that the mean (statistical) search update was time invariant, i.e., the expression in (2) characterizes every cell being searched. When, in addition, code doppler is present, the mean search update is now time dependent in the sense that it is now a function of the cell being searched. Thus, we start our analysis of this case by examining the mean search update in the first and second cells from which we shall find a general expression that characterizes this quantity in the ith cell, $1 \leq i \leq q$.

In general, the mean search update μ in any given search cell is equal to the nominal search update $\Delta T_c/T_c$ (typically, 1/2 for half-chip search increments) of the local PN code generator plus the mean change in phase of the received code over the search time of that cell.* Thus, letting μ_1 denote the mean search update in the first cell being searched, and $\Delta\dot{f}_c$ the code doppler rate in chips/sec^2, then from the Markov model previously established for the single dwell time system, we have that

$$\begin{aligned}\mu_1 &= \frac{\Delta T_c}{T_c} + \Delta f_c(1 - P_{FA}) \int_0^{\tau_D} dt + \Delta f_c P_{FA} \int_0^{(K+1)\tau_D} dt \\ &\quad + \Delta\dot{f}_c(1 - P_{FA}) \int_0^{\tau_D} t\, dt + \Delta\dot{f}_c P_{FA} \int_0^{(K+1)\tau_D} t\, dt \\ &= \frac{\Delta T_c}{T_c} + \Delta f_c \tau_D(1 + K P_{FA}) + \frac{1}{2}\Delta\dot{f}_c \tau_D^2 [1 + P_{FA}(K^2 + 2K)] \;. \qquad (4)\end{aligned}$$

Similarly, in the second cell to be searched, the mean search update μ_2 would be given by

---

[*] We continue to assume, as before, that the code phase derivatives are positive when they are in such a direction as to aid the search (reduce the acquisition time).

$$\begin{aligned}\mu_2 = {} & \frac{\Delta T_c}{T_c} + \Delta f_c(1-P_{FA})\left[(1-P_{FA})\int_{\tau_D}^{2\tau_D} dt + P_{FA}\int_{\tau_D}^{(K+2)\tau_D} dt\right] \\ & + \Delta f_c P_{FA}\left[(1-P_{FA})\int_{(K+1)\tau_D}^{(K+2)\tau_D} dt + P_{FA}\int_{(K+1)\tau_D}^{2(K+1)\tau_D} dt\right] \\ & + \Delta \dot{f}_c(1-P_{FA})\left[(1-P_{FA})\int_{\tau_D}^{2\tau_D} t\,dt + P_{FA}\int_{\tau_D}^{(K+2)\tau_D} t\,dt\right] \\ & + \Delta \dot{f}_c P_{FA}\left[(1-P_{FA})\int_{(K+1)\tau_D}^{(K+2)\tau_D} t\,dt + P_{FA}\int_{(K+1)\tau_D}^{2(K+1)\tau_D} t\,dt\right] \\ = {} & \frac{\Delta T_c}{T_c} + \Delta f_c\,\tau_D(1+KP_{FA}) + \frac{1}{2}\Delta \dot{f}_c\,\tau_D^2[1+P_{FA}(K^2+2K)] \\ & + \Delta \dot{f}_c[\tau_D(1+KP_{FA})]^2 . \qquad (5)\end{aligned}$$

To generalize (4) and (5) to an arbitrary search cell, we first observe that, for any time $t_0 > 0$,

$$(1-P_{FA})\int_{t_0}^{t_0+\tau_D} dt + P_{FA}\int_{t_0}^{t_0+(K+1)\tau_D} dt = \tau_D(1+KP_{FA}) \qquad (6)$$

and

$$\begin{aligned}&(1-P_{FA})\int_{t_0}^{t_0+\tau_D} t\,dt + P_{FA}\int_{t_0}^{t_0+(K+1)\tau_D} t\,dt \\ &\qquad = \frac{1}{2}(1-P_{FA})\left[(t_0+\tau_D)^2 - t_0^2\right] + \frac{1}{2}P_{FA}\left[(t_0+(K+1)\,\tau_D)^2 - t_0^2\right] \\ &\qquad = t\,\tau_D[1+KP_{FA}] + \frac{1}{2}\tau_D^2[1+P_{FA}(K^2+2K)] . \qquad (7)\end{aligned}$$

Thus, extending the Markov chain procedure leading to the expression for μ_2 and using (6) and (7), we arrive at the general expression for the mean search update μ_{n+1} of the n+1st cell, namely,

$$\begin{aligned}\mu_{n+1} = {} & \frac{\Delta T_c}{T_c} + \Delta f_c\,\tau_D(1+KP_{FA}) + \frac{1}{2}\Delta \dot{f}_c\,\tau_D^2[1+P_{FA}(K^2+2K)] \\ & + \Delta \dot{f}_c\,\tau_D(1+KP_{FA})\sum_{k=0}^{n} {}_kC_n\,P_{FA}^k(1-P_{FA})^{n-k}[(n-k)+k(K+1)] \qquad (8)\end{aligned}$$

where

$$ {}_kC_n \triangleq \frac{n!}{k!\,(n-k)!} \tag{9} $$

is the binomial coefficient. The third term in (8) can be further amplified as follows:

$$ \sum_{k=0}^{n} {}_kC_n\, P_{FA}^{k}(1-P_{FA})^{n-k}[(n-k)+k(K+1)] = \sum_{k=0}^{n} {}_kC_n\, P_{FA}^{k}(1-P_{FA})^{n-k}(n+kK)\,. \tag{10} $$

Since, from the properties of a binomial distribution,

$$ \sum_{k=0}^{n} {}_kC_n\, P_{FA}^{k}(1-P_{FA})^{n-k} = 1 $$

$$ \sum_{k=0}^{n} k\; {}_kC_n\, P_{FA}^{k}(1-P_{FA})^{n-k} = n\,P_{FA}\,, \tag{11} $$

then from (10) and (11), we have

$$ \sum_{k=0}^{n} {}_kC_n\, P_{FA}^{k}(1-P_{FA})^{n-k}[(n-k)+k(K+1)] = n + K n P_{FA} = n(1+KP_{FA})\,. \tag{12} $$

Finally, substituting (12) into (8) gives the desired simplified result:

$$ \mu_{n+1} = \frac{\Delta T_c}{T_c} + \Delta f_c\,\tau_D(1+KP_{FA}) + \frac{1}{2}\Delta\dot{f}_c\,\tau_D^2[1+P_{FA}(K^2+2K)] $$
$$ + n\,\Delta\dot{f}_c\,[\tau_D(1+KP_{FA})]^2\,; \quad n \geq 0\,. \tag{13} $$

Note from (13) that the mean search update is a linear function of the search cell. Because of this dependence on n, we cannot directly replace q by N/μ in (1) to arrive at a formula for mean acquisition in the presence of code doppler and doppler rate. Rather, we shall first find the <u>average mean search update</u> μ obtained by averaging μ_{n+1} of (13) over all q search cells, i.e.,

$$ \mu \triangleq \frac{1}{q}\sum_{n=0}^{q-1} \mu_{n+1} \tag{14} $$

and then make the above suggested replacement in (1). Thus, from (13) and (14), we have that

$$\begin{aligned}\mu &= \frac{\Delta T_c}{T_c} + \Delta f_c\,\tau_D(1 + K\,P_{FA}) + \frac{1}{2}\,\Delta\dot{f}_c\,\tau_D^{\,2}\,[1 + P_{FA}\,(K^2 + 2K)] \\ &\qquad + \left[\frac{1}{q}\sum_{n=0}^{q-1} n\right]\Delta\dot{f}_c\left[\tau_D\,(1 + K\,P_{FA})\right]^2 \\ &= \frac{\Delta T_c}{T_c} + \Delta f_c\,\tau_D(1 + K\,P_{FA}) + \frac{1}{2}\,\Delta\dot{f}_c\,\tau_D^{\,2}\,[1 + P_{FA}\,(K^2 + 2K)] \\ &\qquad + \left(\frac{q-1}{2}\right)\Delta\dot{f}_c\left[\tau_D(1 + K\,P_{FA})\right]^2 \\ &= \frac{\Delta T_c}{T_c} + \Delta f_c\,\tau_D(1 + K\,P_{FA}) + \frac{1}{2}\,\Delta\dot{f}_c\,\tau_D^{\,2}\,\{q(1 + K\,P_{FA})^2 + K^2\,P_{FA}(1 - P_{FA})\}. \qquad (15)\end{aligned}$$

Since the total mean search update must correspond to the total number of chips searched, we have that*

$$q\,\mu = \sum_{n=0}^{q-1} \mu_{n+1} = N\,. \qquad (16)$$

Thus, substituting N/μ for q in (15) results in a quadratic equation in μ, namely,

$$\mu^2 - \mu\left[\frac{\Delta T_c}{T_c} + \Delta f_c\,\tau_D(1 + K\,P_{FA}) + \frac{1}{2}\,\Delta\dot{f}_c\,\tau_D^{\,2}\,K^2\,P_{FA}(1 - P_{FA})\right] - \frac{1}{2}\,\Delta\dot{f}_c\,\tau_D^{\,2}\,N(1 + K\,P_{FA})^2 = 0\,. \qquad (17)$$

Letting

$$\begin{aligned}A &= 1 \\ B &= \frac{\Delta T_c}{T_c} + \Delta f_c\,\tau_D(1 + K\,P_{FA}) + \frac{1}{2}\,\Delta\dot{f}_c\,\tau_D^{\,2}\,K^2\,P_{FA}(1 - P_{FA}) \\ C &= \frac{1}{2}\,\Delta\dot{f}_c\,\tau_D^{\,2}\,N(1 + K\,P_{FA})^2\,, \qquad (18)\end{aligned}$$

then

---

*Here we have made the assumption that $|\Delta f_c|$ and $|\Delta\dot{f}_c|$ are small enough such that $\mu_{n+1} > 0$ for all $n = 0,1,\ldots,q-1$ and thus the search proceeds only in one direction, namely, that dictated by the local PN generator code phase update.

$$\mu = \frac{B}{2A}\left[1 + \sqrt{1 + \frac{4AC}{B^2}}\right] . \tag{19}$$

Finally, substituting N/μ for q in (1), with μ defined by (19), gives the resulting expression for mean acquisition time in the presence of code doppler and code doppler rate, namely,

$$\bar{T} = \frac{(2 - P_D)(1 + K P_{FA}) N \tau_D}{2 P_D \left[\dfrac{B\left(1 + \sqrt{1 + \dfrac{4AC}{B^2}}\right)}{2A}\right]} . \tag{20}$$

Note again that, when $\Delta f_c = \Delta \dot{f}_c = 0$, we have that $B = \Delta T_c/T_c = N/q$, $C = 0$, and (20) reduces to (1).

d. Code Doppler, Doppler Rate, and Doppler Acceleration (Jerk) Over a Finite Time Interval

When, in addition to code doppler and doppler rate, the received signal dynamics are characterized by a doppler acceleration or jerk over a finite interval of time, say, $0 \leq t \leq t_1$, then the received code phase $\theta/2\pi$ takes the form

$$\frac{\theta}{2\pi} = \begin{cases} \dfrac{\theta_0}{2\pi} + \Delta f_c t + \dfrac{1}{2}\Delta \dot{f}_c t^2 + \dfrac{1}{6}\Delta \ddot{f}_c t^3 ; & 0 \leq t \leq t_1 \\ \\ \dfrac{\theta_0}{2\pi} + \Delta f_c t + \dfrac{1}{2}\Delta \dot{f}_c t^2 + \dfrac{1}{6}\Delta \ddot{f}_c t^3 - \dfrac{1}{6}\Delta \ddot{f}_c (t - t_1)^3 ; & t_1 \leq t \leq \infty \end{cases} \tag{21}$$

where $\Delta \ddot{f}_c$ denotes the doppler acceleration. The second equation in (21) can be written in a more convenient form which identifies the effective code phase, doppler, and doppler rates, namely,

$$\begin{aligned} \frac{\theta}{2\pi} &= \frac{\theta_0}{2\pi} + \frac{1}{6}\Delta \ddot{f}_c t_1^3 + \left(\Delta f_c - \frac{1}{2}\Delta \ddot{f}_c t_1^2\right) t + \frac{1}{2}\left(\Delta \dot{f}_c + \Delta \ddot{f}_c t_1\right) t^2 ; \quad t_1 \leq t \leq \infty \\ &= \frac{\theta_0'}{2\pi} + \Delta f_c' t + \frac{1}{2}\Delta \dot{f}_c' t^2 . \end{aligned} \tag{22}$$

For convenience of analysis, we shall assume that the time duration of the jerk is an integer multiple of the dwell time, i.e., $t_1 = M\tau_d$; $M \geq 1$, and furthermore, less than the time duration penalty of a false alarm, i.e., $t_1 < (K+1)\tau_D$ or, equivalently, $M < K+1$. As before, we shall characterize, for the purpose of illustration, the mean search update in the first and second search intervals from which an expression valid for the ith search interval will become obvious. Finally, the (time) average mean search update will be computed and used to evalute the mean acquisition time performance of the single dwell system in the presence of code doppler, doppler rate, and finite time duration jerk.

In the first code search interval, the mean search update μ_1 is now given by

$$\begin{aligned}
\mu_1 &= \frac{\Delta T_c}{T_c} + \Delta f_c(1 - P_{FA}) \int_0^{\tau_D} dt + \Delta f_c P_{FA} \int_0^{M\tau_D} dt \\
&\quad + \Delta f_c' P_{FA} \int_{M\tau_D}^{(K+1)\tau_D} dt + \Delta \dot{f}_c (1 - P_{FA}) \int_0^{\tau_D} t\, dt \\
&\quad + \Delta \dot{f}_c P_{FA} \int_0^{M\tau_D} t\, dt + \Delta \dot{f}_c' P_{FA} \int_{M\tau_D}^{(K+1)\tau_D} t\, dt \\
&\quad + \frac{1}{2} \Delta \ddot{f}_c (1 - P_{FA}) \int_0^{\tau_D} t^2\, dt + \frac{1}{2} \Delta \ddot{f}_c P_{FA} \int_0^{M\tau_D} t^2\, dt \\
&= \frac{\Delta T_c}{T_c} + \Delta f_c \tau_D (1 + K P_{FA}) + \frac{1}{2} \Delta \dot{f}_c \tau_D^2 [1 + P_{FA}(K^2 + 2K)] \\
&\quad - \frac{1}{2} \Delta \ddot{f}_c M^2 \tau_D^3 \left\{(1 + K P_{FA}) - [(1 - P_{FA}) + P_{FA} M]\right\} \\
&\quad + \frac{1}{2} \Delta \ddot{f}_c M \tau_D^3 \left\{[1 + P_{FA}(K^2 + 2K)] - [(1 - P_{FA}) + P_{FA} M^2]\right\} \\
&\quad + \frac{1}{6} \Delta \ddot{f}_c \tau_D^3 [(1 - P_{FA}) + P_{FA} M^3] . \qquad (23)
\end{aligned}$$

Note that, when $\Delta \ddot{f}_c = 0$, then (23) reduces to (4). In the second search interval, the mean search update is similarly given by

$$\begin{aligned}\mu_2 = \frac{\Delta T_c}{T_c} &+ (1 - P_{FA}) \left[(1 - P_{FA}) \int_{\tau_D}^{2\tau_D} (\Delta f_c + \Delta\dot{f}_c t + \frac{1}{2} \Delta\ddot{f}_c t^2)\, dt \right. \\ &\qquad \left. + P_{FA} \int_{\tau_D}^{M\tau_D} (\Delta f_c + \Delta\dot{f}_c t + \frac{1}{2} \Delta\ddot{f}_c t^2)\, dt \right] \\ &+ (1 - P_{FA}) P_{FA} \int_{M\tau_D}^{(K+1)\tau_D} (\Delta f_c' + \Delta\dot{f}_c' t)\, dt \\ &+ P_{FA} \left[(1 - P_{FA}) \int_{(K+1)\tau_D}^{(K+2)\tau_D} (\Delta f_c' + \Delta\dot{f}_c' t)\, dt \right. \\ &\qquad \left. + P_{FA} \int_{(K+1)\tau_D}^{2(K+1)\tau_D} (\Delta f_c' + \Delta\dot{f}_c' t)\, dt \right] , \qquad (24)\end{aligned}$$

which upon simplification becomes

$$\begin{aligned}\mu_2 = \frac{\Delta T_c}{T_c} &+ \Delta f_c \tau_D (1 + K P_{FA}) + \frac{1}{2} \Delta\dot{f}_c \tau_D^2 [1 + P_{FA}(K^2 + 2K)] \\ &+ \Delta\dot{f}_c [\tau_D (1 + K P_{FA})]^2 - \frac{1}{2} \Delta\ddot{f}_c M^2 \tau_D^3 \\ &\qquad \times \left\{ (1 + K P_{FA}) - (1 - P_{FA})[(1 - P_{FA}) + P_{FA}(M - 1)] \right\} \\ &+ \Delta\ddot{f}_c M \tau_D^3 \left\{ (1 + K P_{FA})^2 + \frac{1}{2} [1 + P_{FA}(K^2 + 2K)] \right\} \\ &- \frac{1}{2} \Delta\ddot{f}_c M \tau_D^3 (1 - P_{FA}) [3(1 - P_{FA}) + P_{FA}(M^2 - 1)] \\ &+ \frac{1}{6} \Delta\ddot{f}_c \tau_D^3 (1 - P_{FA}) [7(1 - P_{FA}) + P_{FA}(M^3 - 1)] . \qquad (25)\end{aligned}$$

Once again, when $\Delta\ddot{f}_c = 0$, (25) reduces to (5). Extending this Markov chain approach to the n+1st cell, we arrive at the general expression characterizing the mean search update μ_{n+1} of this cell, namely,

$$\mu_{n+1} = \frac{\Delta T_c}{T_c} + \Delta f_c \tau_D (1 + K P_{FA}) + \frac{1}{2} \Delta \dot{f}_c \tau_D^2 [1 + P_{FA}(K^2 + 2K)]$$

$$+ n\Delta \dot{f}_c [\tau_D (1 + K P_{FA})]^2 - \frac{1}{2} \Delta \ddot{f}_c M^2 \tau_D^3 \left\{(1 + K P_{FA}) - (1 - P_{FA})^n [(1 - P_{FA}) + P_{FA}(M-n)]\right\}$$

$$+ \Delta \ddot{f}_c M \tau_D^3 \left\{n(1 + K P_{FA})^2 + \frac{1}{2}[1 + P_{FA}(K^2 + 2K)]\right\}$$

$$- \frac{1}{2} \Delta \ddot{f}_c M \tau_D^3 (1 - P_{FA})^n [(1 - P_{FA})(2n + 1) + P_{FA}(M^2 - n^2)]$$

$$+ \frac{1}{6} \Delta \ddot{f}_c \tau_D^3 (1 - P_{FA})^n \underbrace{[(1 - P_{FA})(3n^2 + 3n + 1) + P_{FA}(M^3 - n^3)]}_{(1 - P_{FA})(n+1)^3 + P_{FA} M^3 - n^3}; \quad 0 \leq n \leq M-1 \qquad (26a)$$

and

$$\mu_{n+1} = \frac{\Delta T_c}{T_c} + \Delta f_c' \tau_D (1 + K P_{FA}) + \frac{1}{2} \Delta \dot{f}_c' \tau_D^2 [1 + P_{FA}(K^2 + 2K)]$$

$$+ n\Delta \dot{f}_c' [\tau_D (1 + K P_{FA})]^2; \qquad n \geq M. \qquad (26b)$$

Using the definition of average mean search update μ given in (14), then substituting (26) into this equation gives

$$\mu = \frac{\Delta T_c}{T_c} + \Delta f_c' \tau_D (1 + K P_{FA}) + \frac{1}{2} \Delta \dot{f}_c' \tau_D^2 [1 + P_{FA}(K^2 + 2K)]$$

$$+ \left[\frac{1}{q} \sum_{n=0}^{q-1} n\right] \Delta \dot{f}_c' [\tau_D (1 + K P_{FA})]^2 + \frac{1}{2} \Delta \ddot{f}_c M^2 \tau_D^3$$

$$\times \left\{[(1 - P_{FA}) + M P_{FA}] \left[\frac{1}{q} \sum_{n=0}^{M-1} (1 - P_{FA})^n\right] - P_{FA} \left[\frac{1}{q} \sum_{n=0}^{M-1} n (1 - P_{FA})^n\right]\right\}$$

$$- \frac{1}{2} \Delta \ddot{f}_c M \tau_D^3 \left\{[1 - P_{FA}) + M^2 P_{FA}] \left[\frac{1}{q} \sum_{n=0}^{M-1} (1 - P_{FA})^n\right]\right.$$

$$\left. + 2(1 - P_{FA}) \left[\frac{1}{q} \sum_{n=0}^{M-1} n(1 - P_{FA})^n\right] - P_{FA} \left[\frac{1}{q} \sum_{n=0}^{M-1} n^2 (1 - P_{FA})^n\right]\right\}$$

$$+ \frac{1}{6} \Delta \ddot{f}_c \tau_D^3 \left\{\frac{1}{q} \sum_{n=1}^{M} n^3 (1 - P_{FA})^n - \frac{1}{q} \sum_{n=0}^{M-1} n^3 (1 - P_{FA})^n + M^3 P_{FA} \left[\frac{1}{q} \sum_{n=0}^{M-1} (1 - P_{FA})^n\right]\right\}. \qquad (27)$$

From the summation properties of arithmetic and geometric series, we have that

$$\sum_{n=0}^{q-1} n = \frac{q(q-1)}{2}$$

$$\sum_{n=0}^{M-1} (1-P_{FA})^n = \frac{1-(1-P_{FA})^M}{P_{FA}}$$

$$\sum_{n=0}^{M-1} n(1-P_{FA})^n = \frac{(1-P_{FA})[1-(1-P_{FA})^{M-1}]}{P_{FA}^{\,2}} - \frac{(M-1)(1-P_{FA})^M}{P_{FA}}$$

$$\sum_{n=0}^{M-1} n^2(1-P_{FA})^n = (1-P_{FA})\left\{\frac{P_{FA}[1-M(1-P_{FA})^{M-1}] + 2(1-P_{FA})[1-(1-P_{FA})^{M-1}]}{P_{FA}^{\,3}}\right\}$$

$$- (M-1)(1-P_{FA})\left\{\frac{P_{FA}M(1-P_{FA})^{M-1} + (1-P_{FA})^M}{P_{FA}^{\,2}}\right\}$$

$$\sum_{n=1}^{M} n^3(1-P_{FA})^n - \sum_{n=0}^{M-1} n^3(1-P_{FA})^n = M^3(1-P_{FA})^M . \qquad (28)$$

Substituting (28) into (27) and simplifying yields

$$\mu = \frac{\Delta T_c}{T_c} + \Delta f_c' \tau_D (1 + K P_{FA}) + \frac{1}{2} \Delta \dot{f}_c' \tau_D^{\,2} \left\{q(1+K P_{FA})^2 + K^2 P_{FA}(1-P_{FA})\right\}$$

$$+ \frac{1}{6q} \Delta \ddot{f}_c M^3 \tau_D^{\,3} . \qquad (29)$$

Comparing (29) with (15), we observe that the effect of the finite duration doppler jerk on the average mean search update is simply the addition of the term $\Delta \ddot{f}_c M^3 \tau_D^{\,3}/(6q)$, which is <u>inversely</u> proportional to the number of search intervals q.

Letting $q = N/\mu$ as in (16), we once again get a quadratic equation in μ, namely,

$$\mu^2\left[1 - \frac{1}{6N}\Delta\ddot{f}_c M^3 \tau_D^3\right] - \mu\left[\frac{\Delta T_c}{T_c} + \Delta f_c{}' \tau_D(1 + K P_{FA}) + \frac{1}{2}\Delta\dot{f}_c{}' \tau_D^3 K^2 P_{FA}(1 - P_{FA})\right]$$

$$- \frac{1}{2}\Delta\dot{f}_c{}' \tau_D^2 N(1 + K P_{FA})^2 = 0. \qquad (30)$$

Letting

$$A = 1 - \frac{1}{6N}\Delta\ddot{f}_c M^3 \tau_D^3$$

$$B = \frac{\Delta T_c}{T_c} + \Delta f_c{}' \tau_D (1 + K P_{FA}) + \frac{1}{2}\Delta\dot{f}_c{}' \tau_D^2 K^2 P_{FA}(1 - P_{FA})$$

$$C = \frac{1}{2}\Delta\dot{f}_c{}' \tau_D^2 N(1 + K P_{FA})^2. \qquad (31)$$

with, as a reminder [see (22) with $t_1 = M\tau_D$],

$$\Delta f_c{}' = \Delta f_c - \frac{1}{2}\Delta\ddot{f}_c M^2 \tau_D^2$$

$$\Delta\dot{f}_c{}' = \Delta\dot{f}_c + \Delta\ddot{f}_c M \tau_D, \qquad (32)$$

then the mean acquisition time $\bar{T}$ is once again given by (20) with A, B, and C now as defined in (31).

6.1.4 Evaluation of Detection Probability P_D and False Alarm Probability P_{FA} in Terms of PN Acquisition System Parameters

The formulas for mean acquisition time developed in the previous section are all functions of the detection probability P_D, false alarm probability P_{FA}, and dwell time τ_D. Thus, it would appear at first glance that, for specified values of detection probability and false alarm probability, one could arbitrarily select the dwell time to achieve any desired mean acquisition time. Upon closer examination, one realizes that indeed this is not possible with the fallacy lying in the fact that, for a given P_{FA} and predetection signal-to-noise ration, P_D is implicitly a function of τ_D. To place this statement in evidence, we begin by evaluating P_D and P_{FA} in terms of the PN acquisition system parameters for the simple case of no code doppler or doppler derivatives. Following this, we shall generalize these results to correspond more realistically to the Shuttle signal dynamics.

a. No Code Doppler

When signal is present (i.e., the cell being searched corresponds to a sample value on the PN correlation curve), then the input to the square-law detector can be expressed in the form

$$\begin{aligned} x(t) &= s(t)+n(t) = \sqrt{2}\,A\cos(\omega_0 t+\psi)+\sqrt{2}\,n_c(t)\cos(\omega_0 t+\psi) \\ &\qquad - \sqrt{2}\,n_s(t)\sin(\omega_0 t+\psi) \\ &= \sqrt{2}\,R(t)\cos\left(\omega_0 t+\psi+\theta(t)\right), \end{aligned} \tag{33}$$

where

$$R(t) = \sqrt{(A+n_c(t))^2+n_s^2(t)}\ ; \quad \theta(t) = \tan^{-1}\frac{n_s(t)}{A+n_c(t)}\,. \tag{34}$$

In (33), A is the rms signal amplitude,* ω_0 the radian carrier frequency, and $n_c(t)$, $n_s(t)$ are bandlimited, independent, low pass, zero mean Gaussian noise processes with variance $\sigma^2 = N_0B$, where N_0 is the single-sided noise spectral density and B is the noise bandwidth of the pre-detection bandpass filter.

The output of the square-law device in Figure 1 in response to the input x(t) of (33) is (ignoring second harmonics of the carrier):

$$y(t) \triangleq x^2(t) = R^2(t) = (A+n_c(t))^2+n_s^2(t) \tag{35}$$

and has a first order probability density function (pdf) which is given by

$$p(y) = \begin{cases} \dfrac{1}{\sigma^2}\exp\left[-\left(\dfrac{y}{\sigma^2}+\gamma\right)\right] I_0\left(2\sqrt{\dfrac{\gamma y}{\sigma^2}}\right); & y \geq 0 \\ 0\ ; & \text{otherwise} \end{cases} \tag{36}$$

---

*For the moment, we shall not enter into a discussion concerning the various system losses and gains which enter into the calculation of the effective signal amplitude to be used in predicting true system signal-to-noise ratio behavior. Such a discussion will be given later on in the development.

where $I_0(x)$ is the zero order modified Bessel function of the first kind and

$$\gamma \triangleq \frac{A^2}{N_0 B} \tag{37}$$

is the predetection signal-to-noise ratio. In the absence of signal, i.e., $A = 0$, (36) reduces to the chi-squared pdf:

$$p(y) = \begin{cases} \frac{1}{\sigma^2} \exp\left(-\frac{y}{\sigma^2}\right); & y \geq 0 \\ 0; & \text{otherwise} \end{cases} \tag{38}$$

which characterizes the square-law output in all search cells which contain noise only.

If $y(t)$ is sampled at intervals $T = 1/B$, then these samples are approximately independent, and furthermore, the integrate-and-dump output can be approximated by a summation over these sampled values, namely,

$$Z \triangleq \frac{1}{\tau_D} \int_0^{\tau_D} y(t)\,dt \cong \frac{1}{N_B} \sum_{k=0}^{N_B - 1} y(kT) \tag{39}$$

where*

$$N_B \triangleq \frac{\tau_D}{T} = B\tau_D . \tag{40}$$

Using the approximation in (39) and the first order pdf's of (36) and (38), the pdf of Z, namely, p(Z), for signal present is given by

$$p(Z) = \begin{cases} \frac{N_B}{\sigma^2} \left(\frac{Z}{\gamma\sigma^2}\right)^{(N_B-1)/2} \exp\left[-N_B\left(\frac{Z}{\sigma^2} - \gamma\right)\right] I_{N_B-1}\left[2\sqrt{N_B^2 \gamma \frac{Z}{\sigma^2}}\right]; & Z \geq 0 \\ 0; & \text{otherwise} \end{cases} \tag{41}$$

and for signal absent is given by

---

[*] It is convenient here to assume that N_B is integer, although the results which follow are, for large N_B, valid for N_B noninteger.

$$p(Z) = \begin{cases} \dfrac{\left(\dfrac{Z N_B}{\sigma^2}\right)^{N_B - 1}}{(N_B - 1)!} \exp\left(-\dfrac{Z N_B}{\sigma^2}\right) ; & Z \geq 0 \\ 0 ; \quad \text{otherwise} \end{cases} \tag{42}$$

In (41), $I_{N_B - 1}(x)$ is the $(N_B - 1)$st order modified Bessel function of the first kind.

Normalizing Z by $\sigma^2/N_B = N_0/\tau_D$ or, equivalently, letting $Z^* \triangleq Z N_B/\sigma^2$, we can rewrite (41) and (42), respectively, in the simpler form,

$$p(Z^*) = \begin{cases} \left(\dfrac{Z^*}{N_B \gamma}\right)^{(N_B - 1)/2} \exp(-Z^* - N_B \gamma) I_{N_B - 1}\left[2\sqrt{N_B \gamma Z^*}\right] ; & Z^* \geq 0 \\ 0 ; \quad \text{otherwise} \end{cases} \tag{43}$$

and

$$p(Z^*) = \begin{cases} \dfrac{(Z^*)^{(N_B - 1)/2}}{(N_B - 1)!} \exp(-Z^*) ; & Z^* \geq 0 \\ 0 ; \quad \text{otherwise} \end{cases} \tag{44}$$

The probability of false alarm, P_{FA}, is the probability that Z exceeds the threshold η when signal is absent or, equivalently, in terms of the normalized random variable Z^* and the normalized threshold $\eta^* \triangleq \eta N_B/\sigma^2$,

$$\begin{aligned} P_{FA} &= \int_{\eta^*}^{\infty} p(Z^*)\, dZ^* = 1 - \int_0^{\eta^*} \frac{(Z^*)^{(N_B - 1)/2}}{(N_B - 1)!} \exp(-Z^*)\, dZ^* \\ &= e^{-\eta^*} \sum_{k=0}^{N_B - 1} \frac{(\eta^*)^k}{k!} . \end{aligned} \tag{45}$$

The detection probability P_D is the probability that Z exceeds the threshold η when signal is present. Thus, using (43) rather than (44), we get

$$P_D = 1 - \int_0^{\eta^*} \left(\frac{Z^*}{N_B\gamma}\right)^{(N_B-1)/2} \exp(-Z^* - N_B\gamma)\, I_{N_B-1}\left[2\sqrt{N_B\gamma Z^*}\right] dZ^* \tag{46}$$

which cannot be put into a closed-form expression.

For large N_B (the case of most practical interest), things become quite a bit simpler. Defining $y_k^* = y(kT)/\sigma^2$, then from (36) and (38), the pdf's of y_k^* in the presence and absence of signal are, respectively,

$$p(y_k^*) = \begin{cases} e^{-(y_k^*+\gamma)} I_0\left(2\sqrt{\gamma y_k^*}\right); & y_k^* \geq 0 \\ 0; & \text{otherwise} \end{cases} \tag{47}$$

$$p(y_k^*) = \begin{cases} e^{-y_k^*}; & y_k^* \geq 0 \\ 0; & \text{otherwise} \end{cases} \tag{48}$$

Also, from (39) and the definition of Z^* in terms of Z, we have

$$Z^* = \sum_{k=0}^{N_B-1} y_k^* . \tag{49}$$

Since, by previous assumption, the y_k^*'s are independent random variables, then for large N_B, Z^* is approximately Gaussian distributed with mean $\overline{Z^*} = N_B \overline{y^*}$ and variance $\sigma_{Z^*}^2 = N_B \sigma_{y^*}^2$. The means and variance of the pdf's in (47) and (48) are well known [3] to be

$$\overline{y^*} = 1+\gamma ; \quad \sigma_{y^*}^2 = 1+2\gamma ; \quad \text{signal present} \tag{50}$$

$$\overline{y^*} = 1 ; \quad \sigma_{y^*}^2 = 1 ; \quad \text{signal absent} . \tag{51}$$

Thus,

$$\overline{Z^*} = N_B(1+\gamma) ; \quad \sigma_{Z^*}^2 = N_B(1+2\gamma) ; \quad \text{signal present} \tag{52}$$

$$\overline{Z^*} = N_B ; \quad \sigma_{Z^*}^2 = N_B ; \quad \text{signal absent} . \tag{53}$$

Using the Gaussian assumption, the false alarm probability is

$$P_{FA} = \int_{\eta^*}^{\infty} \frac{1}{\sqrt{2\pi N_B}} \exp\left[-\frac{(Z^* - N_B)^2}{2N_B}\right] dZ^*$$

$$= \frac{1}{2} \operatorname{erfc}\left[\frac{\eta^* - N_B}{\sqrt{2 N_B}}\right]$$

$$= \frac{1}{2} \operatorname{erfc} \beta , \tag{54}$$

where

$$\operatorname{erfc} x \triangleq \frac{2}{\sqrt{\pi}} \int_{x}^{\infty} \exp(-t^2)\, dt . \tag{55}$$

Thus, if P_{FA} is specified, β can be determined. The corresponding detection probability under the same assumption is

$$P_D = \int_{\eta^*}^{\infty} \frac{1}{\sqrt{2\pi N_B(1+2\gamma)}} \exp\left[-\frac{\left(Z^* - N_B(1+\gamma)\right)^2}{2N_B(1+2\gamma)}\right] dZ^*$$

$$= \frac{1}{2} \operatorname{erfc}\left[\frac{\eta^* - N_B(1+\gamma)}{\sqrt{2 N_B (1+2\gamma)}}\right]$$

$$= \frac{1}{2} \operatorname{erfc}\left[\frac{\beta - \sqrt{\frac{N_B}{2}}\,\gamma}{\sqrt{1+2\gamma}}\right] . \tag{56}$$

Combining (54) and (56) and reidentifying N_B and γ in terms of system parameters gives the final relation

$$P_D = \frac{1}{2} \operatorname{erfc}\left[\frac{\operatorname{erfc}^{-1}(2P_{FA}) - \sqrt{\frac{B\tau_D}{2}}\left(\frac{A^2}{N_0 B}\right)}{\sqrt{1 + 2\left(\frac{A^2}{N_0 B}\right)}}\right] . \tag{57}$$

Thus, given P_D, P_{FA}, A^2/N_0 and B, the dwell time τ_D is determined.

Before using (57) and the dwell time determined from it in the formulas derived in the previous section for mean acquisition time, several modifications based upon practical considerations must be made.

(1) Effective Probability of Detection and Timing Misalignment

The calculation of detection probability as in (46) or (56) implicitly assumed that only one cell in the entire search satisfies the "signal present" hypothesis. In actuality, since the PN correlation curve exists over an interval of ±1 chip around the peak, then, for example, a system which update the locally generated code phase in half-chip increments would yield several cells for which signal could be considered present.

Typically, the system is designed on the basis of the worst case correlation, which for the half-chip update case would correspond to the pair of correlation points one-quarter chip away from the correlation peak. Since the normalized correlation value at these points is 0.75 (relative to a peak of 1), then the single signal point calculation of detection probability as in (46) or (56) would be based on an effective reduction in the nominal signal-to-noise ratio A^2/N_0 of $10 \log_{10}(.75)^2 \doteq 2.5$ dB. Since, however, in reality there exist two worst case correlation positions, then the effective probability of detection P_D' for use in computing mean acquisition time is computed as:

$$P_D' = P_D + (1 - P_D) P_D = 2P_D - P_D^2 , \tag{58}$$

where the first term in (58) represents the probability of detecting signal present on the first correlation point and the second term is the joint probability of not detecting signal on the first correlation point and detecting signal present on the second correlation point. Clearly, for low signal-to-noise ratios (small P_D), the effective detection probability is approximately twice that computed on the basis of a single signal present cell [(46) or (56)]. In summary, then, the computation procedures would be as follows. For a given P_{FA}, determine β from (54). For a specified P_D', find P_D from (57), degrade the given nominal value of γ by 2.5 dB and solve for N_B in (56). Determine the dwell time from $\tau_D = N_B/B$, where B is the given bandpass filter bandwidth determined by considerations on allowable modulation distortion (to be discussed next). Using P_D', P_{FA}, and τ_D in (1), solve for $\hat{T}$.

(2) Modulation Distortion Effects

Typically, the PN modulated carrier is also biphase modulated by data. Depending on the ratio of predetection filter bandwidth B to data rate *R*, this data modulation will suffer distortion and an equivalent power reduction as it passes through this filter. The equivalent power reduction factor D is computed from

$$D = \int_{-\infty}^{\infty} S_m(f)\,|H(j\,2\pi f)|^2\,df\,, \tag{59}$$

where $S_m(f)$ is the power spectral density of the data modulation and $H(j\,2\pi f)$ is the equivalent lowpass transfer function of the predetection bandpass filter. Thus, the nominal signal power A^2 must be multiplied by D to account for this effect when computing the effective signal-to-noise ratio to be used in the previous detection and false alarm probability computations.

(3) Reduction in Noise Spectral Density Caused by PN Despreading

Multiplication of the equivalent noise process at the PN acquisition system input by the locally generated PN sequence spreads the spectrum of this noise process and simultaneously reduces its effective spectral height into the data filter. Letting N_0' denote this effective noise spectral density, then since the bandwidth of the data (predetection) filter is much narrower than that of the PN process, we have that

$$N_0' \cong N_0 \int_{-\infty}^{\infty} T_c\left(\frac{\sin \pi f T_c}{\pi f T_c}\right)^2 |H(j\,2\pi f)|^2\,df\,. \tag{60}$$

In (60), we have assumed for simplicity of the calculation that the PN line spectrum is approximated by its envelope. Thus, again in computing the effective signal-to-noise ratio of the system, N_0 should be replaced by N_0'.

Finally, summing up the effects of 6.1.4.a(1) - 6.1.4.a(3), the effective signal-to-noise ratio γ' in the predetection filter bandwidth is given by

$$\gamma' = \frac{A^2 D L}{N_0' B}, \tag{61}$$

where D is defined in (59), N_0' in (60) and L, the loss due to a fractional chip misalignment $\Delta' T_c$ from the correlation curve peak, is given by

$$L = \left(1 - \frac{\Delta' T_c}{T_c}\right)^2. \tag{62}$$

Again, for half-chip search updates, the worst case loss corresponds to $\Delta' T_c / T_c = 1/4$.

b. Code Doppler and Its Derivatives

When code doppler and its derivatives characterize the received signal dynamics, then the timing error between received and local PN codes is not constant over the dwell time of the detection process. This "smearing" effect has a direct bearing on the calculation of the loss due to fractional chip timing misalignment and thus the expression for this loss given in (62) requires modification.

Consider first the case where the received signal is characterized by code doppler and doppler rate. Then the normalized signal input to the acquisition dwell time integrator in Figure 29 is (under the signal present hypothesis):

$$\tilde{s}(t) = \left(1 - \frac{\Delta' T_c}{T_c} - \Delta f_c t - \frac{1}{2} \Delta \dot{f}_c t^2\right)^2. \tag{63}$$

The corresponding normalized dwell time integrator output is

$$\begin{aligned} L &= \frac{1}{\tau_D} \int_0^{\tau_D} \tilde{s}(t)\, dt \\ &= \left(1 - \frac{\Delta' T_c}{T_c}\right)^2 - [\Delta f_c \tau_D + \frac{1}{3} \Delta \dot{f}_c \tau_D^2]\left(1 - \frac{\Delta' T_c}{T_c}\right) \\ &\quad + \frac{\Delta f_c^2 \tau_D^2}{3} + \frac{\Delta f_c \Delta \dot{f}_c \tau_D^3}{4} + \frac{\Delta \dot{f}_c^2 \tau_D^4}{20}. \end{aligned} \tag{64}$$

For small Δf_c and $\Delta \dot{f}_c$, the loss L of (57) is well approximated by

$$\tilde{L} = \left[\left(1 - \frac{\Delta' T_c}{T_c}\right) - \frac{\Delta f_c \tau_D + \frac{1}{3}\Delta \dot{f}_c \tau_D^2}{2}\right]^2 . \qquad (65)$$

Finally, if the "signal present cell" is being searched during the finite time interval over which the doppler jerk is present, then (63) becomes

$$\tilde{s}(t) = \left(1 - \frac{\Delta' T_c}{T_c} - \Delta f_c t - \frac{1}{2}\Delta \dot{f}_c t^2 - \frac{1}{6}\Delta \ddot{f}_c t^3\right)^2 \qquad (66)$$

and the corresponding loss as computed from (64) is

$$L = \left(1 - \frac{\Delta' T_c}{T_c}\right)^2 - \left[\Delta f_c \tau_D + \frac{1}{3}\Delta \dot{f}_c \tau_D^2 + \frac{1}{12}\Delta \ddot{f}_c \tau_D^3\right]\left(1 - \frac{\Delta' T_c}{T_c}\right)$$

$$+ \frac{1}{j+k+1}\sum_{j=1}^{3}\sum_{k=1}^{3}\left(\frac{1}{j!}\right)\left(\frac{1}{k!}\right)\Delta f_c^{(j)}\,\Delta f_c^{(k)}\,\tau_D^{j+k} , \qquad (67)$$

where, for simplicity of notation, we have defined

$$\Delta f_c^{(1)} = \Delta f_c$$

$$\Delta f_c^{(2)} = \Delta \dot{f}_c$$

$$\Delta f_c^{(3)} = \Delta \ddot{f}_c . \qquad (68)$$

Again for small Δf_c, $\Delta \dot{f}_c$, and $\Delta \ddot{f}_c$, (67) is well approximated by

$$\tilde{L} = \left[\left(1 - \frac{\Delta' T_c}{T_c}\right) - \frac{\Delta f_c \tau_D + \frac{1}{3}\Delta \dot{f}_c \tau_D^2 + \frac{1}{12}\Delta \ddot{f}_c \tau_D^3}{2}\right]^2 . \qquad (69)$$

Using (67) or (69) in (61), one is able to compute, to a first order approximation, the effective signal-to-noise ratio in the predetection filter bandwidth when the received signal dynamics are characterized by code doppler and its first two derivatives.

Because of the dependence of L on dwell time τ_D, the procedure for ultimately calculating mean acquisition time is more complex but may be summarized as follows:

(a) For a given detection probability (P_D'), solve for P_D from (58).

(b) For a specified bandwidth B and filter type, compute D from (58) and N_0' from (60). (Actually, carrier and code doppler affect these computations but we shall assume these are second-order effects.)

(c) Using D and N_0' computed in (b) and L from (67) or $\tilde{L}$ from (69), determine γ' from (61) as a function of τ_D (assume A^2/N_0 is given and worst case misalignment).

(d) Letting $N_B = B\tau_D$, then for a given P_{FA}, together with P_D determined from (a) and γ' from (c), solve (transcendentally) for τ_D from (56).

(e) Using τ_D as determined in (d), and the given values of P_D' and P_{FA}, calculate $\bar{T}$ from (20).

6.2 Sequential Detection Acquistion Time Performance of the Shuttle GPS Receiver

6.2.1 Introduction

Sequential detection is a detection process first used in radar and, more recently, applied to the acquisition process in PN receivers. It offers the advantage of significantly faster search times when compared to "fixed step size" search procedures. The advantage is achieved because the sequential process is able to decide that signal (i.e., PN correlation or partial correlation) is absent much faster than the fixed integration time process. This is because the latter process spends as much time deciding there is no signal (which is the predominant test in an acquisition search) as it does in deciding that the signal is present. Thus, most GPS receivers are implemented with a sequential detection acquisition search algorithm. The following performance analysis of sequential detection acquisition is presented for the purpose of optimizing the Shuttle GPS receiver acquisition algorithm parameters. This results in the minimum Shuttle GPS receiver acquisition time and, consequently, minimum time to first fix (TTFF).

6.2.2 Description of Sequential Detector

The sequential synchronization detector used for GPS receivers is shown in Figure 30. The mean output of this system is proportional to the total power contained in the input. The actual output X(t) is compared to a threshold θ' that is chosen to maximize the probability of detection, P_D, for a given probability of false alarm, P_{FA}. This will lead to minimization of the average synchronization time.

The integration of the square-law output before making a threshold comparison increases the probability of detection, P_D, without changing the probability of false alarm, P_{FA}. The bias subtraction before the integration process will cause the post-detection integration (PDI) output to increase when signal-plus-noise is present and decrease when noise alone is present. The threshold θ' is set to a negative value at the PDI output. If the output is above the threshold for all $0 \leq t \leq T_{TR}$, where T_{TR} denotes the truncation time, the signal is declared present; otherwise, the output will go below the threshold, causing a dismissal of noise alone in a time much smaller than T_{TR}, as shown in Figure 31.

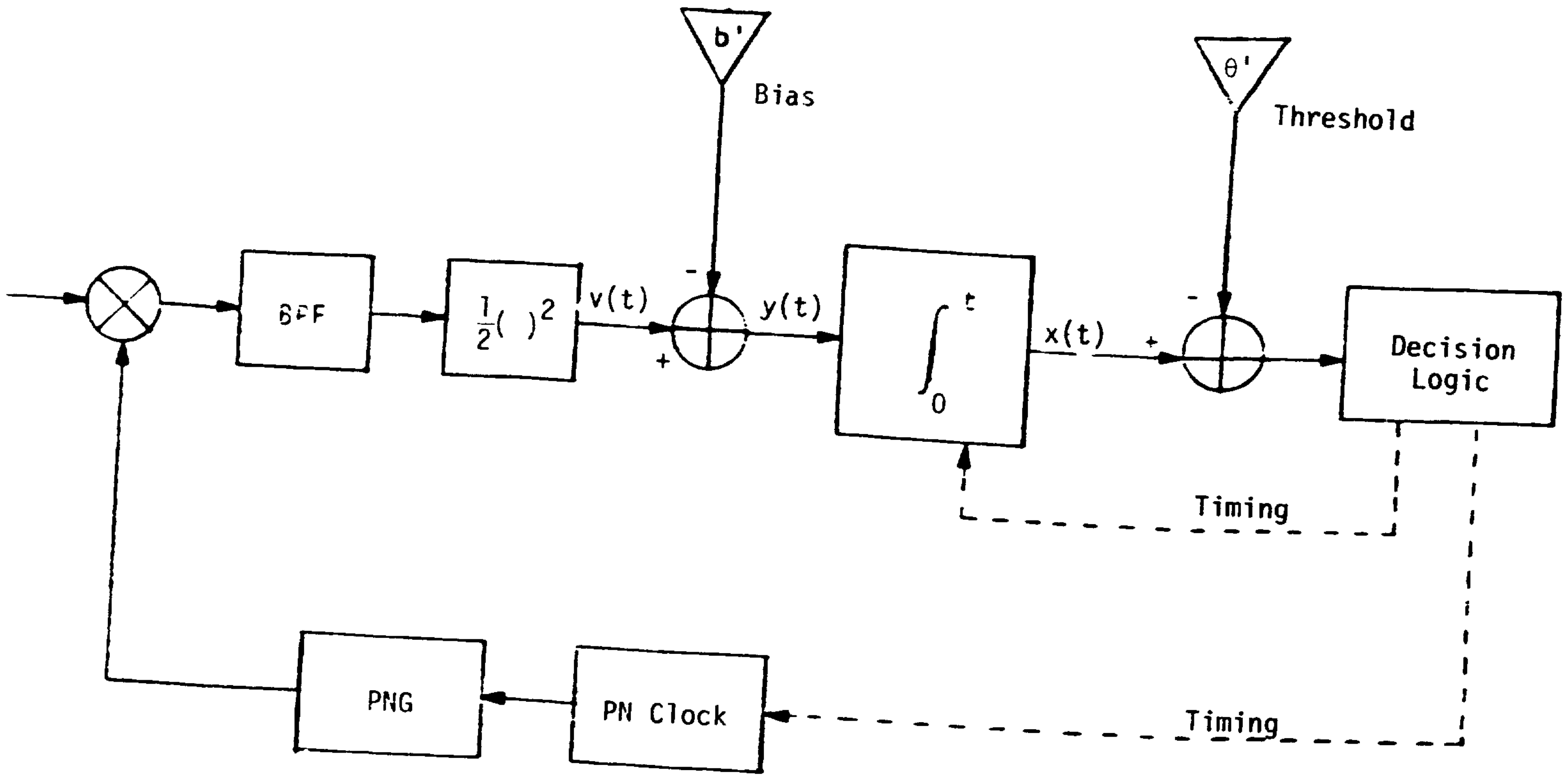

Figure 30. Block Diagram of a Sequential Detection Acquisition System

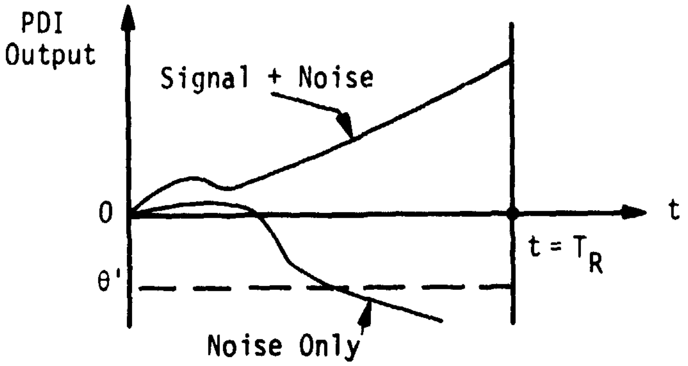

Figure 31. PDI Output as a Function of Time, t

6.2.3 Signal Description

The received GPS signal r(t) is of the form

$$r(t) = \sqrt{2P_p}\, d(t)\, P_p(t) \sin(\omega t + \phi) + \sqrt{2P_{C/A}}\, d(t)\, P_{C/A}(t) \cos(\omega t + \phi) + n(t) \tag{70}$$

where

$P_p(t)$ = high-precision ranging PN code of rate 10.23 Mc/s

$P_{C/A}(t)$ = Gold code of length 1023 chips and rate 1.023 Mc/s

$d(t)$ = 50 sps data signal

ω = carrier frequency

ϕ = unknown carrier phase

P_p = received power with $P_p/N_0 = 31.6$ dB-Hz

$P_{C/A}$ = received power with $P_{C/A}/N_0 = 34.6$ dB-Hz

$n(t)$ = additive thermal noise assumed to be Gaussian with flat spectral density $kN_0/2$.

There is also a code doppler of ±5 chips/sec.

6.2.4 Detector Description

As shown in Figure 30, the receiver multiplies r(t) by a replica of p(t), which starts at some arbitrary initial code phase. The resulting product is passed through a filter wide enough to pass the data signal d(t) plus the doppler shift with little distortion. A filter bandwidth, B, of four times the data rate is enough. For a 50 bps data signal, a bandwidth of 200 Hz is chosen, although the effect of changing bandwidth on the results is discussed later in this report. If the initial phase of the code p(t) is very close to that of the received code, the filter output Z(t) will be the data modulated carrier plus noise; otherwise, the product will be noise alone.

The noise, n(t), in (70) can be divided into its two orthogonal components, yielding:

$$n(t) = \sqrt{2}\, n_I(t) \cos(\omega t + \phi) + \sqrt{2}\, n_Q(t) \sin(\omega t + \phi) ,$$

where n_I and n_Q are two independent, zero mean, Gaussian noise processes with spectral density $N_0(\text{in}) = 1.18\ N_0$ when in correlation and $N_0(\text{out}) = 1.4\ N_0$ when not in correlation.

Assume the square-law output takes the form $v(t) = 1/2\ Z^2(t)$. Then, the outputs under the two hypotheses are:

$$v(t) = \frac{1}{2}\left[n^2_{I[out]}(t) + n^2_{Q[out]}(t)\right] \qquad \text{under } H_0 ;$$

$$v(t) = \frac{1}{2}\left[\sqrt{2p}\ d(t) + n^2_{I[in]}(t)\right]^2 + n^2_{Q[in]}(t) \qquad \text{under } H_1 .$$

Let v(t) be sampled at $t = 1/B$; then the resulting random variable (v') will have the densities

$$P(v'|\text{in}) = e^{-(\alpha+v')}\, I_0(2\sqrt{\alpha v'}) ; \qquad v' > 0 \qquad \text{under } H_1$$

$$P(v'|\text{out}) = \frac{1}{R}\, e^{-v'/R} ; \qquad v' > 0 \qquad \text{under } H_0 ,$$

where

$$v' = \frac{v}{N_0(\text{in})\, B} .$$

v' can be generated using the computer [4] as follows:

$$v' = \frac{(g_1 + \sqrt{2\alpha})^2 + g_2^2}{2} , \text{ for the in condition ;}$$

$$v' = \frac{R(g_1^2 + g_2^2)}{2}, \qquad \text{for the out condition;}$$

$$R = \frac{N_0(\text{out})}{N_0(\text{in})}.$$

g_1 and g_2 are independent, zero mean, unit variance random numbers and α is the signal-to-noise ratio in the filter bandwidth B.

For the sequential detector to be effective, the bias (b) must take a value in between the means of the square-law output under the two hypotheses, i.e.,

$$E(X|\text{out}) < b < E(X|\text{in}), \tag{71}$$

where E[X] is the mean of the signal after bias subtraction and is given by [4]:

$$E[X|\text{out}] = (1 - b')\, N_0(\text{out})\, B$$

$$E[X|\text{in}] = (1 + \alpha)\, N_0(\text{in})\, B - b' N_0(\text{out})\, B.$$

Substituting in (71) yields:

$$1 < b' < (1 + \alpha) \frac{N_0(\text{in})}{N_0(\text{out})}.$$

As a better value for simulation, take

$$b = b' \frac{N_0(\text{out})}{N_0(\text{in})};$$

then,

$$\frac{N_0(\text{out})}{N_0(\text{in})} < b < 1 + \alpha$$

or $\quad 1.19 < b < 1 + \alpha.$

Although the optimum bias b can be theoretically bounded by the above values, the values of threshold θ and truncation time T_{TR} cannot. However, adequate values for θ and T_{TR} can be chosen based on simulation results such that the average synchronization time T_s reaches a minimum value under a desired P_D, P_{FA}, and signal-to-noise ratio α. Evaluation of probability of detection P_D and average time to dismiss the noise alone T_D are needed to obtain complete information about the average synchronization time T_s. This can be illustrated as follows, using the C/A code. Assume the length of the code 1023 chips and the search process proceeds in half-chip increments; then the number of cells to be searched (the uncertainty region) will be 2×1023 cells. The synchronizer takes an average of $2 \times 1023 \times T_D$ seconds to search through the whole uncertainty region. Since P_D is small for small SNR, it will take, on the average, $1/P_D$ passes through this region before the correct synchronization point is reached. Thus, the average synchronization time is given by

$$T_{S1} = \frac{2 \times 1023}{P_D} T_D . \tag{72}$$

The values of T_D and P_D are calculated from computer simulations using the Monte Carlo method as follows. Let XN denote the total time taken to dismiss up to the truncation time T_{TR} for a number of trials equal to XTEST, assuming the noise signal alone is present. Let Xj denote the number of trials that were not dismissed (the number of trials where the PDI output is above threshold for all the time $0 \leq t \leq 1$) under noise signal alone. Let Xj1 denote the number of trials that were not dismissed under signal + noise conditions. Then,

$$T_D = (XN)/(XTEST - Xj)$$

$$P_D = (Xj1)/(XTEST)$$

$$P_{FA} = (Xj)/(XTEST) .$$

It is important to note that there is an average synchronization time correction $(T_{S2} + T_{S3})$ that has to be added to the average synchronization time T_{S1} given in (72). T_{S2} is due to false alarm causing the test to proceed to truncation time and is given by

$$T_{S2} = 2 \times 1023 \times T_{TR} \text{ sec} \times P_{FA} \text{ sec} .$$

T_{S3} is due to time (equal to $T_{penalty}$) spent in the phase-lock loop to determine the false condition. Thus, T_{S3} is given by

$$T_{S3} = 2 \times 1023 \times T_{penalty} \times P_{FA} ,$$

where $T_{penalty}$ is 1 sec, which is the typical code loop response time, so the total average synchronization time would be $T_{S_{total}} = T_{S1} + T_{S2} + T_{S3}$.

6.2.5 Simulation Results and Parameter Optimization

A computer simulation of the sequential detector is used here, since the sequential detection process is not amenable to analysis. A flow diagram for the basic computer simulation program is shown in Figure 32. The subloops for optimizing the values of threshold θ and bias b are not shown, for purposes of clarity. For different values of threshold θ, the bias b is changed within the permissible range so that a best value for b and θ can be selected for fixed values of normalized truncation time ITRNK of 20 and number of trials of 1000. The relation between average synchronization time with b and θ is shown in Figure 33 in the range where probability of detection (assuming single-signal level) is not less than 0.6 and P_{FA} not greater than 0.005. The optimum values for b and θ are chosen from curves to be $b = 2.4$ and $\theta = -1.2$. Then a trial is made to get the relation between truncation time ITRNK and average synchronization time T_{S1}. Two values of ITRNK are chosen to be 16 and 10 where, as shown in Figure 34, ITRNK of 10 gives a smaller T_{S1} but a bigger P_{FA} than that of 16. Figures 35 and 36 show the relation between SNR(α) in dB versus T_{S1} for the ITRNK of 10 and 16, respectively. As SNR in the receiver drops, the acquisition time increases because the receiver has to make several passes through the full period until synchronization is detected.

6.2.6 Correlation Peak Detection

A trial using the actual signal which, in the ideal case, takes the triangle shape shown in Figure 37 instead of using single-point signal + loss was investigated. As expected, the P_D increases (e.g., for the previous specific values of $b = 2.4$, $\theta = -1.2$, ITRNK = 10, the signal point $P_D = 0.686$ while, for the correlation signal case, $P_D = 0.936$). Table 19 shows in detail the actual Monte Carlo random starting positions and the associated probabilities. The initial condition is chosen at random and the trial is repeated five times ($L = 5$) with the resultant probability of detection

$$P_D = \frac{1}{L} \sum_{i=1}^{L} P_i = 0.9842 .$$

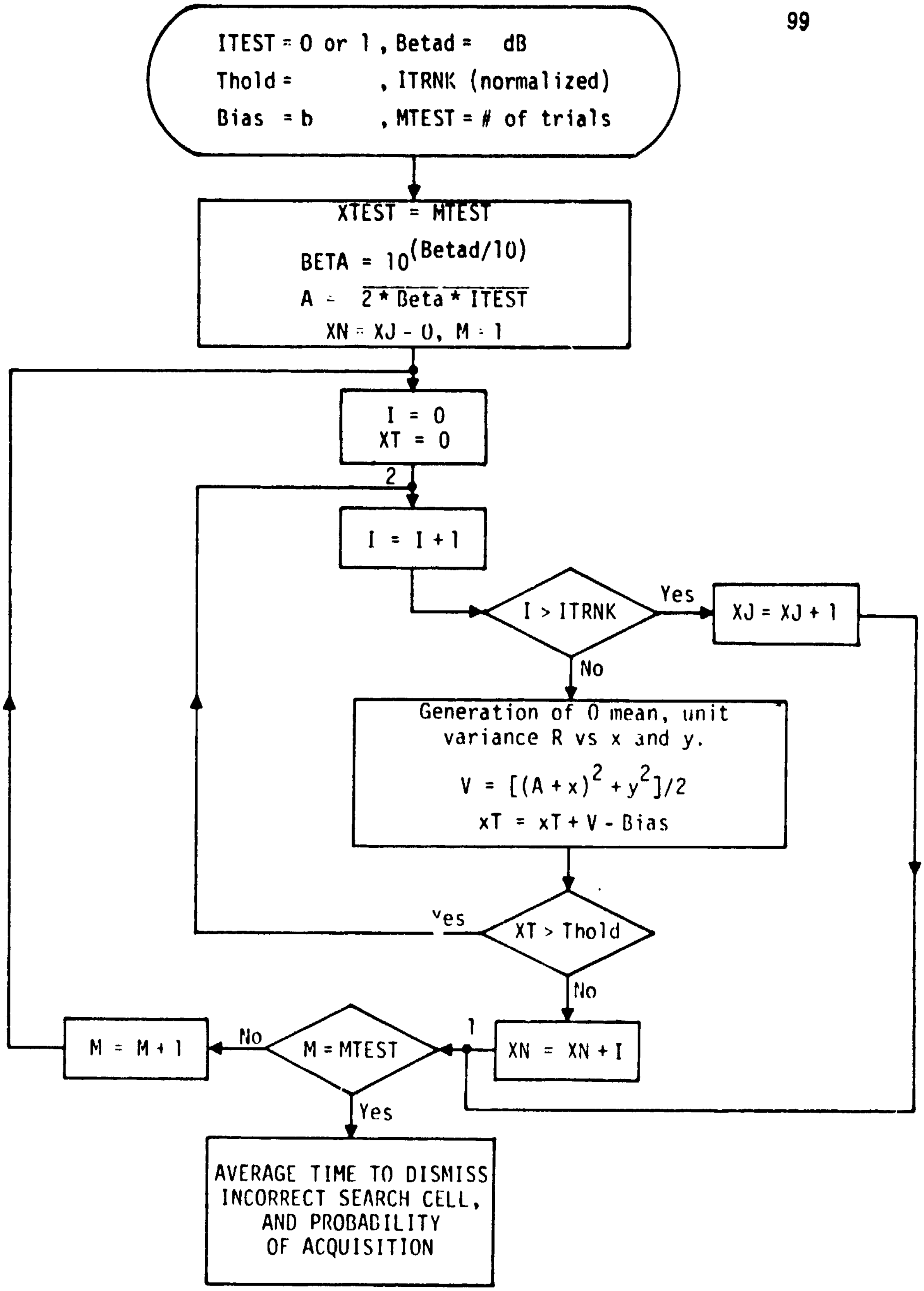

Figure 32. Sequential Detection Simulation Flow Chart

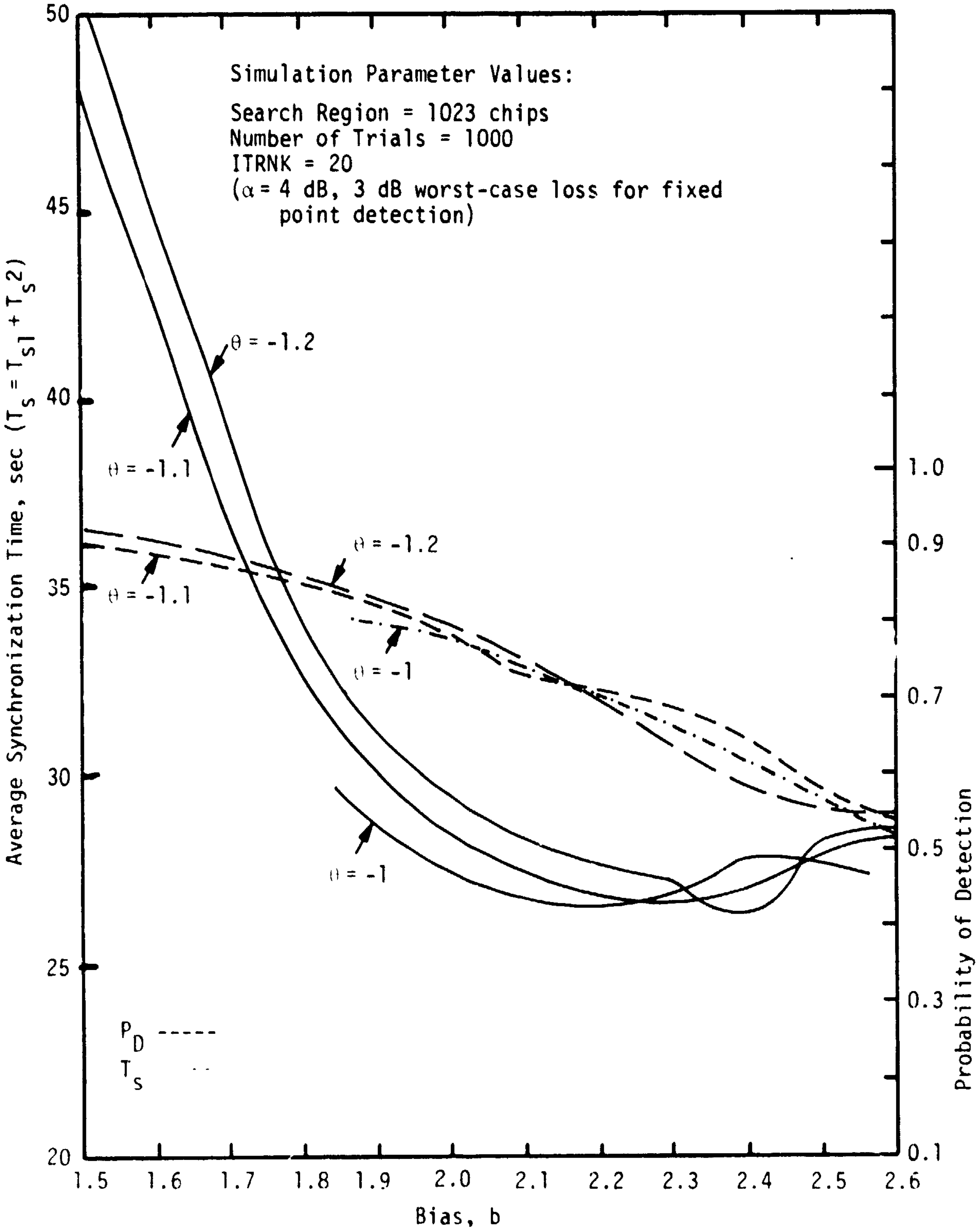

Figure 33. Variation of Average Synchronization Time and Detection Probability With Bias b and Threshold θ for Picking b and θ

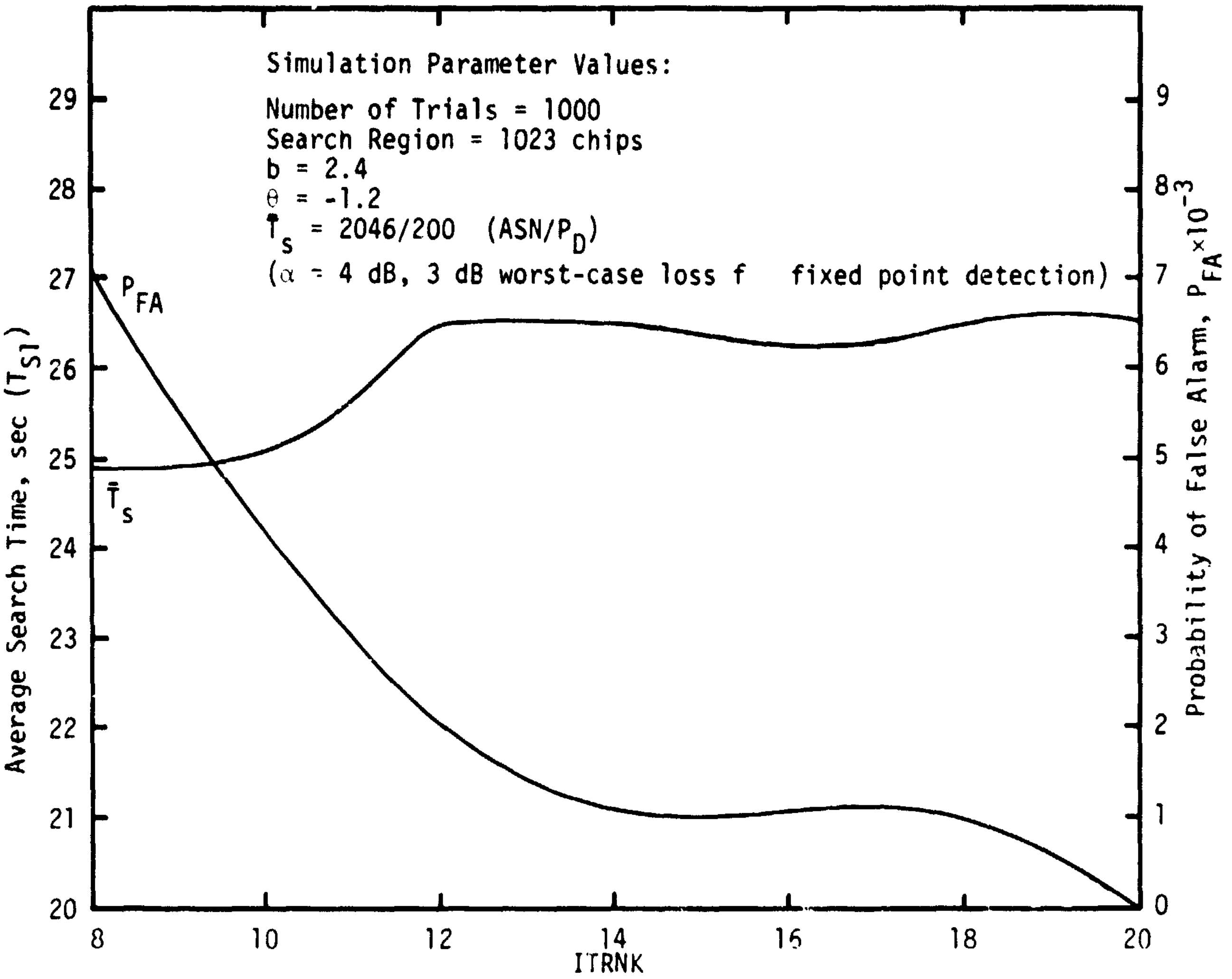

Figure 34. Variation of Average Synchronization Time and Probability of False Alarm With Truncation Time (Normalized)

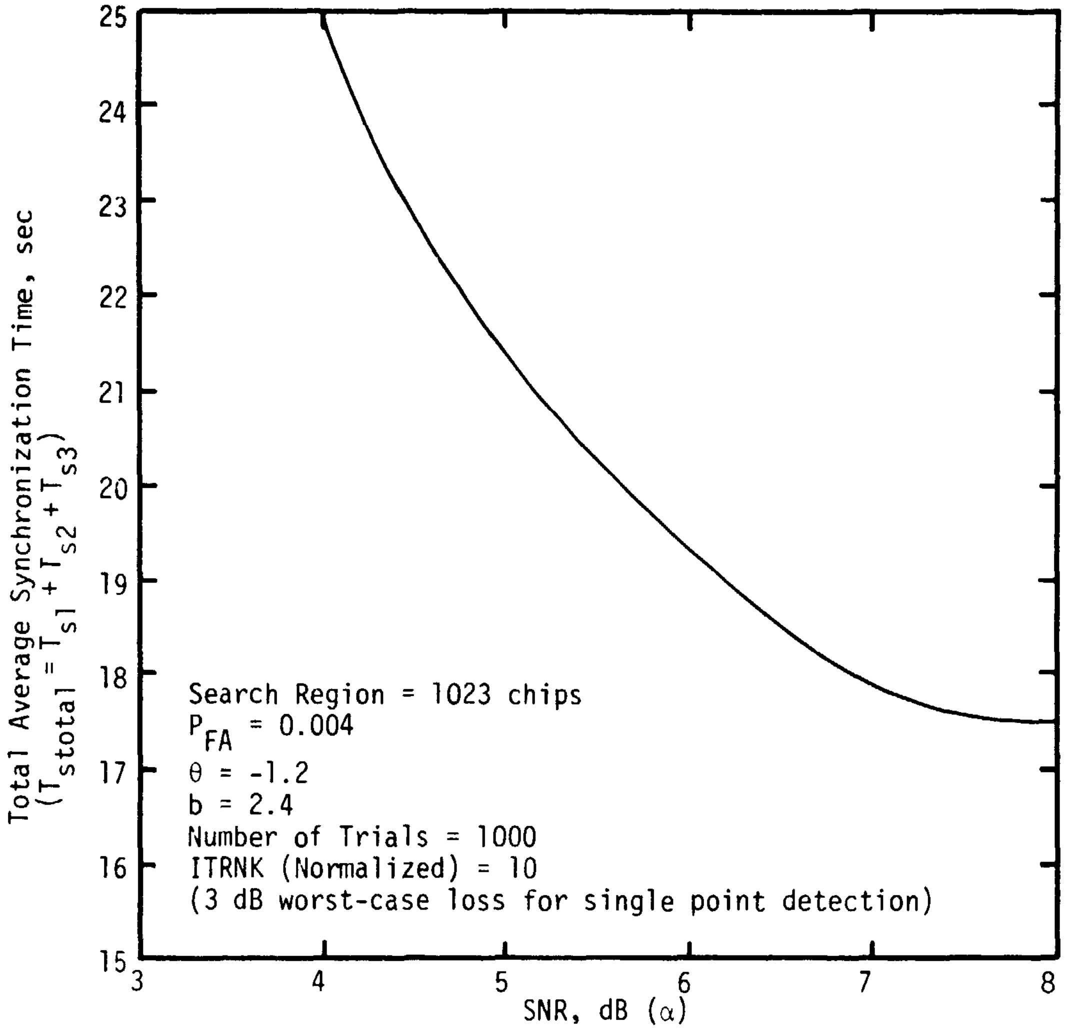

Figure 35. C/A Code Acquisition Time as a Function of Signal-to-Noise Ratio (ITRNK = 10)

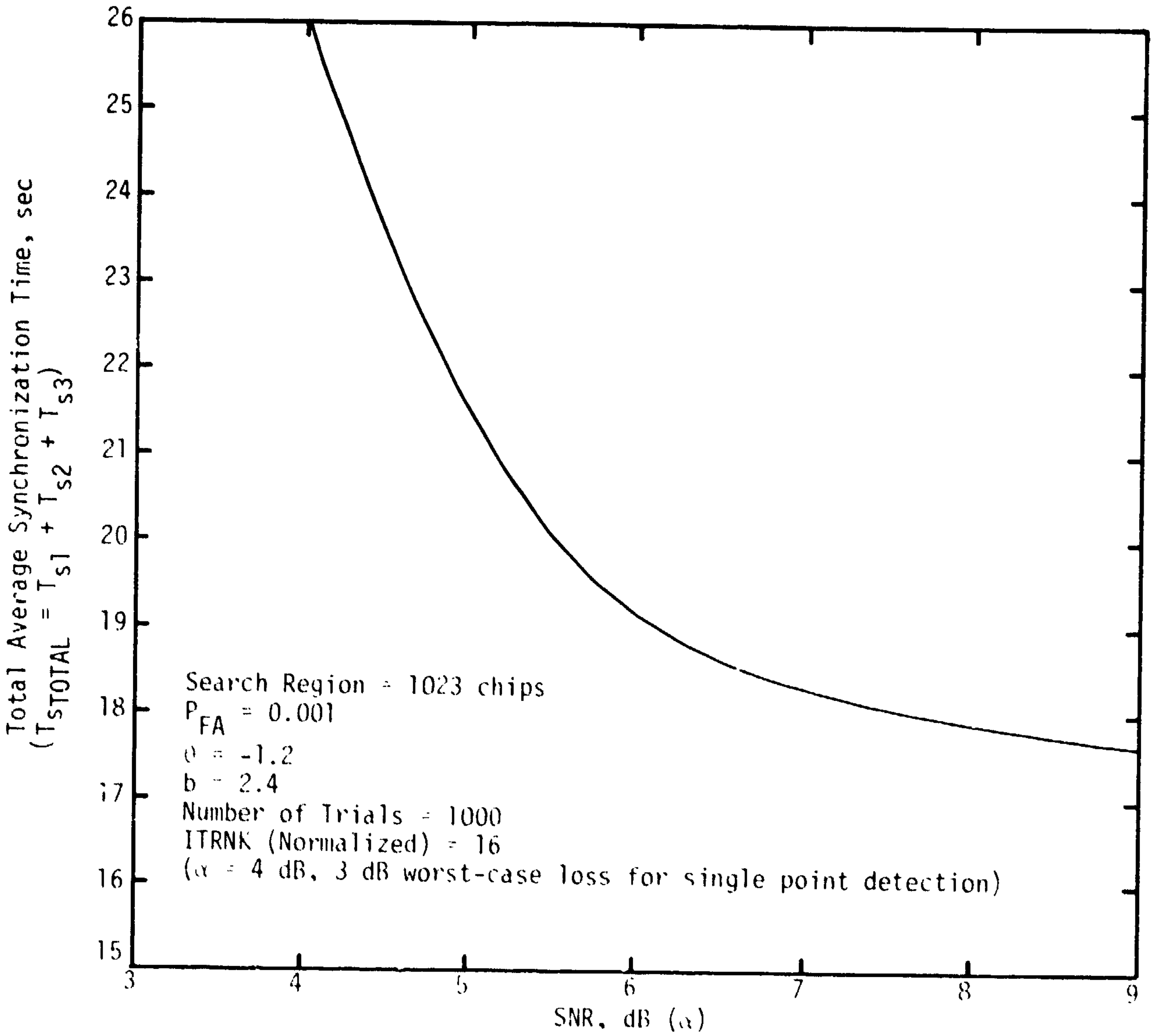

Figure 36. C/A Code Acquisition Time as a Function of Signal-to-Noise Ratio (ITRNK = 16)

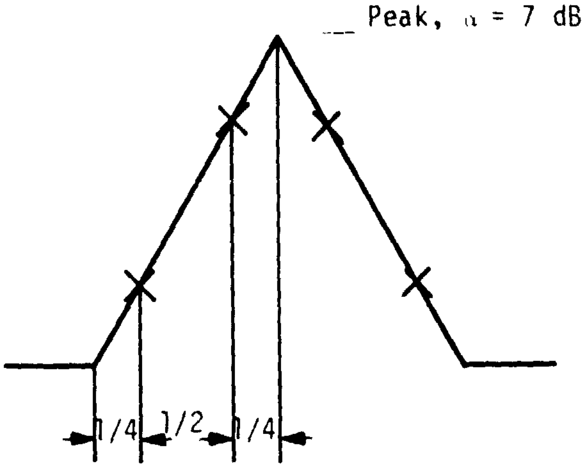

a. Fixed Detection Points

b. Variable Detection Points

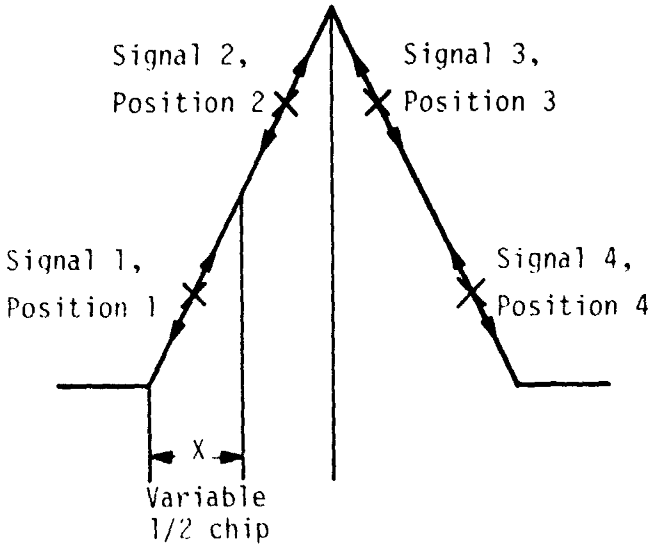

NOTE: Position 1 (and hence Signal 1) varies between 0 and 1/2 chip randomly. Positions 2, 3, 4 (and hence Signals 2, 3, 4) follow Position 1 proportionately with constant displacement.

Figure 37. Two Models of Correlation Peak Detection Used in Simulation

Table 19. Random Starting Points for Correlation Detection for Monte Carlo Simulation and Resultant Probability of Detection

Number of divisions between 0 and 1/2 chip (N)	6
Number of trials (L)	5
	P_D
P(1), which corresponds to random position of s(1) at 1	0.952
P(2), which corresponds to random position of s(1) at 2	0.933
P(3), which corresponds to random position of s(1) at 3	0.928
P(4), which corresponds to random position of s(1) at 1	0.950
P(5), which corresponds to random position of s(1) at 6	0.978
Average $P_d = \frac{1}{L} \sum_{i=1}^{L} P_i$	0.948

In Table 20, the initial condition is picked so that all the possible initial values are chosen equally and the average value of P_D is calculated, resulting in P_D of 0.9442. The above two cases are compared to the case of using four fixed signal positions, shown in Figure 37a, which has a probability of detection of $P_D = 0.936$. Thus, it is concluded that a decision to use a fixed-signal position is preferred for simulation purposes since the difference between this case and the actual random case is not significant.

Using the data for the fixed four-signal case, the average synchronization time, $T_{S1} + T_{S2}$, and P_D are plotted versus SNR, as shown in Figure 38, where both synchronization time and P_D are improved over those of Figure 35, which corresponds to the single-point case. From Figure 38, $P_D = 0.983$ at SNR = 31.6 dB-Hz.

Since $P_D = 0.9$ is a reasonable enough value at SNR = 31.6 dB-Hz, a refinement of the results is done by picking different values of b and θ so that P_D is within 0.9. The values of $b = 3$ and $\theta = -0.9$ are chosen as optimum values from Figure 39. The corresponding values of probability of detection and probability of false alarm are $P_D = 0.9$ and $P_{FA} = 0.001$, respectively. The corresponding values for $T_{S_{total}}$ as a function of SNR is shown in Figure 40. As expected, it is improved by approximately 10% at $\alpha = 8$ dB.

The same reasoning is followed at SNR = 34.6 Hz, which corresponds to the C/A code, and the optimum values are taken from Figure 41 to be $\theta = -0.07$ and $b = 4.2$. The corresponding values for $T_{S_{total}}$ and P_D versus SNR are shown in Figure 42.

6.2.7 Doppler Effect

The effect of the code doppler on the signal-to-noise ratio α is taken into account in this section. It was shown [4] that the signal-to-noise ratio will be changed for each new sample to take the form:

$$\alpha(t) = \alpha_0\left(1 - \frac{\Delta P\ t}{1 - P_0}\right)^2 ,$$

where α_0 is the SNR at $t = 0$ (this corresponds to SNR at the peak of the triangle); P_0 is the initial phase error it will take for the four fixed-signal case, 0.75 chips for S(1) or S(4) and 0.25 chips for S(2) or S(3);

Table 20. Equally Weighted Starting Points for Correlation Detection with Resulting Probability

Number of divisions between 0 and 1/2 chip (N)	6
Number of trials (L)	5
	P_D
P(1), which corresponds to random position of s(1) at 1	0.944
P(2), which corresponds to random position of s(1) at 2	0.926
P(3), which corresponds to random position of s(1) at 3	0.927
P(4), which corresponds to random position of s(1) at 4	0.959
P(5), which corresponds to random position of s(1) at 5	0.965
Average $P_d = \frac{1}{L} \sum_{i=1}^{L} P_i$	0.9442

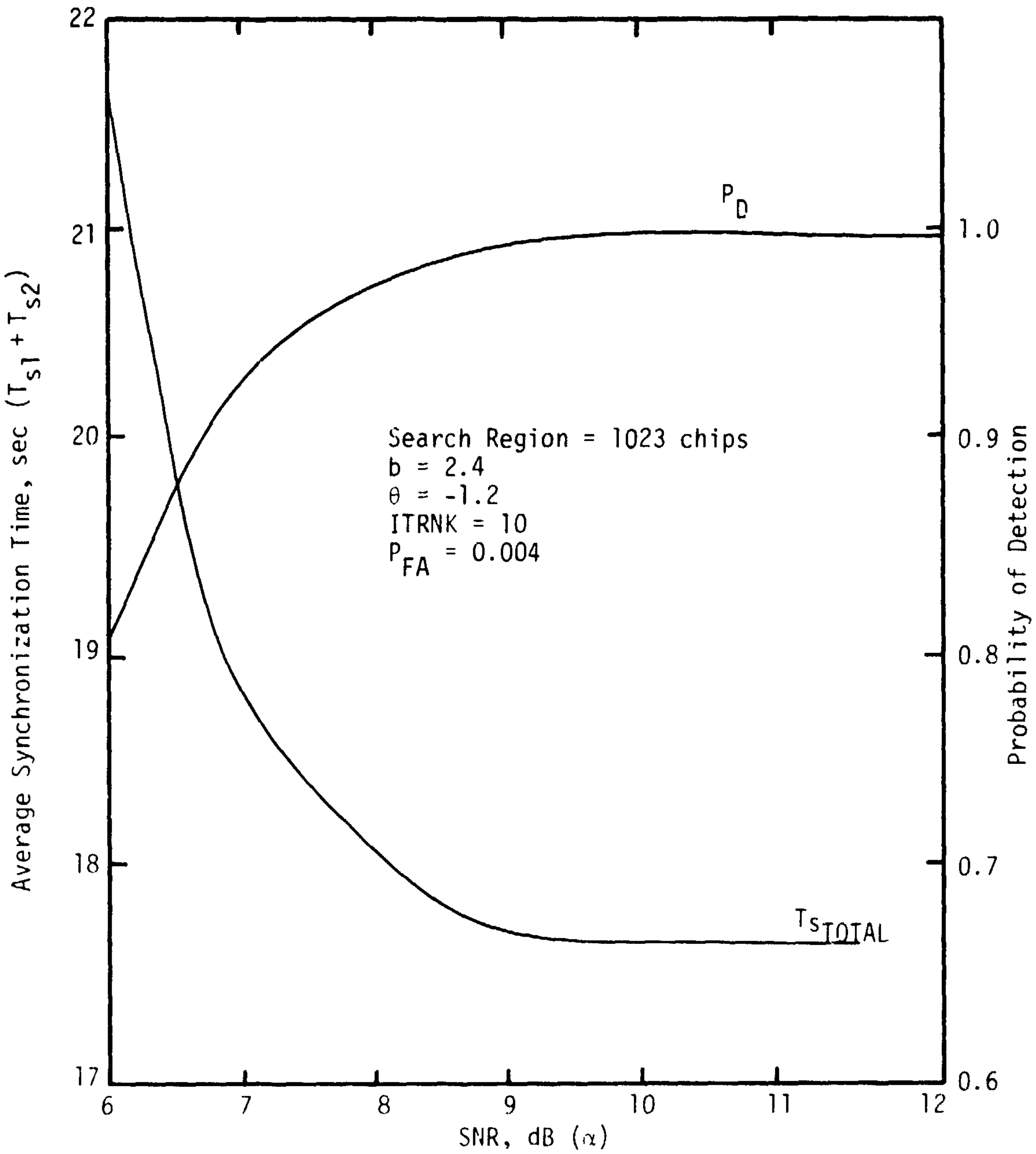

Figure 38. Variation of Detection Probability and Synchronization Time With Signal-to-Noise Ratio for Four Possible Correlation Detection Points

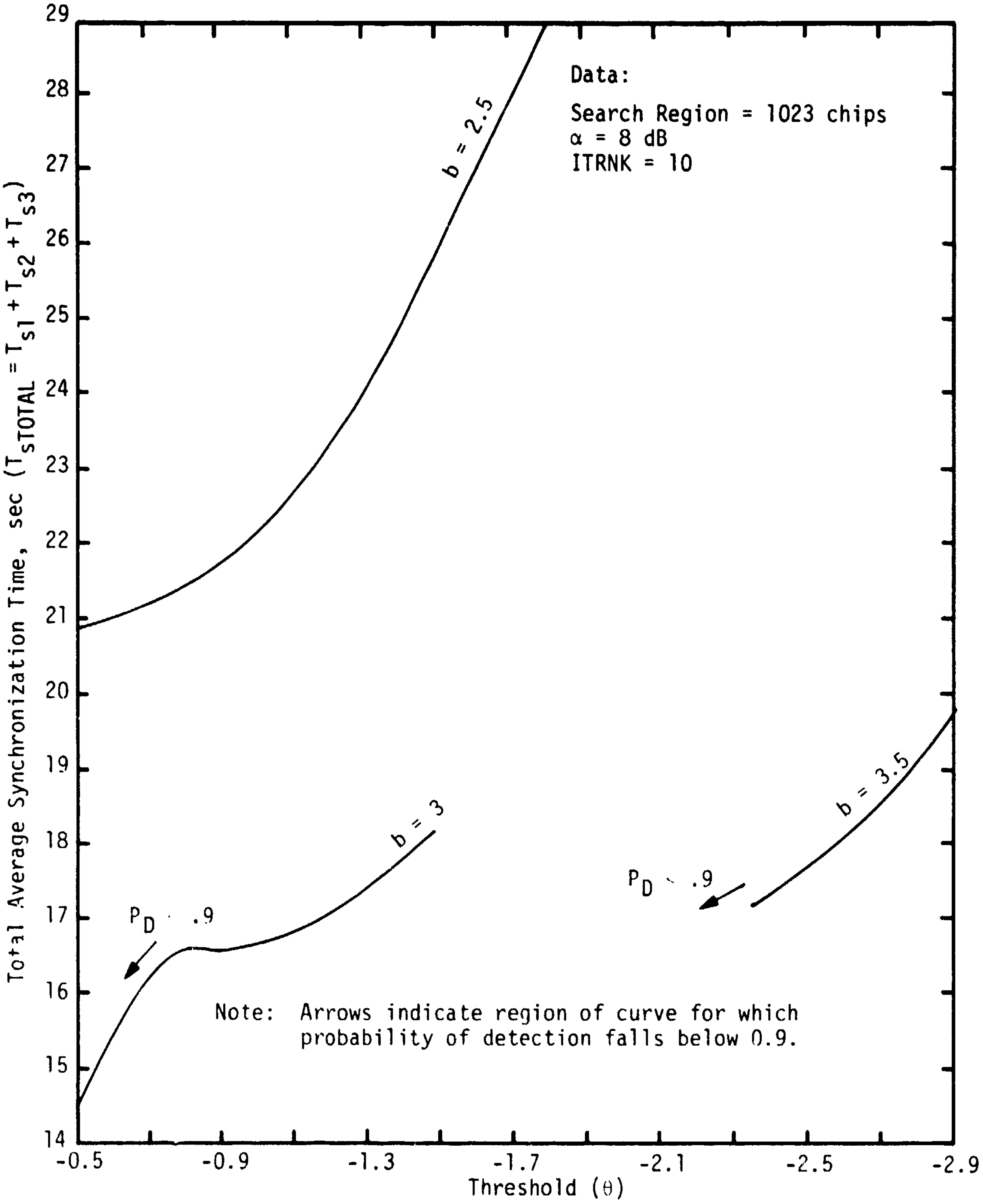

Figure 39. Variation of Synchronization Time With Bias b and Threshold θ for Picking b and θ With Multiple Point Correlation Detection

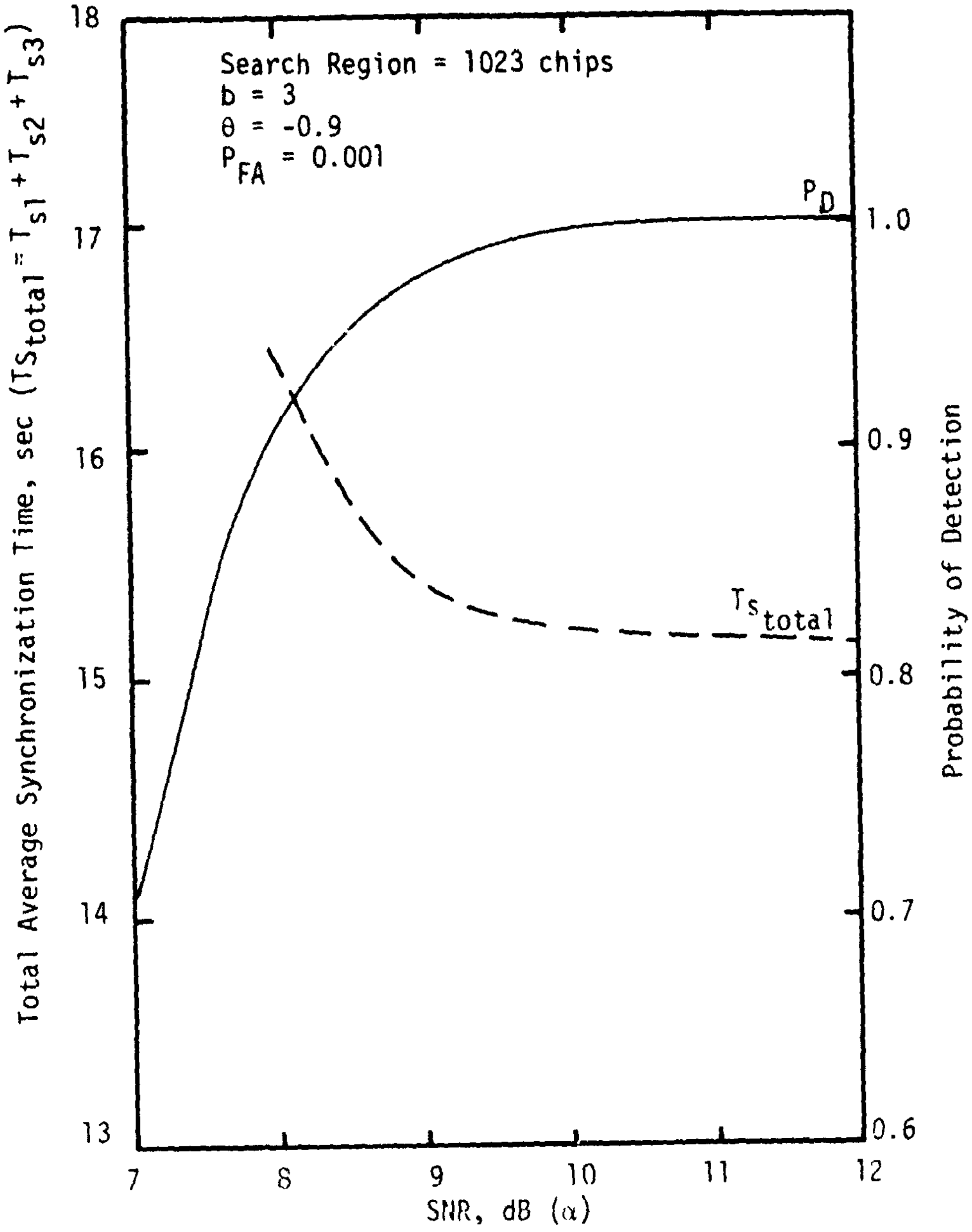

Figure 40. Variation of P_D and $T_{s_{total}}$ With α for b and θ Optimized at $\alpha = 8$ dB for Four-Point Correlation Detection

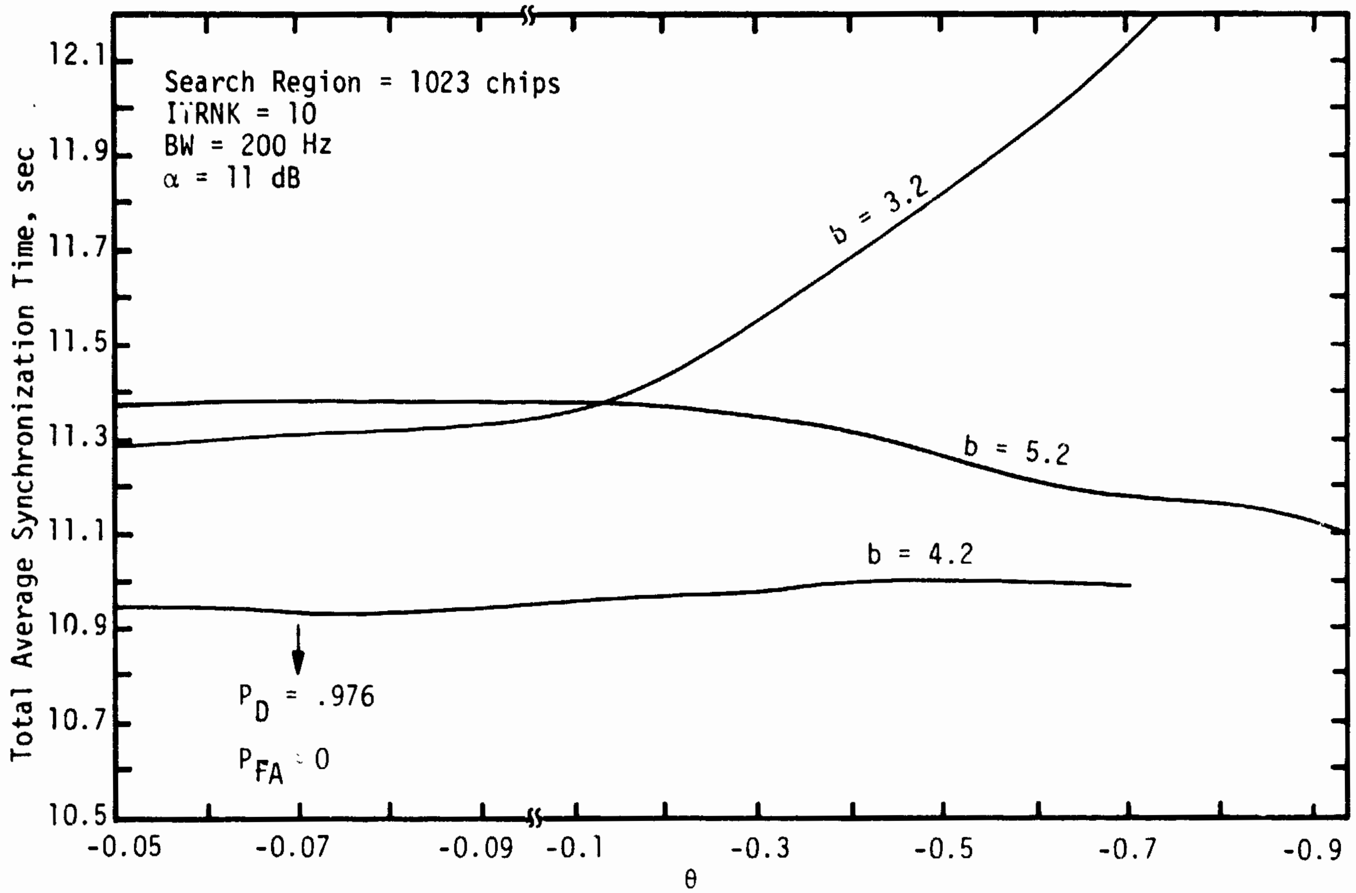

Figure 41. Variation of Total Average Synchronization Time with θ and b for $\alpha = 11$ dB ($C/N_0 = 34$ dB) at Correlation Peak for Four-Point Correlation Detection

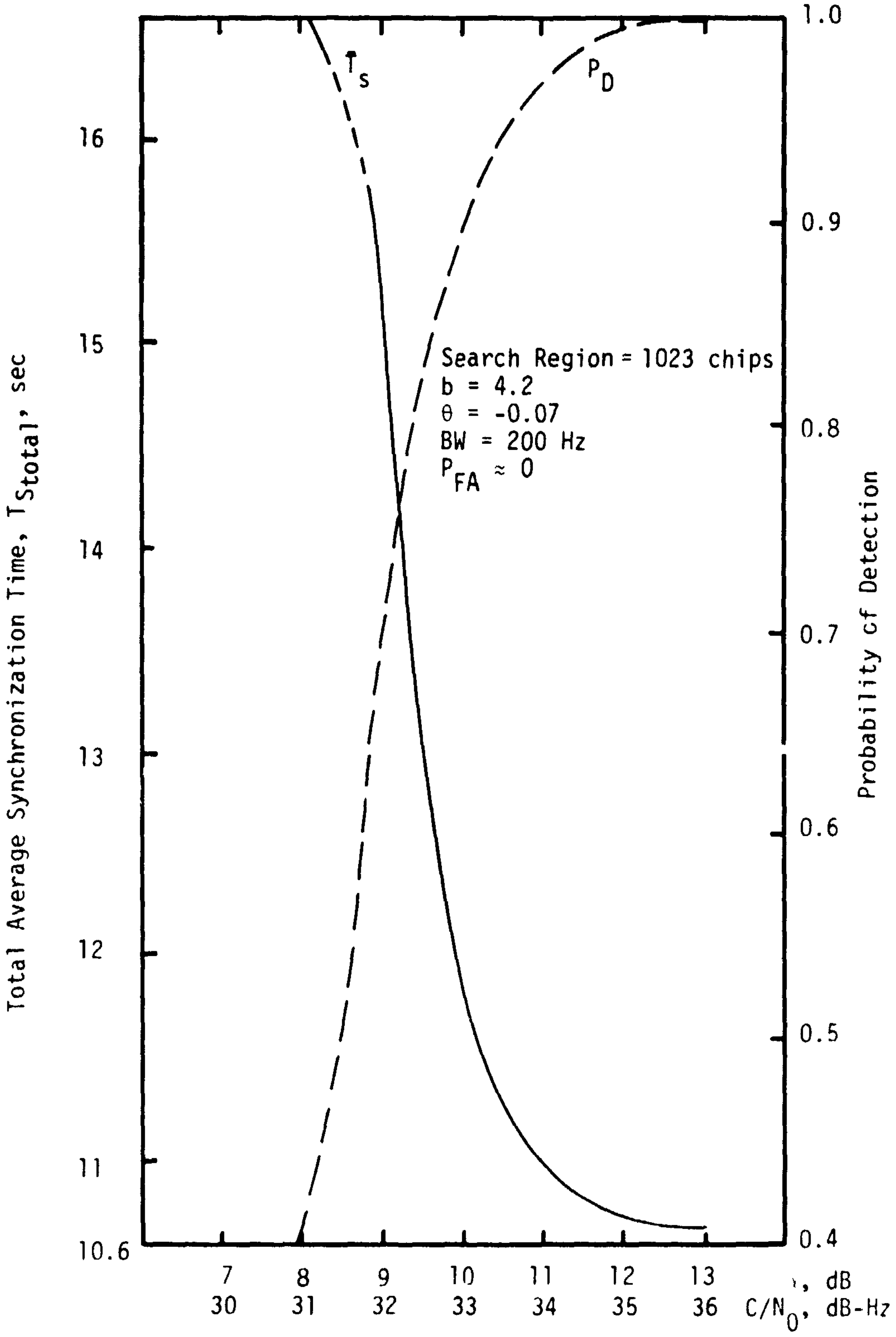

Figure 42. Variation of Total Average Synchronization Time With α (Also C/N$_0$) for b and θ Optimized for α = 11 dB

and ΔP is the code doppler, which is assumed in our case to be ±5 chips/sec. The effect of the code doppler on the total average synchronization time $T_{S_{total}}$ and P_D is considered for the four fixed-signal level.

The relation between doppler and $T_{S_{total}}$ and degradation is plotted in Figures 43 and 44 for the previously selected values of b and θ at the two levels $\alpha = 8$ dB and $\alpha = 11$ dB, respectively. It can be seen that, for doppler offsets greater than approximately 5 chips/sec, the performance degrades rapidly.

6.2.8 Predetection Bandwidth Effect

The simulation bandwidth was varied among the three values 100 Hz, 200 Hz, and 400 Hz to determine the performance sensitivity to bandwidth. The relation between SNR (dB-Hz) versus $T_{S_{total}}$ was considered for the three cases using the best operating points at (peak of triangle) $\alpha = 8$ dB and $\alpha = 11$ dB, respectively. The six curves are drawn in Figure 45 with the LinCom result, which corresponds to a bandwidth of 500 Hz. It is noted from the curves that the Axiomatix results give somewhat better $T_{S_{total}}$ than those of LinCom for the C/A code.

6.2.9 Conclusions

As a result of the analyses and simulations conducted by Axiomatix, it has been shown that a Shuttle GPS receiver with sequential search can search and acquire the entire C/A code in approximately 10 seconds. Furthermore, 1000 chips of P code uncertainty can be searched, with high probability of detection, in approximately 16 seconds. An unfavorable doppler offset of up to 5 code chips per second has negligible effect on the acquisition time. This corresponds to a LOS range rate uncertainty of 5000 feet per second for C/A code acquisition and 500 feet per second for P code acquisition.

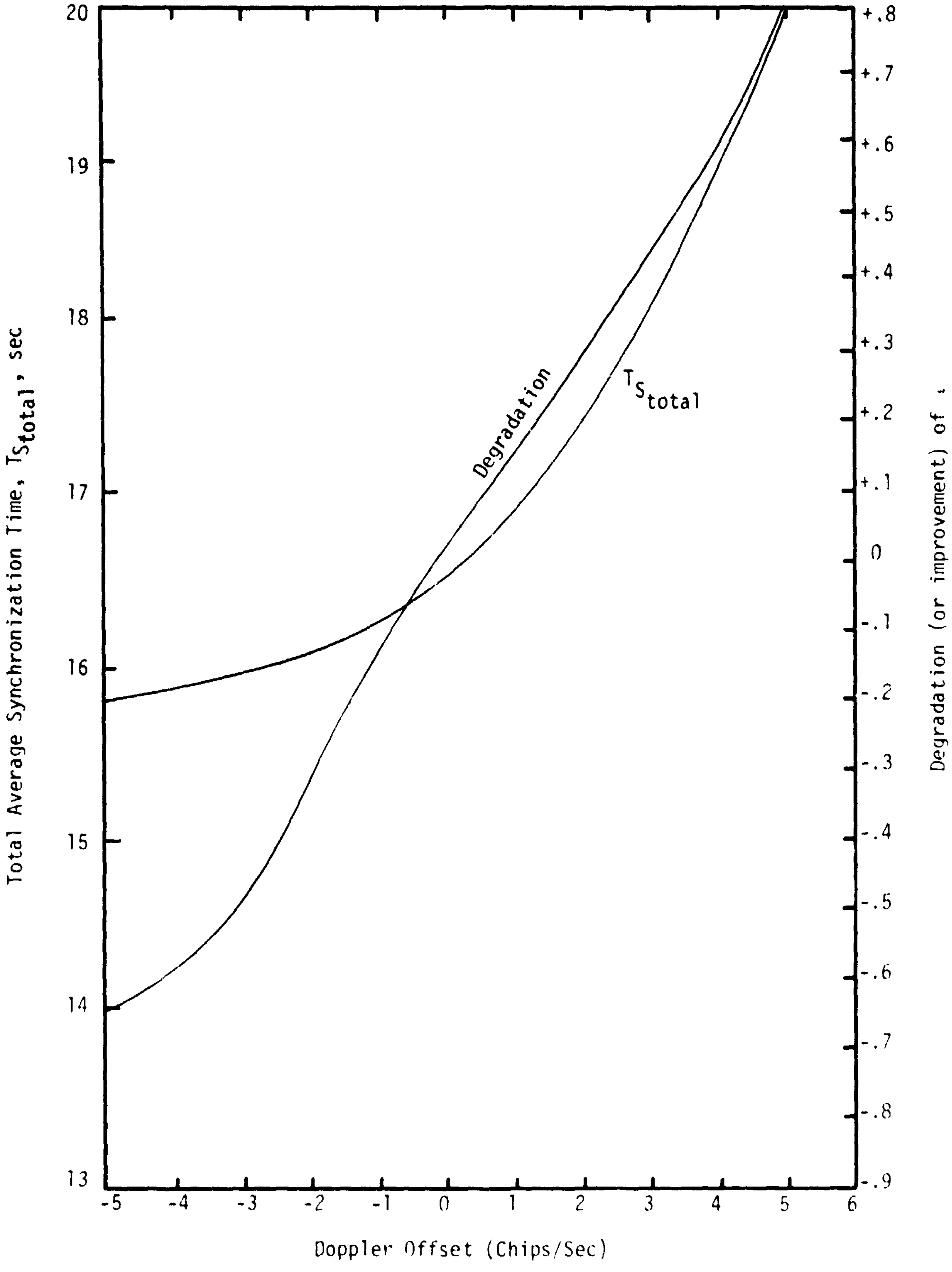

Figure 43. Variation of Total Synchronization Time and Degradation With Code Doppler Offset

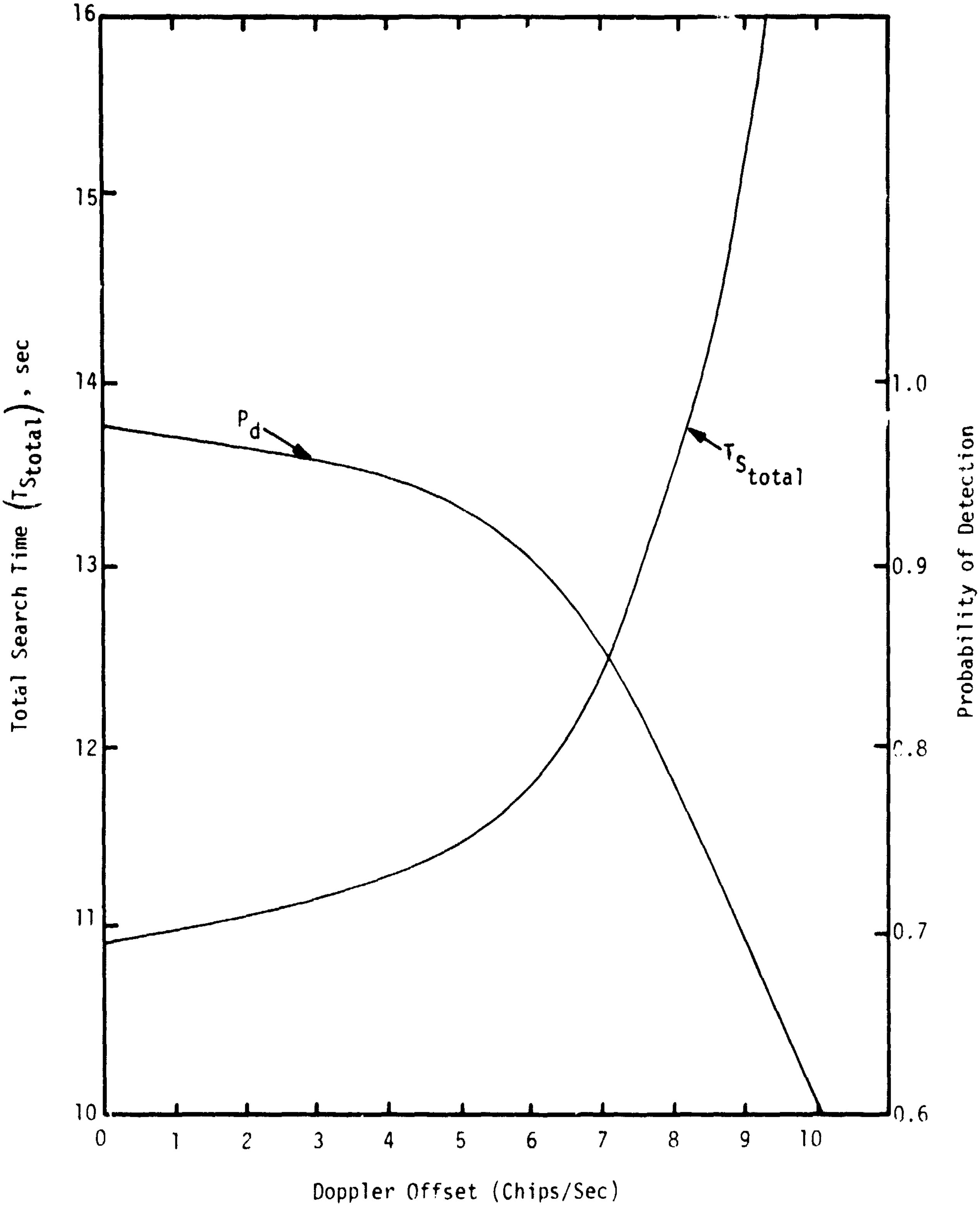

Figure 44. Effect of Doppler on Detection Probability and Total Average Synchronization Time

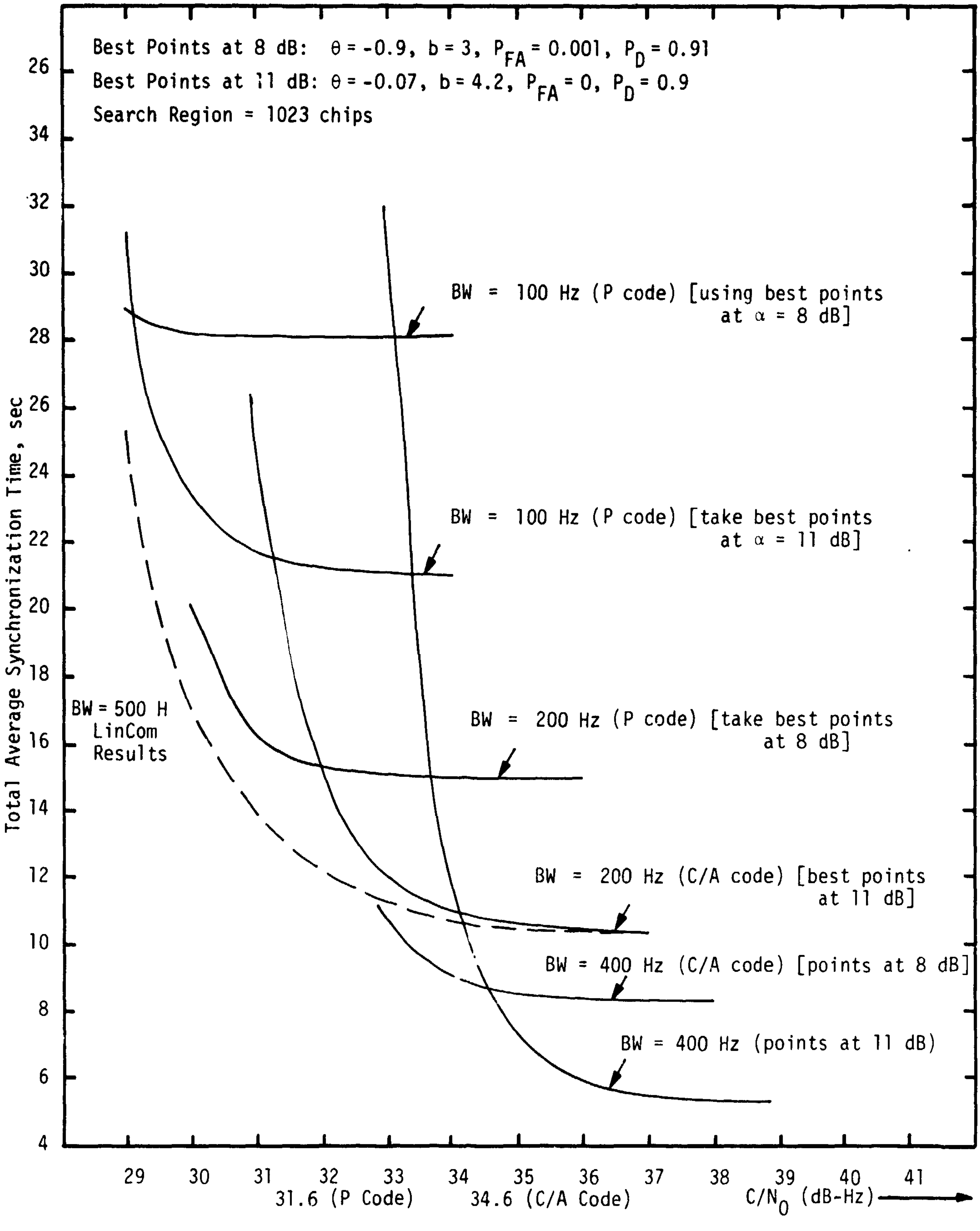

Figure 45. Variation of Total Synchronization Time With C/N_0 and Bandpass Filter Bandwidth B

7.0 GPS CARRIER ACQUISITION AND TRACKING

Most of the GPS user equipment designed to date employs an Automatic Frequency Control (AFC) loop to provide fast carrier acquisition and a Costas loop for carrier tracking during demodulation of the data. The composite AFC/Costas loop design provides two major advantages over a simple Costas loop: (1) the carrier can be acquired without sweeping, and (2) false lock due to data sidebands is avoided.

To form an AFC discriminator for the loop, it can be seen (ignoring noise) [5], that an unnormalized discriminator can be formed by

$$\hat{\omega} = I\frac{dQ}{dt} - Q\frac{dI}{dt} , \tag{73}$$

where I and Q are the in-phase and quadrature phase components of the signal, respectively. Approximating the time derivatives by finite time differences of τ, then neglecting the scaling by $1/\tau$, (73) becomes

$$\hat{\omega} = I(t-\tau)\,Q(t) - I(t)\,Q(t-\tau) . \tag{74}$$

Thus, for a frequency error $\Delta\omega$ and a sinusoidal signal,

$$\begin{aligned} I(t) &= \cos\,(\Delta\omega t + \phi) \\ Q(t) &= \sin\,(\Delta\omega t + \phi) . \end{aligned} \tag{75}$$

Substituting these values into (73) gives $\Delta\omega$ and into (74) gives

$$\begin{aligned} \Delta\hat{\omega} &= \cos\,(\Delta\omega t - \Delta\omega\tau + \phi)\,\sin\,(\Delta\omega t + \phi) - \cos\,(\Delta\omega t + \phi)\,\sin\,(\Delta\omega t - \Delta\omega\tau + \phi) \\ &= \frac{1}{2}[\sin\,(2\Delta\omega t - \Delta\omega\tau + 2\phi) + \sin\,(\Delta\omega\tau) - \sin\,(2\Delta\omega t - \Delta\omega\tau + 2\phi) - \sin\,(-\Delta\omega\tau)] \\ &= \sin\,(\Delta\omega\tau) . \end{aligned} \tag{76}$$

Therefore, using finite time differences, a control proportional to frequency error can be obtained if $|\Delta\omega\tau| \ll 1$. Note that (74) is not affected by BPSK data modulation unless a data bit transition occurs within the delay τ.

If noise is present as in the GPS receivers, the mean of $\Delta\omega$ is still given by (76), but there is a SNR penalty due to the multiplication of wideband noise processes in (74). To avoid this severe penalty, the delay τ can be realized by lowpass filters. Figure 46 illustrates a composite AFC/Costas loop where the AFC discriminator described by (74) is shown within the dashed lines.

When the composite loop is out of lock, a radian frequency error $\Delta\omega(t)$ exists in the phase detector output signals $\varepsilon_c(t)$ and $\varepsilon_s(t)$. Since, typically, the AFC loop bandwidth is small relative to the noise bandwidth of the RC arm filters, then the average AFC output signal $\langle\overline{w_0(t)}\rangle$ can be computed, assuming $\Delta\omega(t)$ fixed equal to $\Delta\omega$. In particular,

$$w_0(t) = K_1^2 K_m^2 S\{m(t)\hat{m}_c(t;\Delta\omega,\phi) \sin(\Delta\omega t + \phi) - m(t)\hat{m}_s(t;\Delta\omega,\phi)\cos(\Delta\omega t + \phi)\}, \tag{77}$$

where $m(t)$ is the BPSK data modulation, K_1^2 is the reference signal power, K_m is the in-phase and quadrature phase detector (multiplier) gain, S is the signal power, and

$$\hat{m}_s(t;\Delta\omega,\phi) \overset{\Delta}{=} G(p)\varepsilon_s(t) = G(p)\{m(t)\sin[\Delta\omega t + \phi]\}$$

$$\hat{m}_c(t;\Delta\omega,\phi) \overset{\Delta}{=} G(p)\varepsilon_c(t) = G(p)\{m(t)\cos[\Delta\omega t + \phi]\}. \tag{78}$$

Note that the differential equation resulting from filtering the signal by the RC filters $G(s)$ are written in compact form by introducing the Heaviside operator $p \overset{\Delta}{=} d/dt$.

The digital modulation $m(t)$ may be represented as

$$m(t) = \sum_{n=-\infty}^{\infty} a_n p(t - nT), \tag{79}$$

where $a_n = \pm 1$ is the data symbol sequence and $p(t)$ is the data pulse shape, e.g., for NRZ coding,

$$p(t) = \begin{cases} 1 & \text{for } -T/2 \le t \le T/2 \\ 0 & \text{elsewhere}. \end{cases} \tag{80}$$

Substituting (79) into (78),

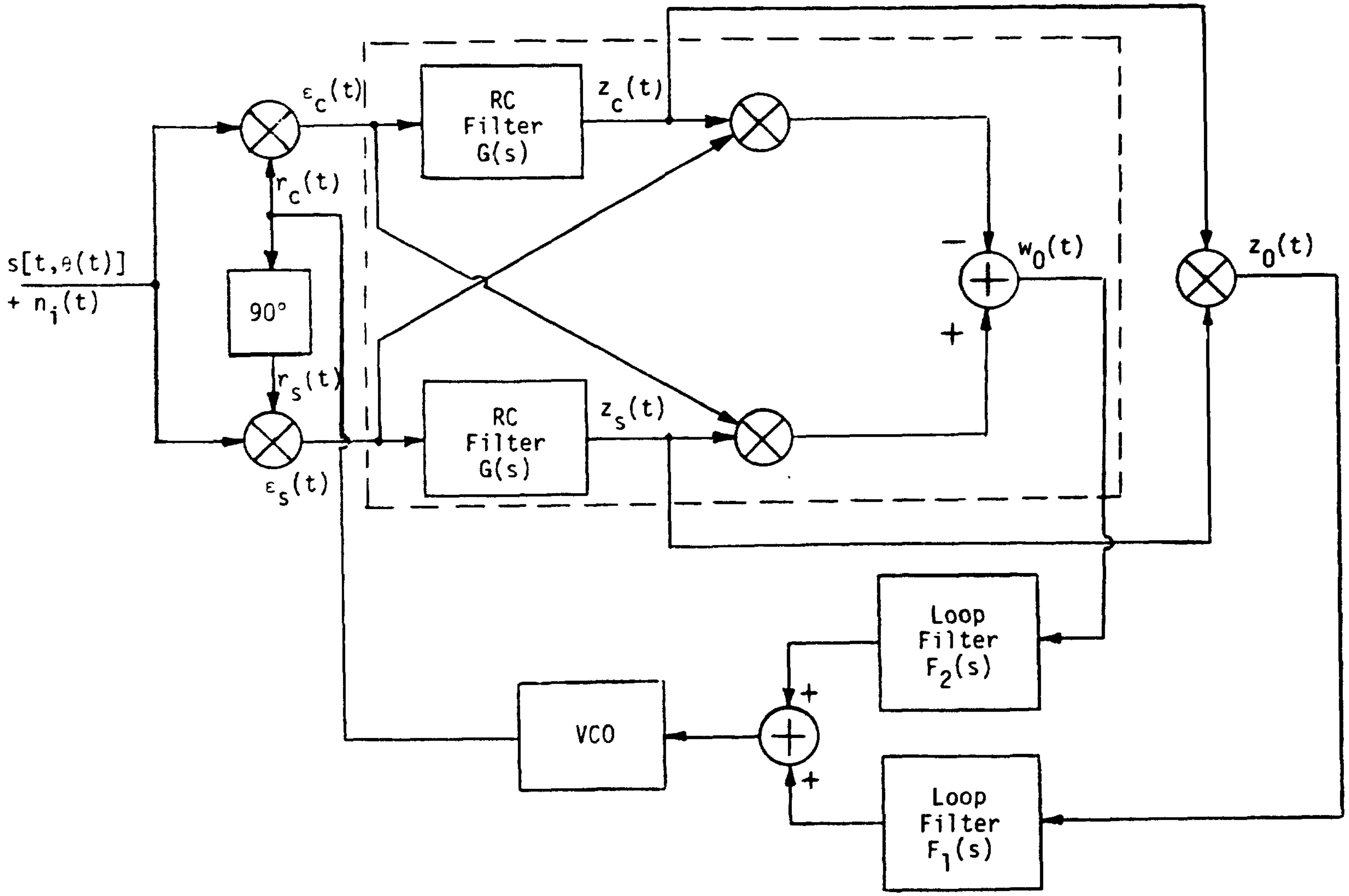

Figure 46. A Composite AFC/Costas Loop

$$\begin{aligned}\hat{m}_s(t;\Delta\omega,\phi) &= \sum_{n=-\infty}^{\infty} a_n \mathcal{F}^{-1}\{G(j\omega)\mathcal{F}[p(t-nT)\sin(\Delta\omega t+\phi)]\} \\ &= \frac{1}{2j}\left[\sum_{n=-\infty}^{\infty} a_n \hat{p}_1(t-nT)\, e^{j(\Delta\omega t+\phi)} - \sum_{n=-\infty}^{\infty} a_n \hat{p}_2(t-nT)\, e^{-j(\Delta\omega t+\phi)}\right]\end{aligned} \tag{81}$$

where $\mathcal{F}$ denotes the Fourier transform with $\mathcal{F}^{-1}$ its inverse and

$$\hat{p}_1(t) = \int_{-\infty}^{\infty} G[j(\omega+\Delta\omega)]\, P(j\omega)\, e^{j\omega t}\, \frac{d\omega}{2\pi}$$

$$\hat{p}_2(t) = \int_{-\infty}^{\infty} G[j(\omega-\Delta\omega)]\, P(j\omega)\, e^{j\omega t}\, \frac{d\omega}{2\pi}\,. \tag{82}$$

Similarly,

$$\hat{m}_c(t;\Delta\omega,\phi) = \frac{1}{2}\left[\sum_{n=-\infty}^{\infty} a_n \hat{p}_1(t-nT)\, e^{j(\Delta\omega t+\phi)} + \sum_{n=-\infty}^{\infty} a_n \hat{p}_2(t-nT)\, e^{-j(\Delta\omega t+\phi)}\right]. \tag{83}$$

Substituting (79), (81), and (83) into (77) and (78) gives

$$\begin{aligned}w_0(t) = K_1^2 K_m^2 S \Bigg\{ &\frac{1}{2j} \sum_{n=-\infty}^{\infty} \sum_{m=-\infty}^{\infty} a_n a_m \hat{p}_2(t-nT)\, p(t-mT) \\ &- \frac{1}{2j} \sum_{n=-\infty}^{\infty} \sum_{m=-\infty}^{\infty} a_n a_m \hat{p}_1(t-nT)\, p(t-mT)\Bigg\}\,,\end{aligned} \tag{84}$$

Taking both the statistical and time averages of (84) and recalling that, for random data,

$$\overline{a_n a_m} = \delta_{mn} = \begin{cases} 1; & m = n \\ 0; & m \neq n\,, \end{cases} \tag{85}$$

we get

$$\frac{\langle \overline{w_0(t)} \rangle}{K_1^2 K_m^2 S} = \frac{1}{2j} \lim_{T_0\to\infty} \frac{1}{T_0} \int_{-T_0/2}^{T_0/2} \sum_{n=-\infty}^{\infty} p(t-nT)[\hat{p}_2(t-nT) - \hat{p}_1(t-nT)]\, dt \tag{86a}$$

and

$$\frac{\langle\overline{w_0(t)}\rangle}{K_1^2\,K_m^2\,S} = \frac{1}{2j}\lim_{T_0\to\infty}\sum_{n=-\infty}^{\infty}\int_{-\infty}^{\infty}\int_{-\infty}^{\infty} G[j(\omega-\Delta\omega)]\,P(j\omega)\,P(-j\omega')$$

$$\times\frac{\sin[(\omega-\omega')T_0/2]}{(\omega-\omega')T_0/2}\,e^{-j(\omega-\omega')nT}\,\frac{d\omega}{2\pi}\,\frac{d\omega'}{2\pi}$$

$$-\frac{1}{2j}\lim_{T_0\to\infty}\sum_{n=-\infty}^{\infty}\int_{-\infty}^{\infty}\int_{-\infty}^{\infty} G[j(\omega+\Delta\omega)]\,P(j\omega)\,P(-j\omega')$$

$$\times\frac{\sin[(\omega-\omega')T_0/2]}{(\omega-\omega')T_0/2}\,e^{-j(\omega-\omega')nT}\,\frac{d\omega}{2\pi}\,\frac{d\omega'}{2\pi}\;. \qquad (86b)$$

Recognizing that

$$\sum_{n=-\infty}^{\infty} e^{-j(\omega-\omega')nT} = \frac{2\pi}{T}\sum_{k=-\infty}^{\infty}\delta\left(\omega-\omega'-\frac{2\pi k}{T}\right)\,, \qquad (87)$$

then (86) simplifies to

$$\frac{\langle\overline{w_0(t)}\rangle}{K_1^2\,K_m^2\,S} = \frac{1}{2jT}\lim_{T_0\to\infty}\sum_{k=-\infty}^{\infty}\int_{-\infty}^{\infty} G[j(\omega-\Delta\omega)]\,P(j\omega)\,P\left[-j\left(\omega-\frac{2\pi k}{T}\right)\right]$$

$$\times\frac{\sin\left[\frac{2\pi k}{T}\left(\frac{T_0}{2}\right)\right]}{\frac{2\pi k}{T}\left(\frac{T_0}{2}\right)}\,\frac{d\omega}{2\pi}$$

$$-\frac{1}{2jT}\lim_{T_0\to\infty}\sum_{k=-\infty}^{\infty}\int_{-\infty}^{\infty} G[j(\omega+\Delta\omega)]\,P(j\omega)\,P\left[-j\left(\omega-\frac{2\pi k}{T}\right)\right]$$

$$\times\frac{\sin\left[\frac{2\pi k}{T}\left(\frac{T_0}{2}\right)\right]}{\frac{2\pi k}{T}\left(\frac{T_0}{2}\right)}\,\frac{d\omega}{2\pi}\;. \qquad (88)$$

Since the only term in (88) which yields a nonzero contribution is that corresponding to k=0, then (88) reduces to

$$\frac{\langle\overline{w_0(t)}\rangle}{K_1^2 K_m^2 S} = \frac{1}{2j}\int_{-\infty}^{\infty} S_m(\omega)\left\{G[j(\omega-\Delta\omega)] - G[j(\omega+\Delta\omega)]\right\}\frac{d\omega}{2\pi}$$

$$= \int_{-\infty}^{\infty} S_m(\omega)\ \mathrm{Im}\left\{G[j(\omega-\Delta\omega)]\right\}\frac{d\omega}{2\pi}\ , \tag{89}$$

or, finally,

$$f(\Delta\omega)\ \triangleq\ \frac{\langle\overline{w_0(t)}\rangle}{K_1^2 K_m^2 S} = \int_{-\infty}^{\infty} S_m(\omega+\Delta\omega)\ \mathrm{Im}\left\{G(j\omega)\right\}\frac{d\omega}{2\pi}\ , \tag{90}$$

where

$$S_m(\omega)\ \triangleq\ \frac{1}{T}\left|P(j\omega)\right|^2 \tag{91}$$

is the power spectrum of the modulation m(t) and $\mathrm{Im}\{G(j\omega)\}$ denotes the imaginary part of the arm filter transfer function. Since G(s) is an RC filter with transfer function

$$G(j\omega) = \frac{1}{1 + j(\omega/\omega_c)} = \frac{-j(\omega/\omega_c)}{1 + (\omega/\omega_c)^2}\ ;\ \omega_c = \frac{1}{RC}\ , \tag{92}$$

then

$$\mathrm{Im}\left\{G(j\omega)\right\} = -\frac{\omega/\omega_c}{1 + (\omega/\omega_c)^2}\ . \tag{93}$$

Furthermore, for NRZ coded data,

$$S_m(\omega) = T\,\frac{\sin^2\left(\frac{\omega T}{2}\right)}{\left(\frac{\omega T}{2}\right)^2}\ . \tag{94}$$

Substituting (93) and (94) in (89), the desired discriminator characteristic is given by

$$f(\Delta\omega) = \frac{1}{\omega_c T\left[1+\left(\frac{\Delta\omega}{\omega_c}\right)^2\right]}\left\{\left[\frac{\Delta\omega}{\omega_c}\cos\Delta\omega T+\sin\Delta\omega T\right]e^{-\omega_c T}-\frac{\Delta\omega}{\omega_c}\right\}$$

$$+\frac{\frac{\Delta\omega}{\omega_c}}{1+\left(\frac{\Delta\omega}{\omega_c}\right)^2}+\frac{\frac{\Delta\omega}{\omega_c}}{\omega_c T\left[1+\left(\frac{\Delta\omega}{\omega_c}\right)^2\right]^2}\left\{\left(\frac{\Delta\omega}{\omega_c}\right)^2-1-e^{-\omega_c T}\left[\left[\left(\frac{\Delta\omega}{\omega_c}\right)^2-1\right]\cos\Delta\omega T\right.\right.$$

$$\left.\left.+2\left(\frac{\Delta\omega}{\omega_c}\right)\sin\Delta\omega T\right]\right\}. \tag{95}$$

Figure 47 illustrates $f(\Delta\omega)$ versus $\Delta\omega/\omega_c$ for $\omega_c T = 0.83\pi$ (the optimum ratio of arm filter 3 dB frequency to data rate for small ST/N_0; see [6]) and $\omega_c T = 1.66\pi$, respectively. The equivalent linear gain, $K_{\dot{\varphi}}$, of these discriminator characteristics is indicated on Figure 47 by dotted lines and is found analytically as follows. Assuming $\Delta\omega/\omega_c$ to be small, then from (95),

$$f(\Delta\omega) = \frac{\Delta\omega}{\omega_c}K_{\dot{\varphi}}, \tag{96}$$

where

$$K_{\dot{\varphi}} = 1-2\frac{\left[1-\left(1+\frac{\omega_c T}{2}\right)e^{-\omega_c T}\right]}{\omega_c T}. \tag{97}$$

Figure 48 is a plot of $K_{\dot{\varphi}}$ versus $f_c T = \omega_c T/2\pi$. Note from Figure 47 that, as $\omega_c T$ is increased, the linear gain $K_{\dot{\varphi}}$ increases but the region of linearity decreases. However, the region of linearity in frequency increases as $\omega_c T$ is increased. For example, if the region of linearity is defined as an error of less than 10%, then for $\omega_c T = 0.83\pi$, the region is $\Delta\omega = 0.68\ \omega_c$ or $\Delta f = 0.282/T$, but is $\Delta\omega = 0.446\ \omega_c$ or $\Delta f = 0.370/T$ for $\omega_c T = 1.66\pi$. Figure 49 plots the region of linearity $\Delta f_{max}T$ versus $f_c T$. Since $K_{\dot{\varphi}}$ is approximately 1 for $f_c T \geq 10$, the region of linearity is approximately

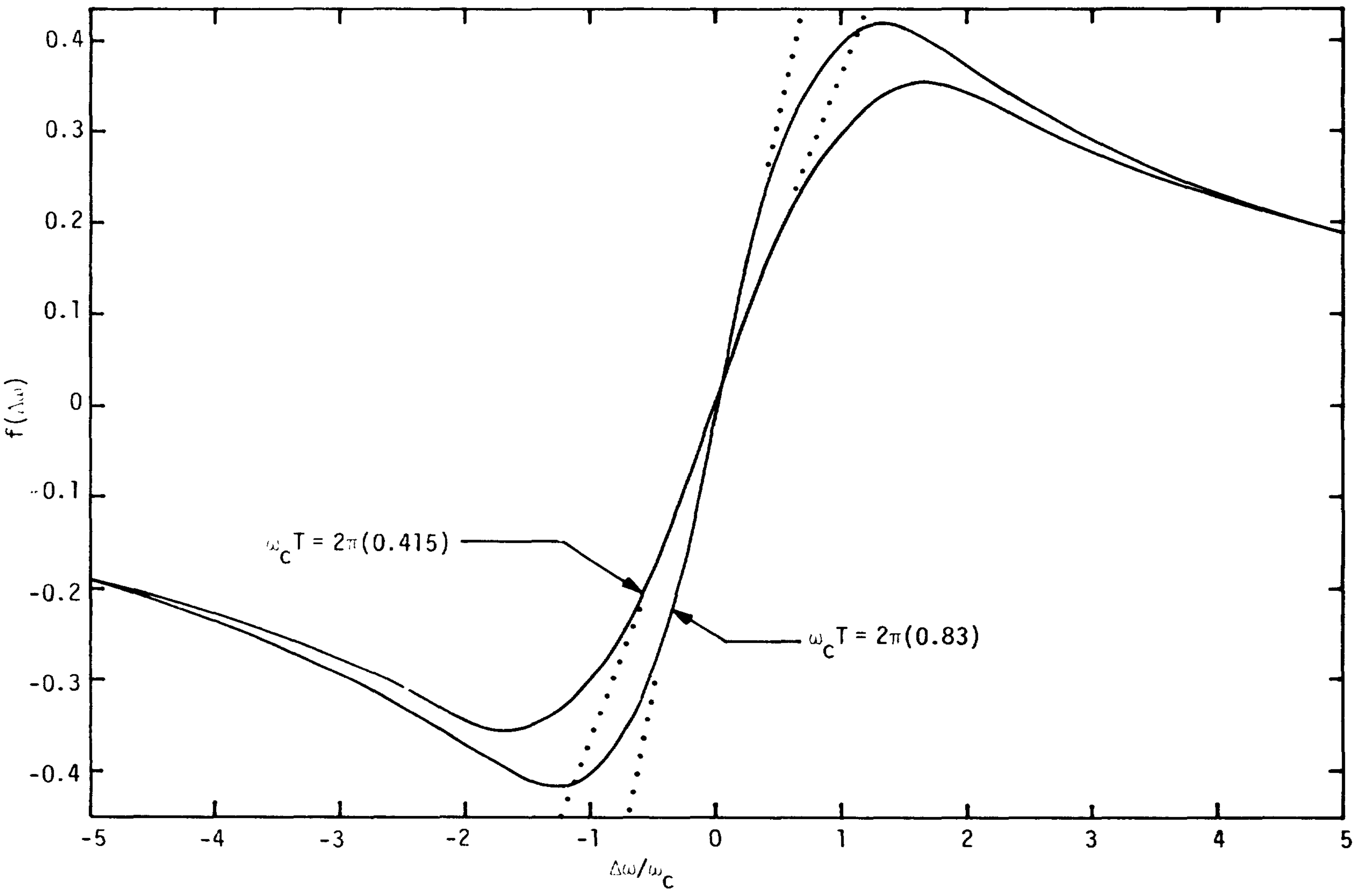

Figure 47. AFC Discriminator Characteristics

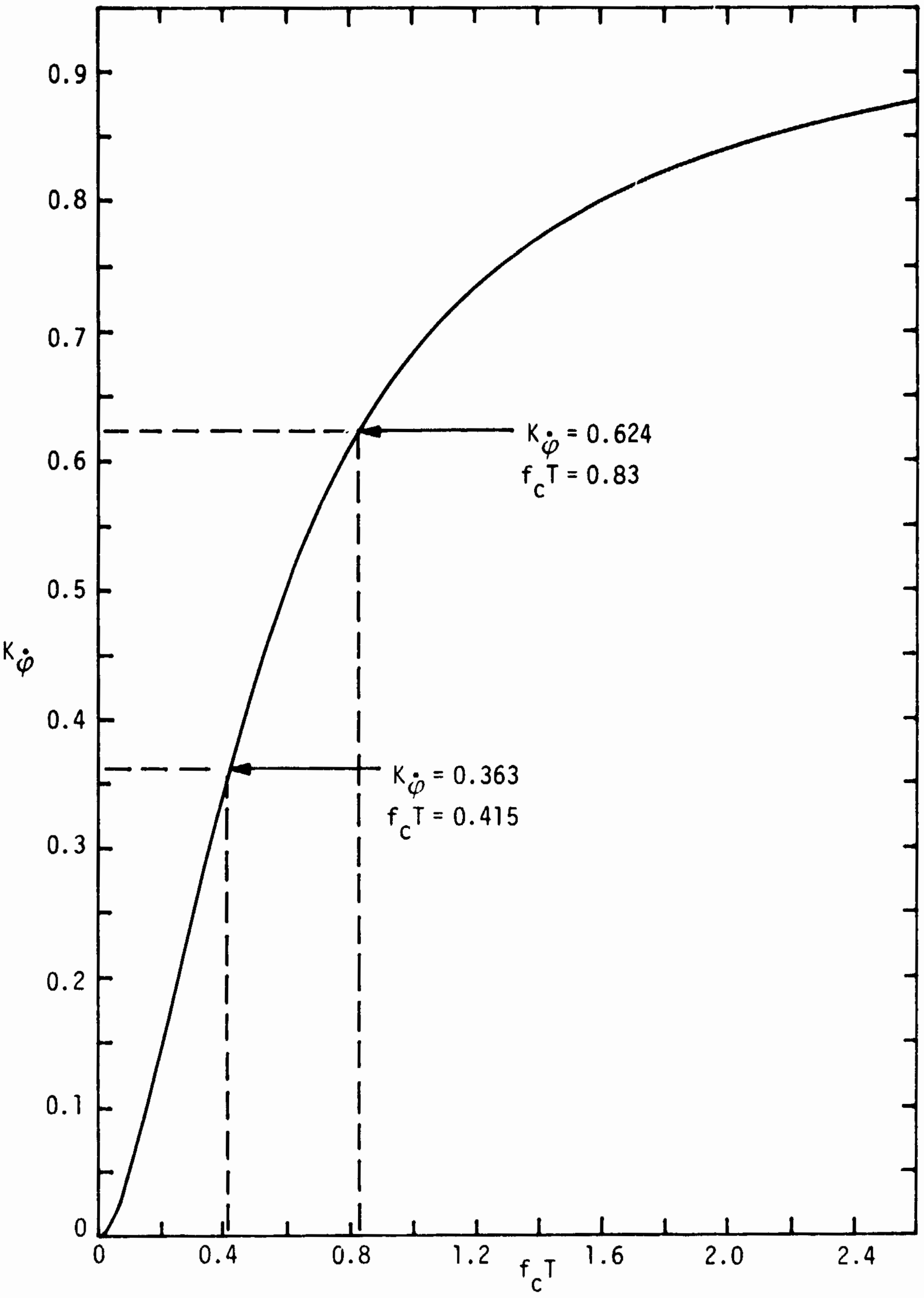

Figure 48. Discriminator Linear Gain Versus Ration of Arm Filter 3 dB Cutoff Frequency to Data Rate

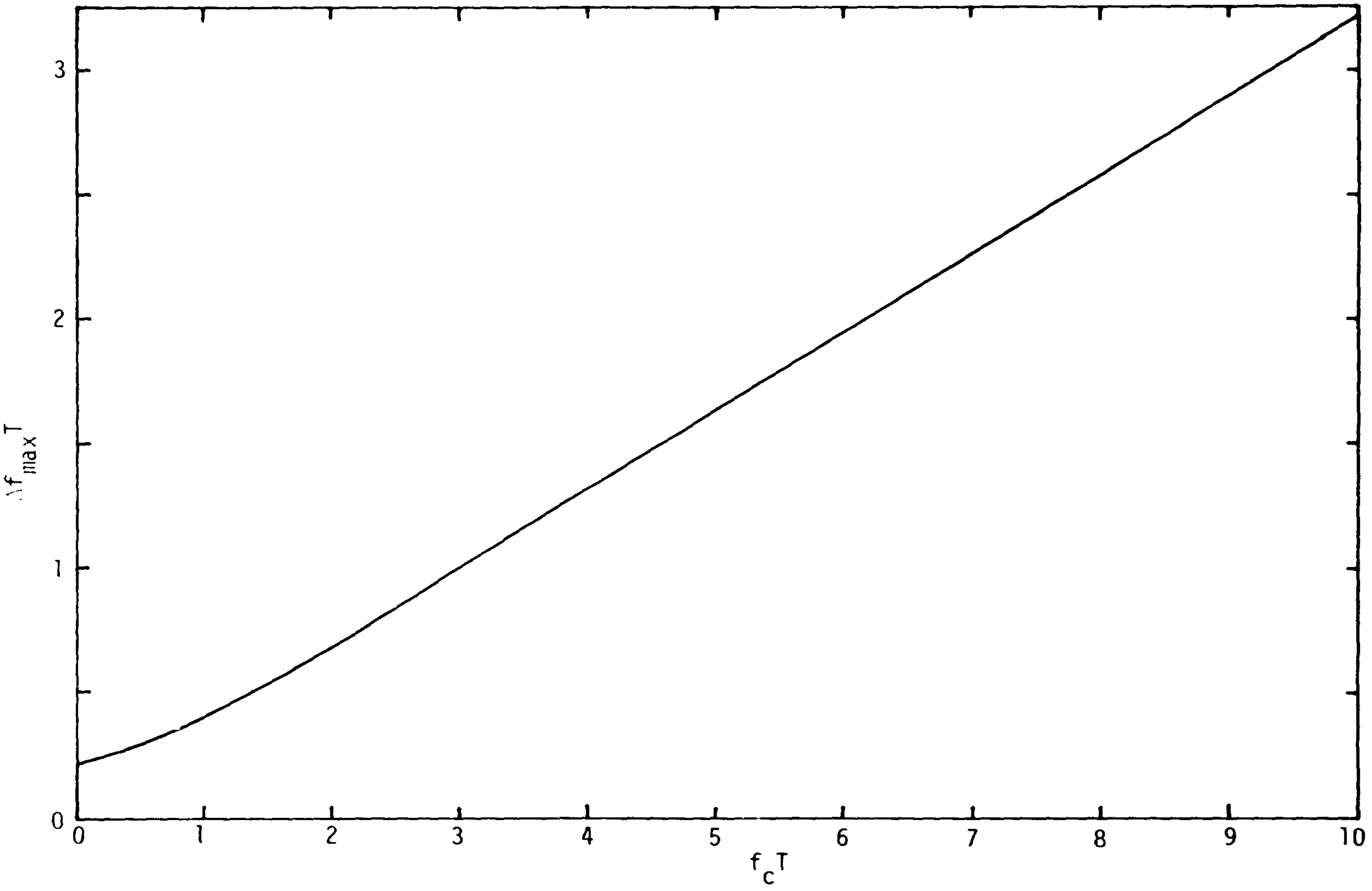

Figure 49. Region of Linearity for AFC Discriminator

$$\Delta f_{max} T \simeq 0.322\, f_c T \qquad \text{for } f_c T \geq 10\,. \tag{98}$$

7.1 AFC Loop Response - Linear Model

We observe from Figure 47 that, for a given value of $\omega_c T$, the discriminator characteristic is linear over a certain range of frequency offset and, in particular, is described by (96) in this region. Moreover, since (95) and hence (96) were derived under the assumption of a constant frequency offset, i.e., $\omega(t) - \hat{\omega}(t) = \Delta\omega$, then from Figure 46, the closed loop AFC response is described by

$$\hat{\omega}(t) = K_V F_2(p) K_1^2 K_m^2 S K_{\dot{\varphi}} \left(\omega(t) - \hat{\omega}(t)\right) \Big/ \omega_c \tag{99}$$

or, in Laplace Transform notation,

$$\frac{\hat{\omega}(s)}{\omega(s)} = \frac{S K K_{\dot{\varphi}} F_2(s) / \omega_c}{1 + S K K_{\dot{\varphi}} F_2(s) / \omega_c}\,, \tag{100}$$

where K_V is the VCO gain in rad/sec/v and $K \triangleq K_V K_1^2 K_m^2$.* Assuming that $F_2(s)$ is an imperfect integrating filter, i.e.,

$$F_2(s) = \frac{1 + s\tau_{22}}{1 + s\tau_{12}}\,, \tag{101}$$

then

$$\frac{\hat{\omega}(s)}{\omega(s)} = \frac{S K K_{\dot{\varphi}} (1 + s\tau_{22})/\omega_c}{1 + S K K_{\dot{\varphi}}/\omega_c + s\,(\tau_{12} + S K K_{\dot{\varphi}} \tau_{22}/\omega_c)}\,, \tag{102}$$

which implies a <u>first-order loop</u> response with radian cutoff frequency

$$\omega_{nF} = \frac{1 + S K K_{\dot{\varphi}}/\omega_c}{\tau_{12} + S K K_{\dot{\varphi}} \tau_{22}/\omega_c}\,. \tag{103}$$

---

*$K_{\dot{\varphi}}$ is not included in the definition of K since it is actually a function of $\omega_c T$ rather than a constant.

If a conventional Costas loop were to employ $F_2(s)$ of (101) as its loop filter, then the loop response would be <u>second-order</u> and characterized by the following parameters:

$$r_2 \triangleq S K D_m \tau_{22} F_{02} \,; \qquad F_{02} \triangleq \frac{\tau_{22}}{\tau_{12}}$$

$$\omega_{n2} = \frac{\sqrt{r_2}}{\tau_{22}} \tag{104}$$

In (104) ω_{n2} is the <u>natural frequency</u> of the loop, and for small F_{02} (the usual case in design),

$$r_2 \cong 4\zeta_2^2 \,, \tag{105}$$

where ζ_2 is the loop's <u>damping factor</u>. Also in (104),

$$D_m \triangleq \int_{-\infty}^{\infty} S_m(\omega)\, |G(j\omega)|^2 \, \frac{d\omega}{2\pi} \tag{106}$$

is the <u>data modulation distortion factor</u> (equivalent power reduction due to arm filters).* Using these definitions in (102), we obtain

$$\frac{\hat{\omega}(s)}{\omega(s)} = \left(\frac{K_{\dot\varphi}}{D_m\omega_c}\right) \frac{\omega_{n2}^2 + s\sqrt{r_2}\,\omega_{n2}}{\frac{\omega_{n2}}{\sqrt{r_2}}\left(F_{02} + \frac{K_{\dot\varphi}}{D_m\omega_c}\sqrt{r_2}\,\omega_{n2}\right) + s\left(1 + \frac{K_{\dot\varphi}}{D_m\omega_c}\sqrt{r_2}\,\omega_{n2}\right)} \tag{107}$$

$$\omega_{nF} = \frac{\omega_{n2}}{\sqrt{r_2}} \left[\frac{F_{02} + \frac{K_{\dot\varphi}}{D_m\omega_c}\sqrt{r_2}\;\omega_{n2}}{1 + \frac{K_{\dot\varphi}}{D_m\omega_c}\sqrt{r_2}\;\omega_{n2}}\right] . \tag{108}$$

The function $K_{\dot\varphi}/(D_m\omega_c)$ which appears in many places in (107) and (108) can be evaluated as follows. For an RC arm filter and NRZ data, one can show from (106) that

---

*The parameter D_m, like $K_{\dot\varphi}$, is a function of $\omega_c T$.

$$D_m = 1 - \frac{1}{\omega_c T}\left(1 - e^{-\omega_c T}\right). \tag{109}$$

Thus, from (97) and (109),

$$\frac{K_{\dot{\varphi}}}{D_m \omega_c} = \left(\frac{K_{\dot{\varphi}}}{D_m \omega_c T}\right) T \triangleq K_c T, \tag{110}$$

with

$$K_c = \left(\frac{1}{\omega_c T}\right) \frac{\omega_c T - 2 + (2 + \omega_c T)\, e^{-\omega_c T}}{\omega_c T - 1 + e^{-\omega_c T}}. \tag{111}$$

For example, at the small ST/N_0 optimum design ratio of arm filter cutoff frequency to data rate, viz., $\omega_c T = 0.83\pi$, then $K_c = 0.216$. Figure 50 plots K_c versus $f_c T$. Note that, for $f_c T \geq 10$, $K_c = 1/\omega_c T$.

7.2 AFC Loop Response to an Input Frequency Step

Using (110), we can write (107) in the form

$$\frac{\hat{\omega}(s)}{\omega(s)} = K_c T \left[\frac{A + Bs}{C + Ds}\right] = K_c T \left[\frac{A - \frac{BC}{D}}{C + Ds} + \frac{B}{D}\right], \tag{112}$$

where

$$A = \omega_{n2}^2 ; \qquad B = \sqrt{r_2}\, \omega_{n2} ;$$

$$C = \frac{\omega_{n2}}{\sqrt{r_2}}\left(F_{02} + K_c T \sqrt{r_2}\, \omega_{n2}\right) ; \qquad D = 1 + K_c T \sqrt{r_2}\, \omega_{n2} . \tag{113}$$

If $\omega(t)$ is now a frequency step $\Lambda_0 u(t)$, i.e., $\omega(s) = \Lambda_0/s$, then

$$\hat{\omega}(s) = K_c T \left[\frac{\Lambda_0}{s}\left(\frac{A - \frac{BC}{D}}{C + Ds}\right) + \frac{\Lambda_0 \frac{B}{D}}{s}\right]$$

$$= K_c T \frac{A}{C} \Lambda_0 \left[\frac{1}{s} - \frac{1 - \frac{B/D}{A/C}}{s + C/D}\right]. \tag{114}$$

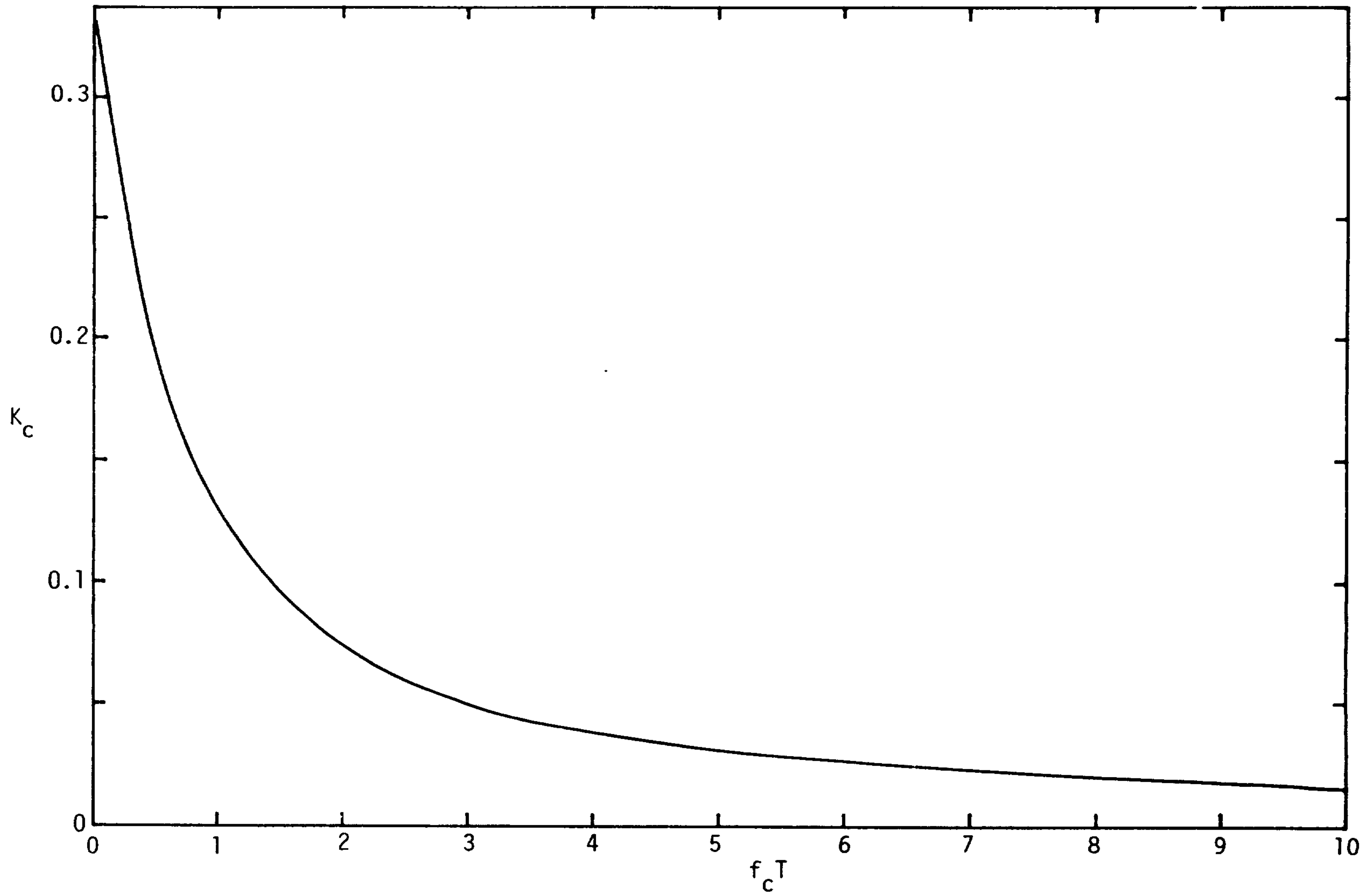

Figure 50. Gain Constant K_c Versus f_cT

From (113),

$$1 - \frac{B/D}{A/C} = \frac{1 - F_{02}}{1 + K_c T \sqrt{r_2}\, \omega_{n2}} \doteq \frac{1}{1 + K_c T \sqrt{r_2}\, \omega_{n2}} = \frac{1}{D} , \tag{115}$$

since $F_{02} \ll 1$. To simplify (114) any further, we must express $K_c T \sqrt{r_2}\, \omega_{n2}$ in the denominator of (115) in terms of the parameters of the conventional Costas loop portion of the overall composite loop. Assuming for $F_1(s)$ an imperfect integration filter of the form

$$F_1(s) = \frac{1 + s\tau_{21}}{1 + s\tau_{11}} , \tag{116}$$

then the Costas loop is <u>second-order</u> with parameters [analogous to (104)]

$$\begin{aligned} r_1 &\triangleq S K D_m \tau_{21} F_{01} ; & F_{01} &\triangleq \frac{\tau_{21}}{\tau_{11}} \\ \omega_{n1} &= \frac{\sqrt{r_1}}{\tau_{21}} ; & B_{L1} &\doteq \frac{r_1 + 1}{4\tau_{21}} \end{aligned} \tag{117}$$

where, in addition, B_{L1} is the single-sided bandwidth of the Costas loop portion alone. Thus, from (104) and (117), we have that

$$\begin{aligned} K_c T \sqrt{r_2}\, \omega_{n2} &= K_c T S K D_m F_{02} \\ &= K_c T \frac{r_1}{\tau_{21}} \left(\frac{F_{02}}{F_{01}}\right) = K_c \left(\frac{4 r_1}{r_1 + 1}\right) \left(\frac{F_{02}}{F_{01}}\right) B_{L1} T . \end{aligned} \tag{118}$$

Since a conventional Costas loop is typically designed for critical damping ($r_1 = 2$) and $B_{L1} T \ll 1$, then if we arbitrarily choose $F_{02} \simeq F_{01}$, we have that

$$K_c T \sqrt{r_2}\, \omega_{n2} = K_c \left(\frac{8}{3}\right) \left(\frac{F_{02}}{F_{01}}\right) B_{L1} T \ll 1 \tag{119}$$

or equivalently, from (113) and (115),

$$D \doteq 1 ; \qquad 1 - \frac{B/D}{A/C} \doteq 1 . \tag{120}$$

Thus, (112) simplifies to

$$\frac{\hat{\omega}(s)}{\omega(s)} = K_c T\left(\frac{A}{s + C}\right) = K_c T\left(\frac{\omega_{n2}^2}{s + \omega_{nF}}\right) \tag{121}$$

and accordingly, (114) becomes

$$\hat{\omega}(s) = K_c T \frac{A}{C} \Lambda_0 \left[\frac{1}{s} - \frac{1}{s + C}\right] \tag{122}$$

$$= \frac{\Lambda_0}{1 + \dfrac{F_{02}}{K_c T \sqrt{r_2}\, \omega_{n2}}} \left[\frac{1}{s} - \frac{1}{s + \omega_{nF}}\right]$$

$$= \frac{\Lambda_0}{1 + \dfrac{3F_{01}}{8K_c B_{L1} T}} \left[\frac{1}{s} - \frac{1}{s + \omega_{nF}}\right] . \tag{123}$$

The equivalent time domain response is then

$$\hat{\omega}(t) = \frac{\Lambda_0}{1 + \xi} \left[1 - e^{-\omega_{nF} t}\right] u(t) , \tag{124}$$

where we have defined

$$\xi = \frac{3 F_{01}}{8 K_c B_{L1} T} . \tag{125}$$

The corresponding frequency error response, $\varphi(t) = \omega(t) - \hat{\omega}(t)$, is given by

$$\varphi(t) = \Lambda_0 \left(\frac{\xi}{1 + \xi}\right) u(t) + \frac{\Lambda_0}{1 + \xi} e^{-\omega_{nF} t} u(t) . \tag{126}$$

Furthermore, since from (121), the AFC acts like a first-order loop, its two-sided noise bandwidth W_{LF} is related to ω_{nF} by

$$W_{LF} = \frac{\dfrac{1}{2\pi j} \displaystyle\int_{-j\infty}^{j\infty} \left(\frac{\hat{\omega}(s)}{\omega(s)}\right) \left(\frac{\hat{\omega}(-s)}{\omega(-s)}\right) ds}{\left|\dfrac{\hat{\omega}(0)}{\omega(0)}\right|^2} ; \tag{127a}$$

or

$$W_{LF} = \frac{1}{2\pi j}\int_{-j\infty}^{j\infty}\left(\frac{\omega_{nF}}{s+\omega_{nF}}\right)\left(\frac{\omega_{nF}}{-s+\omega_{nF}}\right)ds = \frac{\omega_{nF}}{2}\,. \tag{127b}$$

Alternately, the single-sided noise bandwidth $B_{LF} \overset{\Delta}{=} W_{LF}/2$ is related to ω_{nF} by

$$B_{LF} = \frac{\omega_{nF}}{4}\,. \tag{128}$$

Substituting (128) into (126), we obtain the desired radian frequency error response:

$$\dot{\varphi}(t) = \Lambda_0\left(\frac{\xi}{1+\xi}\right)u(t) + \frac{\Lambda_0}{1+\xi}e^{-4B_{LF}t}\,u(t)\,. \tag{129}$$

7.3 Acquisition Behavior of the Composite AFC/Costas Loop in the Absence of Noise

It is well known that an imperfect second-order phase-locked loop is characterized by a finite acquisition range (often called capture or pull-in range) which represents the largest frequency difference between the frequency of the received carrier and that of the VCO for which phase-lock will occur. Typically for high-gain loops, this acquisition range (relative to the loop-bandwidth) is solely a function of the loop damping and the ratio of the time constants of the imperfect loop filter. In view of the similarity between the differential equations of operation of the conventional Costas loop and the phase-locked loop, one might expect the two to have similar acquisition behavior. Since, in effect, a Costas loop reconstructs and tracks a phantom carrier at twice the input frequency, the above statement is indeed true, at least for frequency errors on the order of the loop bandwidth. The similarity to a phase-locked loop, however, tends to break down as the frequency error becomes large, due to the tendency of the Costas loop to false lock to a sideband of the data modulation. Such a false lock phenomenon does not occur in a phase-locked loop, since it tracks an unmodulated carrier. This false lock tendency of the Costas loop often prohibits acquisition by sweeping the VCO frequency over the range of frequency uncertainty, particularly if the false lock frequencies, which occur at integer multiples of half the data rate, fall within the uncertainty region.

The addition of the AFC network to a conventional Costas loop considerably improves the false lock problem and increases the acquisition range to a value on the order of the arm filter bandwidth.

To begin the analysis of the acquisition behavior of the composite AFC/Costas loop, we present (by analogy to the phase-locked loop) the results for acquisition range and frequency acquisition time* for the Costas loop portion alone.

For a phase-locked loop with frequency error Δf, the loop will lock if [7]:

$$|\Delta f| \leq \frac{B_L}{\pi}\left(\frac{2r}{r+1}\right)\sqrt{\frac{2}{F_0} - 1} \tag{130}$$

and the corresponding time to achieve the frequency lock is [7]:

$$T_f = \left(\frac{r+1}{4B_L}\right)\frac{\left[\frac{\pi}{2}\left(\frac{r+1}{r}\right)\left(\frac{\Delta f}{B_L}\right)\right]^2 - \frac{1}{2}\ln\left[\pi\left(\frac{r+1}{r}\right)\left(\frac{\Delta f}{B_L}\right)\right]}{1 - \frac{F_0}{2-F_0}\left[\frac{\pi}{2}\left(\frac{r+1}{r}\right)\left(\frac{\Delta f}{B_L}\right)\right]^2} . \tag{131}$$

Since the differential equation of operation of the Costas loop is identical in form to that of the phase-locked loop except that ϕ is replaced by 2ϕ and Δf by $2\Delta f$, then (130) and (131) apply for the Costas loop if Δf is replaced by $2\Delta f$. In particular, for the Costas loop portion of the composite loop of Figure 46, we have that frequency lock is achieved if

$$|\Delta f| < \frac{B_{L1}}{\pi}\left(\frac{r_1}{r_1+1}\right)\sqrt{\frac{2}{F_{01}} - 1} \tag{132}$$

and the time to reach this condition is

---

[*] We shall ignore the phase stabilization time (the additional time to reach phase lock once frequency lock has been established) since this time has only a small effect on acquisition time for appreciable initial frequency errors.

$$T_f = \left(\frac{r_1+1}{4B_{L1}}\right) \frac{\left[\frac{\pi}{2}\left(\frac{r_1+1}{r_1}\right)\left(\frac{2\Delta f}{B_{L1}}\right)\right]^2 - \frac{1}{2}\ln\left[\pi\left(\frac{r_1+1}{r_1}\right)\left(\frac{2\Delta f}{B_{L1}}\right)\right]}{1 - \frac{F_{01}}{2-F_{01}}\left[\frac{\pi}{2}\left(\frac{r_1+1}{r_1}\right)\left(\frac{2\Delta f}{B_{L1}}\right)\right]^2} , \qquad (133)$$

where B_{L1}, r_1, and F_{01} are the loop parameters defined in (122).

Since the AFC increases the acquisition range by producing a restoring force proportional to the frequency error [see (95) or its linear equivalent (96)], it is essential that the value of initial frequency error be such that the AFC can reduce this error to a value within the pull-in range of the Costas loop. Since, from (129), the initial radian frequency error can, in the limit as t approaches infinity, be reduced no further than $\Lambda_0\xi/(1+\xi)$, then for acquisition of the composite loop, we require that

$$\frac{\Lambda_0\,\xi}{1+\xi} < 2\pi\left[\frac{B_{L1}}{\pi}\left(\frac{r_1}{r_1+1}\right)\sqrt{\frac{2}{F_{01}}-1}\right] . \qquad (134)$$

Letting $r_1 = 2$ and using the corresponding definition of ξ given in (125), we arrive at the inequality

$$\frac{\frac{3}{8K_c}\left(\frac{F_{01}}{B_{L1}T}\right)}{1+\frac{3}{8K_c}\left(\frac{F_{01}}{B_{L1}T}\right)} < \frac{1}{\frac{3\Lambda_0 T}{4}\left(\frac{F_{01}}{B_{L1}T}\right)}\sqrt{2F_{01} - F_{01}^2} . \qquad (135)$$

Since, from Figure 47, the AFC discriminator characteristic is approximately linear over the frequency range $\Delta\omega < 0.68\,\omega_c$ for $\omega_c T = 0.83\pi$ with slope K_{ϕ}, then the maximum acquisition range of the composite loop is approximately

$$\frac{|\Delta f|}{B_{L1}} < \left(\frac{0.68\,\omega_c T}{2\pi}\right)\frac{1}{B_{L1}T} = \frac{0.282}{B_{L1}T} . \qquad (136)$$

If Λ_0 is set equal to $0.68\,\omega_c$ and $F_{01} = 0.001$, then at $\omega_c T = 0.83\pi$, the inequality in (135) can be reduced to

$$B_{L1}T > 0.00637 . \qquad (137)$$

In view of (137), for $r_1 = 2$ and $F_{01} = 0.001$, then from (136)

$$\left(\frac{|\Delta f|}{B_{L1}}\right)_{max} < 44.27 \,. \tag{138}$$

The corresponding maximum acquisition range for the Costas loop alone and the same loop parameters is obtained from (132) and is given by

$$\left(\frac{|\Delta f|}{B_{L1}}\right)_{max} = 9.488 \,. \tag{139}$$

Thus, a modest improvement in acquisition range is possible through the addition of the AFC. More important, however, this increased acquisition range is accompanied by a considerably reduced acquisition time.

When the frequency error is large, the behavior of the composite loop is controlled primarily by the AFC loop. Thus, the time t_1 to reduce the frequency error from its initial value $\Delta f_0 \overset{\Delta}{=} \Lambda_0/2\pi$ to another value, say Δf_1, can be determined from (128), viz.,

$$2\pi\Delta f_1 = 2\pi\Delta f_0\left(\frac{\xi}{1+\xi}\right) + \frac{2\pi\Delta f_0}{1+\xi}e^{-4B_{LF}t_1} \tag{140}$$

or

$$t_1 = -\frac{1}{4B_{LF}} \ln\left\{\left[\frac{\Delta f_1}{\Delta f_0} - \frac{\xi}{1+\xi}\right](1+\xi)\right\} \,. \tag{141}$$

When Δf_1 becomes within the pull-in range of the Costas loop, then the time t_2 to complete the frequency acquisition process is determined by the combined action of the AFC and Costas loops. This time will, in general, be less than that computed for the Costas loop alone attempting to achieve frequency lock from an initial frequency error of Δf_1. The latter is computed from (133) with Δf replaced by Δf_1. Since an expression for t_2 is difficult to obtain, we shall upper bound t_2 by the value t_2' computed for the Costas loop acting alone as discussed above. Thus, we propose to upper bound the acquisition time T_{ACQ} of the composite loop by the sum of t_1 as determined by (141) and t_2' as determined by (133) with Δf_1 replacing Δf. Since Δf_1 is thus far arbitrary, we shall choose its value so as to minimize $T_{ACQ}' = t_1 + t_2'$. Furthermore, if Δf_1 is considerably less than the pull-in range of the Costas loop, then the acquisition time formula of (133) simplifies to

$$t_2' \cong \frac{r_1+1}{4\,B_{L1}} \left\{ \left[\frac{\pi}{2} \left(\frac{r_1+1}{r_1} \right) \left(\frac{2\Delta f_1}{B_{L1}} \right) \right]^2 - \frac{1}{2} \ln \left[\pi \left(\frac{r_1+1}{r_1} \right) \left(\frac{2\Delta f_1}{B_{L1}} \right) \right] \right\} . \tag{142}$$

We shall make this assumption in what follows and check its region of validity later on. Since we wish to choose Δf_1 so as to minimize $T_{ACQ} = t_1 + t_2'$, we can differentiate T_{ACQ} with respect to Δf_1 and equate the resulting expression to zero. Letting

$$C = \frac{\pi}{2} \left(\frac{r_1+1}{r_1} \right) \frac{1}{B_{L1}}$$

and (143)

$$x = 2\Delta f_1 \ ,$$

we have from (141) and (142) that

$$T_{ACQ}' = -\frac{1}{4B_{LF}} \ln \left\{ \frac{(1+\xi)\,x}{2\Delta\,f_0} - \xi \right\} + \left(\frac{r_1+1}{4\,B_{L1}} \right) \left\{ C^2x^2 - \frac{1}{2} \ln 2\,C\,x \right\} . \tag{144}$$

Thus,

$$\frac{\partial\,T_{ACQ}'}{\partial\,x} = -\frac{1}{4\,B_{LF} \left\{ x - \dfrac{2\Delta f_0\,\xi}{1+\xi} \right\}} + \frac{(r_1+1)}{4\,B_{L1}} \left[2\,C^2\,x - \frac{1}{2x} \right] = 0 \ , \tag{145}$$

or, after simplification,

$$x^3 - \frac{2\Delta f_0\,\xi}{1+\xi}\,x^2 - \left[\frac{1}{4C^2} + \frac{1}{2C^2\,(r_1+1)\,\dfrac{B_{LF}}{B_{L1}}} \right] x + \frac{\Delta f_0\,\xi}{2C^2\,(1+\xi)} = 0 \ . \tag{146}$$

A cubic equation of the form $x^3 + px^2 + qx + r = 0$ may be reduced to

$$y^3 + ay + b = 0 \tag{147}$$

by substituting for x the value of $y - p/3$. Here,

$$a = q - \frac{p^2}{3}$$

$$b = \frac{1}{27}(2p^3 - 9pq + 27r) \ . \qquad (148)$$

The case of interest here is where

$$\frac{b^2}{4} + \frac{a^3}{27} < 0 \ , \qquad (149)$$

for which there will be three real and unequal roots. These solutions for y are obtained as follows. Compute the value of the angle θ in the expression

$$\cos\theta = \frac{b/2}{\sqrt{-\frac{a^3}{27}}} \ . \qquad (150)$$

Then the three solutions y_1, y_2, and y_3 are

$$\begin{aligned} y_1 &= 2\sqrt{-\frac{a}{3}}\ \cos\frac{\theta}{3} \\ y_2 &= 2\sqrt{-\frac{a}{3}}\ \cos\left(\frac{\theta}{3} + \frac{2\pi}{3}\right) \qquad (151) \\ y_3 &= 2\sqrt{-\frac{a}{3}}\ \cos\left(\frac{\theta}{3} + \frac{4\pi}{3}\right) \end{aligned}$$

or, equivalently, the three solutions for x are

$$\begin{aligned} x_1 &= 2\sqrt{-\frac{a}{3}}\ \cos\frac{\theta}{3} - \frac{p}{3} \\ x_2 &= 2\sqrt{-\frac{a}{3}}\ \cos\left(\frac{\theta}{3} + \frac{2\pi}{3}\right) - \frac{p}{3} \qquad (152) \\ x_3 &= 2\sqrt{-\frac{a}{3}}\ \cos\left(\frac{\theta}{3} + \frac{4\pi}{3}\right) - \frac{p}{3} \ . \end{aligned}$$

Comparing (146) and (147) and normalizing x by $2\Delta f_0$, we find that, corresponding to (152), we have the three solutions

$$\frac{x_1}{2\Delta f_0} = 2\sqrt{-\frac{a'}{3}}\ \cos\frac{\theta'}{3} + \frac{\xi}{3(1+\xi)}$$

$$\frac{x_2}{2\Delta f_0} = 2\sqrt{-\frac{a'}{3}}\ \cos\left(\frac{\theta'}{3} + \frac{2\pi}{3}\right) + \frac{\xi}{3(1+\xi)}$$

$$\frac{x_3}{2\Delta f_0} = 2\sqrt{-\frac{a'}{3}}\ \cos\left(\frac{\theta'}{3} + \frac{4\pi}{3}\right) + \frac{\xi}{3(1+\xi)}\ , \tag{153}$$

where

$$\theta' = \cos^{-1}\left\{-\frac{\frac{b'}{2}}{\sqrt{-\frac{a'^3}{27}}}\right\} \tag{154}$$

and

$$a' \triangleq \frac{a}{(2\Delta f_0)^2} = -\left\{\frac{\left(\frac{r_1}{r_1+1}\right)^2}{2\pi^2\left(\frac{\Delta f_0}{B_{L1}}\right)^2}\left[\frac{1 + \frac{(r_1+1)}{2}\frac{B_{LF}}{B_{L1}}}{(r_1+1)\frac{B_{LF}}{B_{L1}}}\right] + \frac{1}{3}\left(\frac{\xi}{1+\xi}\right)^2\right\}$$

$$b' \triangleq \frac{b}{(2\Delta f_0)^3} = -\frac{2}{27}\left(\frac{\xi}{1+\xi}\right)\left\{\left(\frac{\xi}{1+\xi}\right)^2 + \frac{9\left(\frac{r_1}{r_1+1}\right)^2}{4\pi^2\left(\frac{\Delta f_0}{B_{L1}}\right)^2}\left[\frac{1-(r_1+1)\frac{B_{LF}}{B_{L1}}}{(r_1+1)\frac{B_{LF}}{B_{L1}}}\right]\right\}. \tag{155}$$

Letting $r_1 = 2$ and substituting the relation for ξ found in (125), we get

$$a' = -\left\{\frac{4/9}{2\pi^2\left(\frac{\Delta f_0}{B_{L1}}\right)^2}\left[\frac{1 + 1.5\left(\frac{B_{LF}}{B_{L1}}\right)}{3\left(\frac{B_{LF}}{B_{L1}}\right)}\right] + \frac{1}{3}\left(\frac{\frac{3}{8K_c}\ \frac{F_{01}}{B_{L1}T}}{1 + \frac{3}{8K_c}\ \frac{F_{01}}{B_{L1}T}}\right)^2\right\}$$

$$b' = -\frac{2}{27}\left(\frac{\frac{3}{8K_c}\ \frac{F_{01}}{B_{L1}T}}{1 + \frac{3}{8K_c}\ \frac{F_{01}}{B_{L1}T}}\right)\left\{\left(\frac{\frac{3}{8K_c}\ \frac{F_{01}}{B_{L1}T}}{1 + \frac{3}{8K_c}\ \frac{F_{01}}{B_{L1}T}}\right)^2 + \frac{1}{\pi^2\left(\frac{\Delta f_0}{B_{L1}}\right)^2}\left[\frac{1 - 3\left(\frac{B_{LF}}{B_{L1}}\right)}{3\left(\frac{B_{LF}}{B_{L1}}\right)}\right]\right\}. \tag{156}$$

Although it appears from (153) that three solutions exist, in reality only the first, namely $x_1/2\Delta f_0$, results in

$$(1 + \xi)\,\frac{x_1}{2\Delta f_0} - \xi \;>\; 0\,. \tag{157}$$

The inequality of (157) is necessary to insure a real solution for T_{ACQ}, since we observe that the above expression is the argument of the natural logarithm in the first term of (144). Finally, then, solving the first equation in (153) using (154) and (156), we can compute our desired upper bound on T_{ACQ} from [see (144)]:

$$\begin{aligned} B_{L1}\,T'_{ACQ} \;=\; & -\frac{1}{4}\left(\frac{B_{LF}}{B_{L1}}\right)^{-1} \ln\left[\left(1 + \frac{3}{8K_c}\,\frac{F_{01}}{B_{L1}T}\right)\left(\frac{x_1}{2\Delta f_0}\right) - \frac{3}{8K_c}\,\frac{F_{01}}{B_{L1}T}\right] \\ & + 0.75\left\{\frac{9\pi^2}{4}\left(\frac{x_1}{2\Delta f_0}\right)^2\left(\frac{\Delta f_0}{B_{L1}}\right)^2 - \frac{1}{2}\ln\left[3\pi\left(\frac{x_1}{2\Delta f_0}\right)\left(\frac{\Delta f_0}{B_{L1}}\right)\right]\right\}. \end{aligned} \tag{158}$$

As an example of the acquisition time for a GPS receiver, consider the parameters used in the GPSPAC. The data rate is 50 bps and $B_{L1} = 35$ Hz (or $B_{L1}T = 0.7$), $F_{01} = 0.001$, and $r_1 = 2$. For optimum tracking at low ST/N_0, the arm filter bandwidth is $f_cT = 0.415$. Figure 51 illustrates the acquisition time with these parameters with $f_cT = 0.415$ and $f_cT = 10$. From Figure 51, it is seen that there is little difference in the curves for the two values of f_cT, but the region of linearity as indicated by the dashed lines of $\Delta f_{max}/B_{L1}$ is larger for $f_cT = 10$. Also included in Figure 51 is the acquisition time performance of a conventional Costas loop as computed from (133) which assumes $f_c/B_{L1} \gg 10$. The asymptote indicated by $\Delta f_0/B_{L1} = 9.488$ is the pull-in range of the Costas loop determined from (132) at which point the denominator of (133) vanishes and the acquisition time becomes infinite. The acquisition time for the Costas loop and the composite AFC/Costas loop is $T'_{ACQ} = 13.7$ sec and $T'_{ACQ} = 43.4$ msec, respectively, for $\Delta f_0 = \Delta f_{max} = 160$ Hz, $f_c = 500$ Hz, and $B_{L1} = B_{LF} = 35$ Hz. In other words, the composite AFC/Costas loop acquires 316 times faster than the conventional Costas loop. These acquisition times also assume that the conventional Costas loop does not false lock; but, there are false lock points at ±25, ±50, ±100, and ±150 Hz about the carrier frequency for the

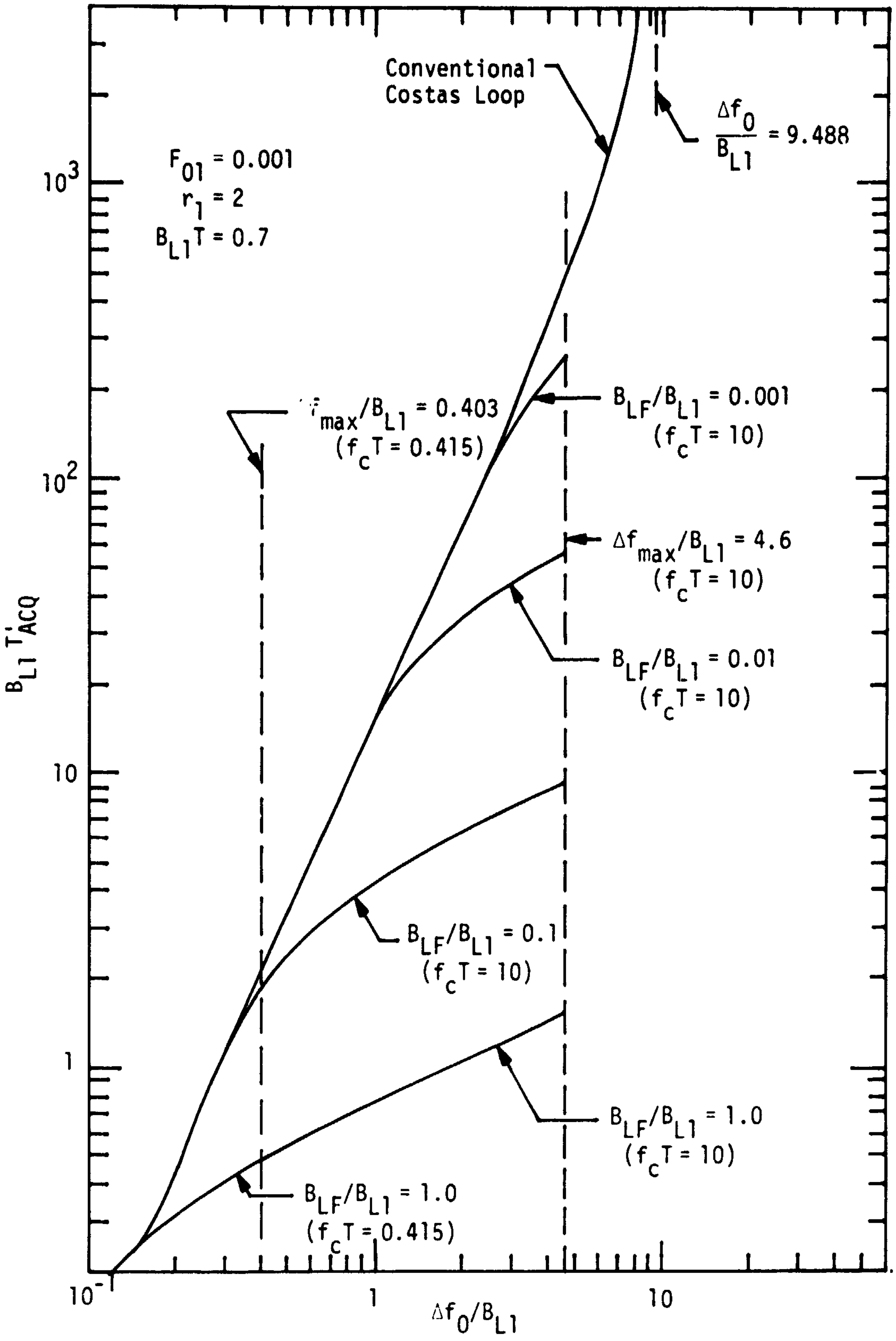

Figure 51. Acquisition Behavior of Composite AFC/Costas Loop ($B_{L1}T = 0.7$)

conventional Costas loop and no false lock points for the composite AFC/Costas loop.

Narrowing the Costas loop bandwidth improves tracking under low dynamic conditions such as the Shuttle/GPS receiver will encounter on-orbit. Figure 52 presents the acquisition time for the AFC/Costas loop with $B_{L1}T = 0.1$ or seven times narrower than in Figure 51. For $\Delta f_{max} = 160$ Hz, the acquisition time of the composite AFC/Costas loop increases by a factor of 430 with $B_{L1} = B_{LF} = 5$ Hz from $T'_{ACQ} = 43.4$ msec with $B_{L1} = B_{LF} = 35$ Hz. In fact, Figure 52 shows that, for $f_cT = 10$, the acquisition time increases exponentially as Δf_0 increases above 3 Hz for $B_{LF} = B_{L1} = 5$ Hz. However, the composite AFC/Costas loop can still acquire at 160 Hz, while the conventional Costas loop can never acquire. If narrower arm filter bandwidths than $f_cT = 10$ are used, then as shown in Figure 52 the acquisition time is decreased within the region of linearity for the narrower bandwidth; but, of course, the acquisition range is decreased.

One final point before leaving the discussion of acquisition performance regards verification of the assumption made just prior to (142), allowing use of this simplified acquisition time formula rather than (133) in deriving the bound on acquisition time. The assumption made was that the solution found for the value of Δf_1 which minimized T'_{ACQ} would satisfy

$$\Delta f_1 \ll \frac{B_{L1}}{\pi}\left(\frac{r_1}{r_1+1}\right)\sqrt{\frac{2}{F_{01}} - 1} \tag{159}$$

or, equivalently,

$$\left(\frac{x_1}{2\Delta f_0}\right)\left(\frac{\Delta f_0}{B_{L1}}\right) \ll \frac{1}{\pi}\left(\frac{r_1}{r_1+1}\right)\sqrt{\frac{2}{F_{01}} - 1} \; . \tag{160}$$

Using $x_1/(2\Delta f_0)$ as determined from (153), Figure 53 plots the left-hand side of (160) versus $\Delta f_0/B_{L1}$ for $r_1 = 2$ and $F_{01} = 0.001$. For these parameter values, the right-hand side of (160) equals 9.488. Since the denominator of (133) is computed as one minus the square of the ratio of the left-hand to right-hand side of (160), we observe from Figure 53 that this correction factor is well within our approximation over most values of frequency offset within the acquisition range.

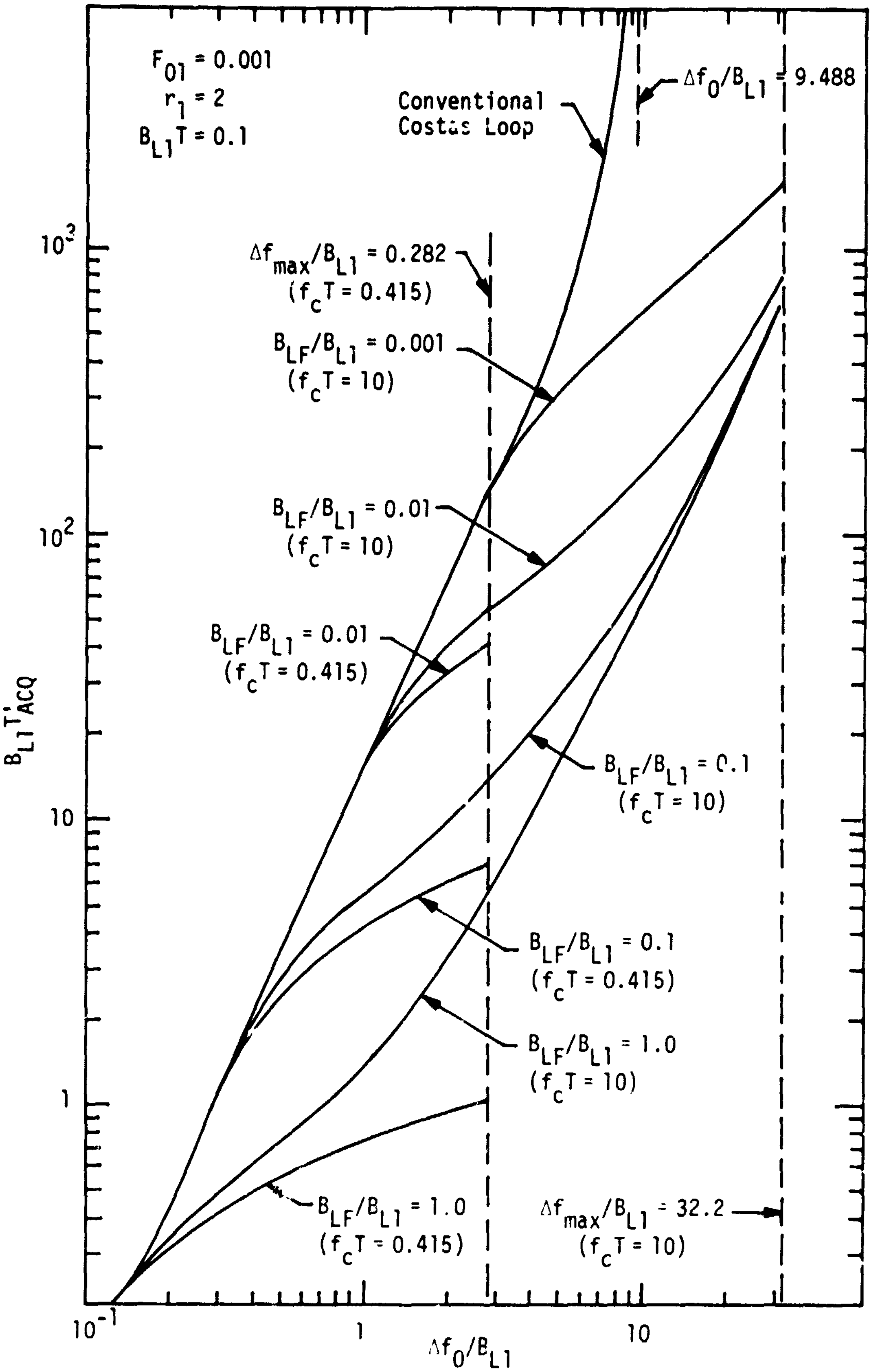

Figure 52. Acquisition Behavior of Composite AFC/Costas Loop ($B_{L1}T = 0.1$)

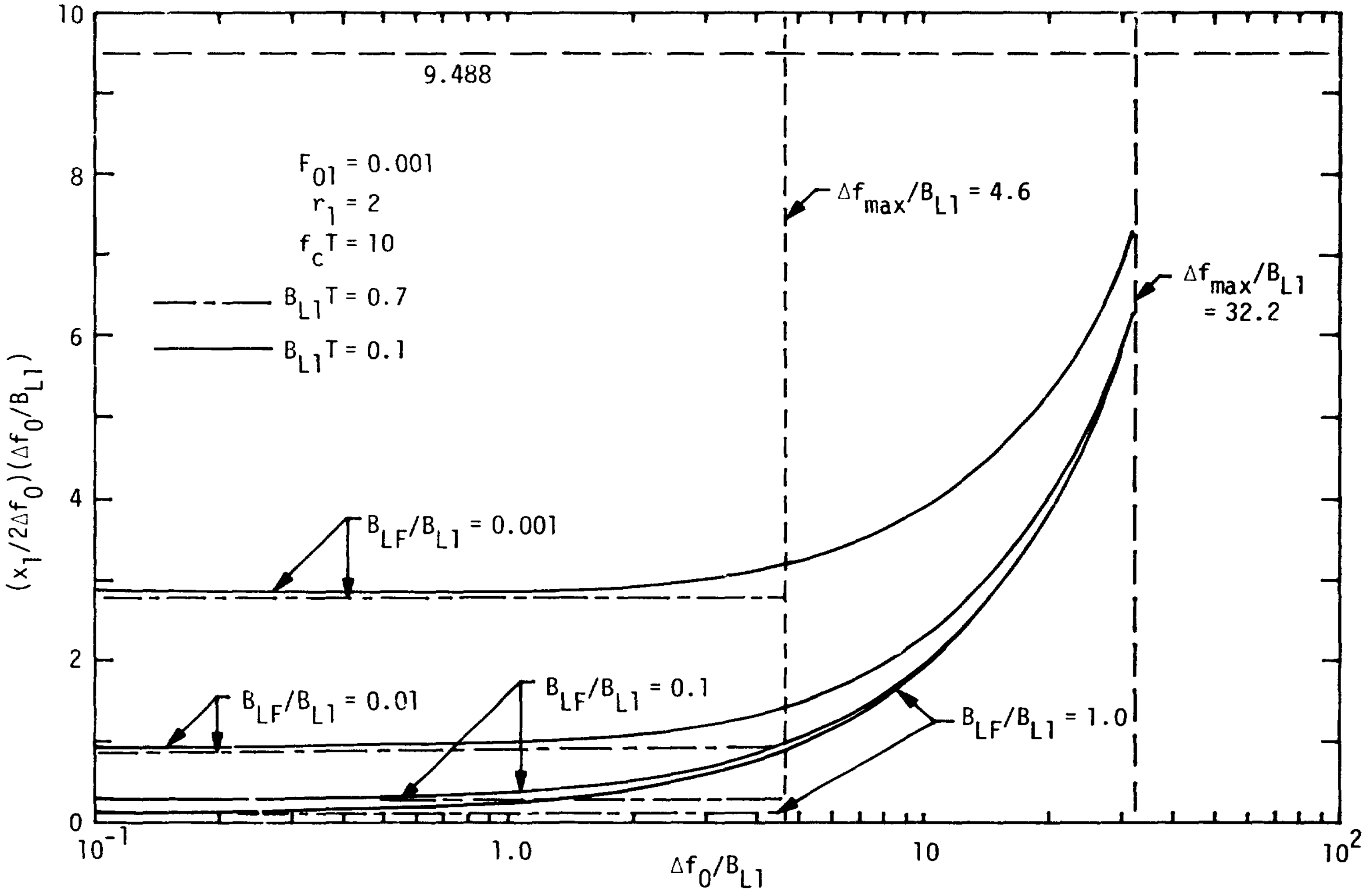

Figure 53. Check on Validity of Using Simplified Formula for Calculation of Costas Loop Acquisition Time

7.4 Tracking Performance of Composite AFC/Costas Loop

When separate loop filters are employed for the AFC and Costas loops as in Figure 46, the equivalent additive Costas loop noise and AFC error signal (which acts like additive noise when the loop is locked) are processed by different closed loop transfer functions insofar as evaluating phase tracking jitter. To see this, we begin by relating the VCO output phase to its two input signal components, i.e.,

$$\hat{\theta}(t) = \frac{K_V}{p}\left[F_1(p)\, z_0(t) + F_2(p)\, w_0(t)\right], \tag{161}$$

where $z_0(t)$ and $w_0(t)$ are given by

$$\begin{aligned} z_0(t) = {} & \frac{K_1^2 K_m^2}{2}\left\{\left[\sqrt{S}\,\hat{m}(t) - \hat{N}_s(t)\right]^2 - \hat{N}_c^2(t)\right\} \sin 2\phi(t) \\ & + K_1^2 K_m^2 \hat{N}_c(t)\left[\sqrt{S}\,\hat{m}(t) - \hat{N}_s(t)\right] \cos 2\phi(t) \end{aligned} \tag{162}$$

and

$$w_0(t) = K_1^2 K_m^2 \left\{N_c(t)\left[\sqrt{S}\,\hat{m}(t) - \hat{N}_s(t)\right] - \hat{N}_c(t)\left[\sqrt{S}\, m(t) - N_s(t)\right]\right\} \tag{163}$$

where the additive channel noise is expressed in the form of a narrowband process about the actual frequency of the observed data, viz.,

$$n_i(t) = \sqrt{2}\left\{N_c(t) \cos\left[\omega_0 t + \theta(t)\right] - N_s(t) \sin\left[\omega_0 t + \theta(t)\right]\right\}. \tag{164}$$

The narrowband processes $N_c(t)$ and $N_s(t)$ are statistically independent, stationary, white Gaussian noise processes with single-sided noise spectral density N_0 W/Hz. The narrowband processes $\hat{N}_c(t)$ and $\hat{N}_s(t)$ in (162) and (163) are $N_c(t)$ and $N_s(t)$ passed through the lowpass arm filter G(s), respectively. Alternately separating $z_0(t)$ into its signal and noise components, we can rewrite (161) as

$$\hat{\theta}(t) = \frac{K_V K_1^2 K_m^2}{p}\left\{F_1(p)\left[S\hat{m}^2(t)\,\frac{\sin 2\phi}{2} + \frac{1}{2}\, v_2(t,2\phi)\right] + F_2(p)\,\frac{1}{2}\, w(t)\right\}, \tag{165}$$

where

$$v_2(t,2\phi) \triangleq [-\hat{N}_c^2(t) + \hat{N}_s^2(t) - 2\sqrt{S}\,\hat{m}(t)\hat{N}_s(t)]\sin 2\phi + [2\sqrt{S}\,\hat{m}(t)\hat{N}_c(t) - 2\hat{N}_c(t)\hat{N}_s(t)]\cos 2\phi \qquad (166)$$

and

$$w(t) \triangleq 2w_0(t) = 2\sqrt{S}\,\hat{m}(t)N_c(t) - 2N_c(t)\hat{N}_s(t) - 2\sqrt{S}\,m(t)\hat{N}_c(t) - 2\hat{N}_c(t)N_s(t) \; . \qquad (167)$$

Then, letting $K \triangleq K_V K_1^2 K_m^2$, replacing $\hat{m}^2(t)$ by $D_m \triangleq \langle\overline{m^2(t)}\rangle$, and ignoring the self-noise of the modulation, we get

$$2\hat{\theta}(t) = \frac{K}{p}\{F_1(p)[S D_m \sin 2\phi(t) + v_2(t,2\phi)] + F_2(p)w(t)\} \; . \qquad (168)$$

Finally, letting $\phi_2(t) \triangleq 2\phi(t) = 2[\theta(t) - \hat{\theta}(t)] \triangleq \theta_2(t) - \hat{\theta}_2(t)$ and taking the linearized case, i.e., $\sin 2\phi(t) \cong 2\phi(t)$, gives the desired differential equation of loop operation, viz.,

$$\phi_2(t) = \theta_2(t) - \frac{K}{p}F_1(p)S D_m \phi_2(t) + \frac{K}{p}F_1(p)\,v_2(t,\phi_2) + \frac{K}{p}F_2(p)w(t) \qquad (169)$$

or

$$\phi_2(t) = \frac{p}{p + S D_m K F_1(p)}\theta_2(t) + \frac{S D_m K F_1(p)}{p + S D_m K F_1(p)}\frac{v_2(t,\phi_2)}{S D_m} + \frac{S D_m K F_2(p)}{p + S D_m K F_1(p)}\frac{w(t)}{S D_m} \; . \qquad (170)$$

Defining, as is done for conventional Costas loops, the closed loop transfer function,

$$H_1(p) = \frac{S D_m K F_1(p)}{p + S D_m K F_1(p)} \; , \qquad (171)$$

equation (170) simplifies to

$$\phi_2(t) = [1 - H_1(p)]\,\theta_2(t) + H_1(p)\,\frac{v_2(t,\phi_2)}{S\,D_m} + \left[H_1(p)\,\frac{F_2(p)}{F_1(p)}\right]\frac{w(t)}{S\,D_m}$$

$$= [1 - H(p)]\,\theta_2(t) + N_e(t)\,, \qquad (172)$$

where $N_e(t)$ is the total equivalent noise and, as predicted, is composed of the sum of the additive Costas loop noise $v_2(t,2\phi)$ and AFC error signal w(t), each processed by different closed loop transfer functions. To evaluate the tracking performance of the composite loop, we must find the spectral density of $N_e(t)$.

From the definition of $N_e(t)$ given in (172), we see by inspection that its power spectral density $S_{N_e}(\omega)$ is given by

$$S_{N_e}(\omega) = \frac{1}{(S\,D_m)^2}\left|H_1(j\omega)\right|^2 S_{v_2}(\omega) + \frac{1}{(S\,D_m)^2}\left|H_1(j\omega)\right|^2 \left|\frac{F_2(j\omega)}{F_1(j\omega)}\right|^2 S_w(\omega)$$

$$+ \left(\frac{1}{S\,D_m}\right)^2 \left|H_1(j\omega)\right|^2 \frac{F_2(j\omega)}{F_1(j\omega)}\,S_{v_2w}(\omega) + \left(\frac{1}{S\,D_m}\right)^2 \left|H_1(j\omega)\right|^2 \frac{F_2{}^*(j\omega)}{F_1{}^*(j\omega)}\,S_{wv_2}(\omega)$$

$$(173)$$

where the asterisk denotes complex conjugate, $S_{v_2}(\omega)$ and $S_w(\omega)$ are the power spectral densities of $v_2(t,\phi_2)$ and w(t), respectively, and $S_{v_2w}(\omega)$ and $S_{wv_2}(\omega)$ are the corresponding cross-spectral densities. Since the bandwidth of the Costas loop is ordinarily designed to be narrow with respect to the equivalent noise bandwidth of $v_2(t,\phi_2)$ and likewise for the AFC loop with respect to w(t), we can approximate $v_2(t,\phi_2)$ and w(t) as delta-correlated processes with power spectral densities $S_{v_2}(0)$ and $S_w(0)$, and cross-spectral densities $S_{v_2w}(0)$ and $S_{wv_2}(0)$. From [8],

$$S_{v_2}(0) = 4\,S\left(\frac{N_0}{2}\right)\int_{-\infty}^{\infty} S_m(\omega)\,|G(j\omega)|^4\,\frac{d\omega}{2\pi} + 4\left(\frac{N_0}{2}\right)^2\int_{-\infty}^{\infty} |G(j\omega)|^4\,\frac{d\omega}{2\pi}\,. \qquad (174)$$

Similarly, from the definition of w(t) in (167), we find after some algebraic manipulation that

$$S_w(0) = 16\,S\left(\frac{N_0}{2}\right)\int_{-\infty}^{\infty} S_m(\omega)\,[\mathrm{Im}\,\{G(j\omega)\}]^2\,\frac{d\omega}{2\pi}$$

$$+\,16\left(\frac{N_0}{2}\right)^2\int_{-\infty}^{\infty}[\mathrm{Im}\,\{G(j\omega)\}]^2\,\frac{d\omega}{2\pi}$$

$$S_{v_2w}(0) = S_{wv_2}(0) = 0\,. \qquad (175)$$

Thus, substituting (174) and (175) into (173), we get

$$S_{N_e}(\omega) = \frac{1}{(S\,D_m)^2}\,|H_1(j\omega)|^2\,[2\,S\,N_0\,D_m\,K_D + N_0^2\,B_i\,K_L]$$

$$+\,\frac{1}{(S\,D_m)^2}\,|H_1(j\omega)|^2\left|\frac{F_2(j\omega)}{F_1(j\omega)}\right|^2[2\,S\,N_0\,D_m\,\mathcal{K}_D + N_0^2\,B_i\,\mathcal{K}_L]\,, \qquad (176)$$

where

$$K_D = \frac{\int_{-\infty}^{\infty} S_m(\omega)\,|G(j\omega)|^4\,\frac{d\omega}{2\pi}}{\int_{-\infty}^{\infty} S_m(\omega)\,|G(j\omega)|^2\,\frac{d\omega}{2\pi}}\;; \qquad \mathcal{K}_D = \frac{\int_{-\infty}^{\infty} S_m(\omega)\,[\mathrm{Im}\,\{G(j\omega)\}]^2\,\frac{d\omega}{2\pi}}{\int_{-\infty}^{\infty} S_m(\omega)\,|G(j\omega)|^2\,\frac{d\omega}{2\pi}}$$

$$K_L = \frac{\int_{-\infty}^{\infty} |G(j\omega)|^4\,\frac{d\omega}{2\pi}}{\int_{-\infty}^{\infty} |G(j\omega)|^2\,\frac{d\omega}{2\pi}}\;; \qquad \mathcal{K}_L = \frac{\int_{-\infty}^{\infty} [\mathrm{Im}\,\{G(j\omega)\}]^2\,\frac{d\omega}{2\pi}}{\int_{-\infty}^{\infty} |G(j\omega)|^2\,\frac{d\omega}{2\pi}}$$

$$D_m = \int_{-\infty}^{\infty} S_m(\omega)\,|G(j\omega)|^2\,\frac{d\omega}{2\pi}\;; \qquad B_i = \int_{-\infty}^{\infty} |G(j\omega)|^2\,\frac{d\omega}{2\pi}\,. \qquad (177)$$

The total equivalent noise power, $\sigma_{N_e}^2$, can now be obtained by integrating (176) between $-\infty$ and ∞, viz.,

$$\sigma_{N_e}^2 \triangleq \int_{-\infty}^{\infty} S_{N_e}(\omega)\,\frac{d\omega}{2\pi} = \frac{1}{(S\,D_m)^2}[2\,S\,N_0\,D_m\,K_D + N_0^2\,B_i\,K_L]\int_{-\infty}^{\infty}|H_1(j\omega)|^2\,\frac{d\omega}{2\pi}$$

$$+\,\frac{4}{(S\,D_m)^2}[2\,S\,N_0\,D_m\,\mathcal{K}_D + N_0^2\,B_i\,\mathcal{K}_L]\int_{-\infty}^{\infty}|H_1(j\omega)|^2\left|\frac{F_2(j\omega)}{F_1(j\omega)}\right|^2\frac{d\omega}{2\pi}\,. \qquad (178)$$

The first integral in (178) is the well-known relation for loop bandwidth of a second-order Costas loop, i.e.,

$$\int_{-\infty}^{\infty} |H_1(j\omega)|^2 \frac{d\omega}{2\pi} = 2B_{L1} \cong \frac{r_1+1}{2\tau_{21}} . \tag{179}$$

The second integral in (178) is evaluated as follows. Define

$$\begin{aligned} I_3 &\triangleq \int_{-\infty}^{\infty} |H_1(j\omega)|^2 \left|\frac{F_2(j\omega)}{F_1(j\omega)}\right|^2 \frac{d\omega}{2\pi} \\ &= \frac{1}{2\pi j}\int_{-\infty}^{\infty} A_3(s)\,A_3(-s)\,ds , \end{aligned} \tag{180}$$

where

$$\begin{aligned} A_3(s) &\triangleq H_1(s)\,\frac{F_2(s)}{F_1(s)} \\ &= \frac{S D_m K + s[S D_m K(\tau_{22}+\tau_{11})] + s^2 S D_m K \tau_{11}\tau_{22}}{S D_m K + s[S D_m K(\tau_{21}+\tau_{12})+1] + s^2[\tau_{11}+\tau_{12}(S D_m K \tau_{21}+1)] + s^3 \tau_{12}\tau_{11}} \\ &= \frac{c_0 + c_1 s + c_2 s^2}{d_0 + d_1 s + d_2 s^2 + d_3 s^3} . \end{aligned} \tag{181}$$

Integrals of the type given in (180) have been previously tabulated (see for example, [7], p. 135, Table 4-1). When the denominator of $A_n(s)$ is a third-order polynomial, i.e., $n=3$, then the result is

$$I_3 = \frac{c_2^2 d_0 d_1 + (c_1^2 - 2c_0c_2)d_0d_3 + c_0^2 d_2 d_3}{2d_0d_3(d_1d_2 - d_0d_3)} . \tag{182}$$

Substituting (181) into (182), one obtains after considerable simplification

$$I_3 \triangleq 2B_{L12} = \left(\frac{F_{02}}{F_{01}}\right)^2 \frac{r_1 + \left(\frac{\tau_{21}}{\tau_{22}}\right)^2}{2\tau_{21}} , \tag{183}$$

where we have made only the assumption that $F_{01}, F_{02} << 1$. Further relating B_{L12} to the bandwidth B_{L1} of the Costas loop alone by

$$B_{L12} = \gamma_B B_{L1} , \tag{184}$$

one can show, using (104), (108), (111), (117), (128), and (183), that

$$\gamma_B = \frac{r_2\left(\frac{B_{LF}}{B_{L1}}\right)}{\left(\frac{r_1}{r_1+1}\right)^2\left[K_c B_{L1} T + \frac{F_{01}(r_1+1)}{4r_1}\right]}\left\{\left(\frac{r_1}{r_1+1}\right) + \frac{\left(\frac{r_1+1}{4r_2}\right)\left(\frac{B_{LF}}{B_{L1}}\right)}{K_c B_{L1} T + \frac{F_{01}(r_1+1)}{4r_1}}\right\}$$

$$\cong \frac{\frac{(r_1+1)}{4}\left(\frac{B_{LF}}{B_{L1}}\right)^2}{\left(\frac{r_1}{r_1+1}\right)^2\left\{K_c B_{L1} T\left[1 + \frac{F_{01}(r_1+1)}{4r_1 K_c B_{L1} T}\right]\right\}^2} . \tag{185}$$

Thus, for $r_1 = 2$, (185) reduces to

$$\gamma_B = \frac{12\left(\frac{B_{LF}}{B_{L1}}\right)^2}{\left[\frac{8K_c B_{L1} T}{3}(1+\xi)\right]^2} \tag{186}$$

where ξ is defined in (125). Figure 54 illustrates the bandwidth ratio γ_B as computed from (186) versus B_{LF}/B_{L1} for $F_{01} = 0.001$, $B_{L1}T = 0.7$, 0.1, and $f_c T = 0.415$, 10.

Finally, combining (178), (179), (183), and (184), the total equivalent noise power, which is identical to the mean-square phase tracking jitter $\sigma_{\phi_2}^2$, is given by

$$\sigma_{\phi_2}^2 = \frac{4}{\rho \mathcal{S}_{L_1}} + \frac{4}{\rho \mathcal{S}_{L_2}}$$

$$= \sigma_1^2 + \sigma_2^2 , \tag{187}$$

where

$$\rho = \frac{S}{N_0 B_{L1}}$$

is the signal-to-noise ratio of an equivalent linear loop, e.g., a phase-locked loop, having a bandwidth equal to that of the Costas loop, $\mathcal{S}_{L_1}$ is

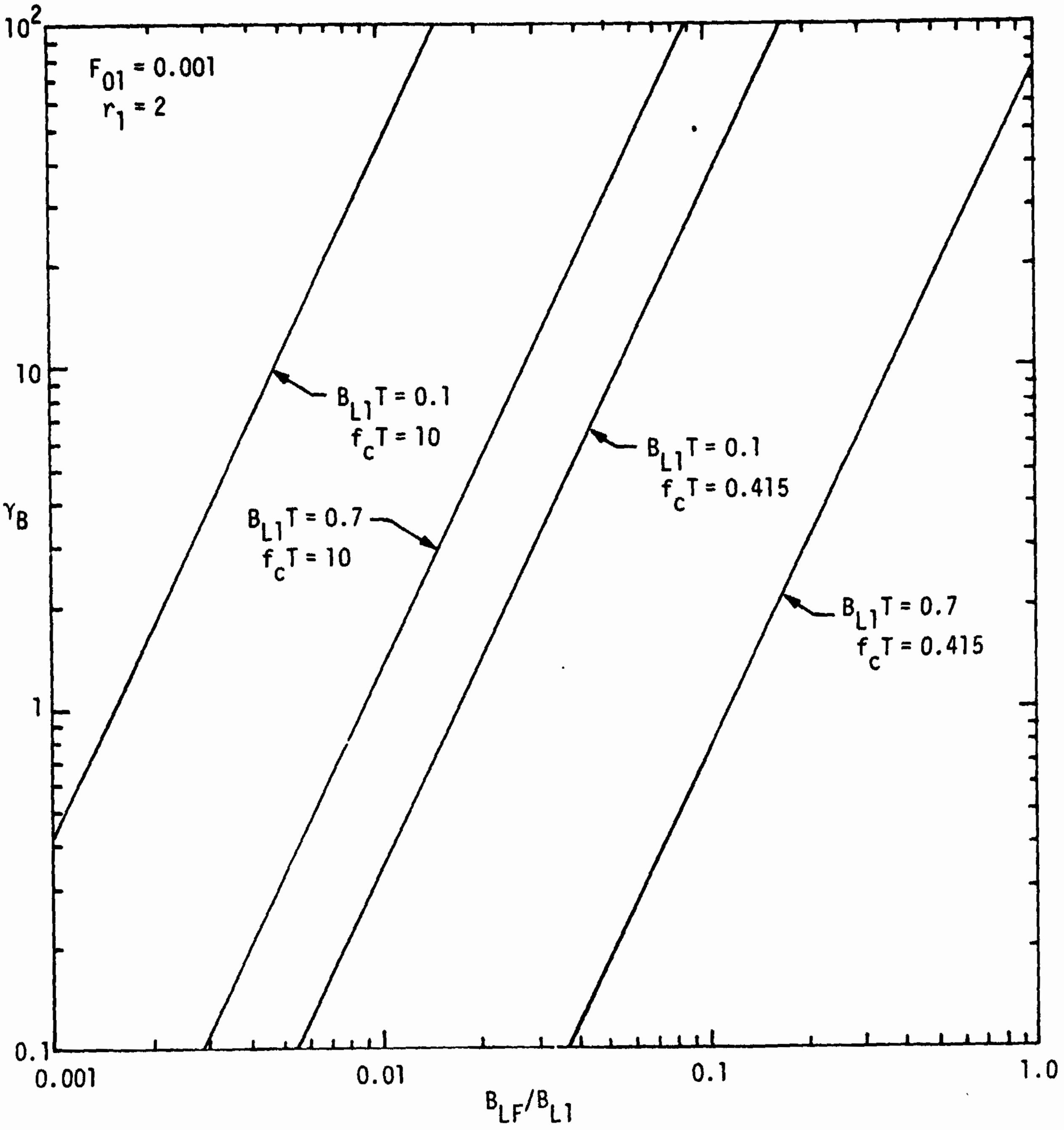

Figure 54. Bandwidth Ratio γ_B Versus the Ratio of AFC to Costas Loop Bandwidth

the familiar squaring loss of the Costas loop, namely,

$$\mathcal{S}_{L_1} = \frac{D_m}{K_D + \frac{K_L}{\rho_i D_m}} \tag{188}$$

and $\mathcal{S}_{L_2}$ is the squaring loss of the AFC loop which is defined by

$$\mathcal{S}_{L_2} = \frac{D_m}{4\gamma_B \left[\mathcal{K}_D + \frac{\mathcal{K}_L}{\rho_i D_m}\right]} . \tag{189}$$

In (188) and (189), $\rho_i \triangleq 2S/N_0B_i$ is the signal-to-noise ratio in the arm filter bandwidth. For a single-pole RC arm filter as in Figure 46,

$$K_L = \mathcal{K}_L = \frac{1}{2} . \tag{190}$$

Furthermore, for NRZ data, K_D and $\mathcal{K}_D$ defined in (177) can be evaluated as

$$K_D = \frac{1 - \frac{3-(3+\omega_cT)\,e^{-\omega_cT}}{2\omega_cT}}{1 - \frac{1}{\omega_cT}\left[1 - e^{-\omega_cT}\right]} \tag{191}$$

and

$$\mathcal{K}_D = \frac{\frac{1}{\omega_cT}\left[1 - (1+\omega_cT)\,e^{-\omega_cT}\right]}{1 - \frac{1}{\omega_cT}\left[1 - e^{-\omega_cT}\right]} . \tag{192}$$

Figure 55 illustrates D_m, K_D, and $\mathcal{K}_D$ as defined in (109), (191) and (192) versus $f_cT = \omega_cT/2\pi$. At $f_cT = 0.415$, (191) and (192) are evaluated as $K_D = 0.782$ and $\mathcal{K}_D = 0.437$. Also, from (109), $D_m = 0.645$. Similarly, at $f_cT = 10$, then $K_D = 0.992$, $\mathcal{K}_D = 0.0162$, and $D_m = 0.984$. Thus, the component of phase tracking jitter due to the Costas loop for $f_cT = 0.415$ is given by

$$\sigma_1^2 = \frac{4N_0B_{L1}}{S}\left[\frac{0.782 + \frac{0.775}{\rho_i}}{0.645}\right] \tag{193}$$

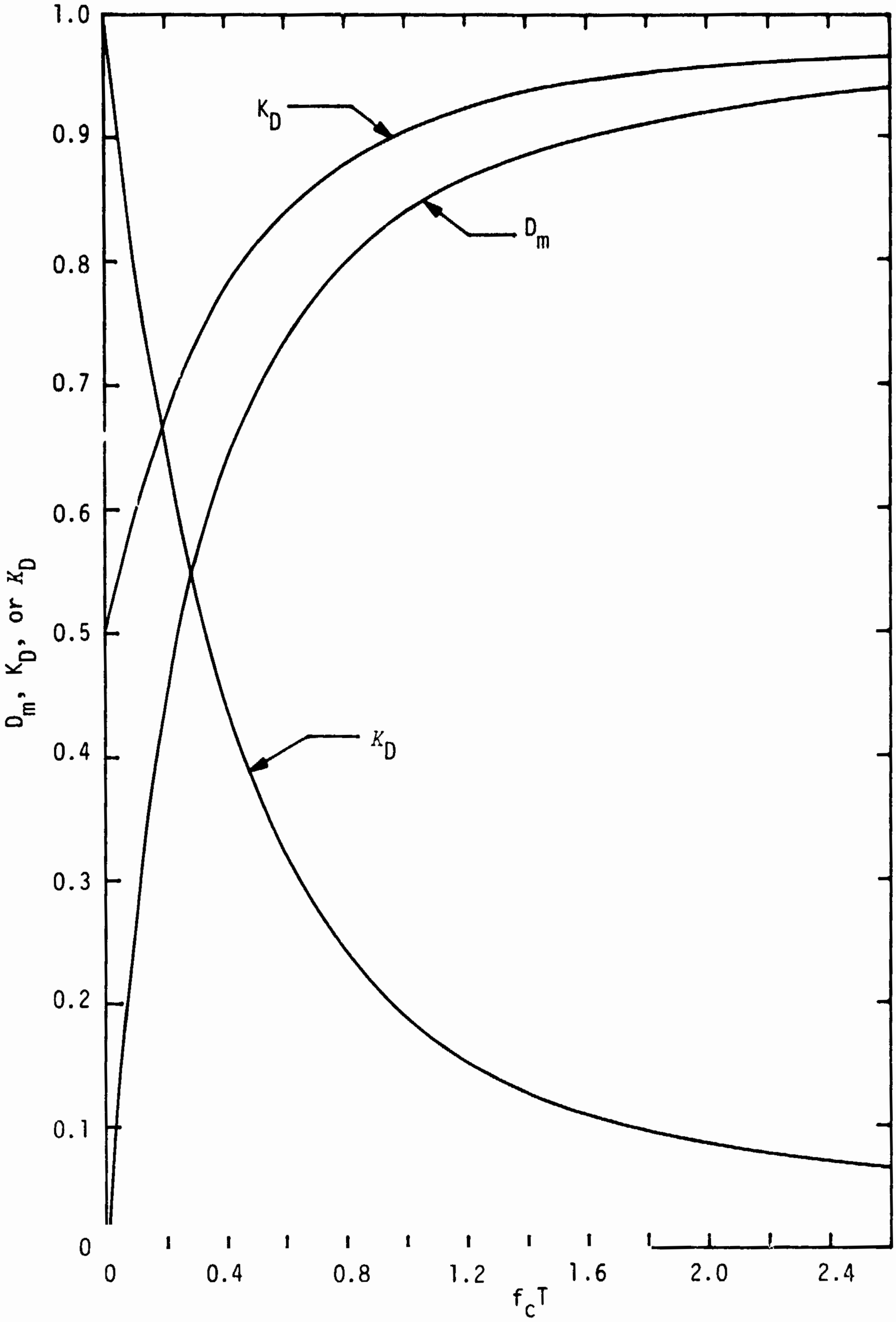

Figure 55. Parameters D_m, K_D, and $\mathcal{K}_D$ Versus f_cT for an RC Arm Filter and NRZ Data

and for $f_cT = 10$,

$$\sigma_1^2 = \frac{4N_0B_{L1}}{S}\left[\frac{0.992 + \dfrac{0.508}{\rho_i}}{0.984}\right] . \qquad (194)$$

Since for a single-pole RC filter, $B_i = \omega_c/2$, we can express ρ_i as

$$\rho_i \triangleq \frac{S}{N_0B_i} = \frac{S}{N_0B_{L1}}(B_{L1}T)\frac{1}{B_iT}$$

$$= \frac{S}{N_0B_{L1}}(B_{L1}T)\frac{2}{\omega_cT} . \qquad (195)$$

Thus, (193) can be rewritten as

$$\sigma_1^2 = \frac{4N_0B_{L1}}{S}\left[1.212 + 1.567\left(\frac{N_0B_{L1}}{S}\right)\left(\frac{1}{B_{L1}T}\right)\right], \qquad (196)$$

and (194) can be rewritten as

$$\sigma_1^2 = \frac{4N_0B_{L1}}{S}\left[1.008 + 16.223\left(\frac{N_0B_{L1}}{S}\right)\left(\frac{1}{B_{L1}T}\right)\right]. \qquad (197)$$

Similarly, the AFC loop component of phase tracking jitter for $f_cT = 0.415$ is given by

$$\sigma_2^2 = \frac{4N_0B_{L1}}{S}\left[0.678 + 1.567\left(\frac{N_0B_{L1}}{S}\right)\left(\frac{1}{B_{L1}T}\right)\right]\left\{\frac{48\left(\dfrac{B_{LF}}{B_{L1}}\right)^2}{\left[\dfrac{B_{L1}T}{1.736}\left(1 + \dfrac{1.736\,F_{01}}{B_{L1}T}\right)\right]^2}\right\} \qquad (198)$$

and for $f_cT = 10$,

$$\sigma_2^2 = \frac{4N_0B_{L1}}{S}\left[0.0165 + 16.223\left(\frac{N_0B_{L1}}{S}\right)\left(\frac{1}{B_{L1}T}\right)\right]\left\{\frac{48\left(\dfrac{B_{LF}}{B_{L1}}\right)^2}{\left[\dfrac{B_{L1}T}{23.95}\left(1 + \dfrac{23.95\,F_{01}}{B_{L1}T}\right)\right]^2}\right\} .$$

(199)

Figures 56 and 57 illustrate the rms phase tracking jitter $\sigma_{\phi 2}$ as computed from (196) - (199) and (187) versus ST/N_0 (E_b/N_0) in dB for $F_{01} = 0.001$, $r_1 = 2$, and $B_{L1}T = 0.7$, 0.1, respectively. The parameter in both figures is the ratio of AFC to Costas loop bandwidth for $f_cT = 0.415$ and $f_cT = 10$. Acquisition may take place if $\sigma_{\phi 2} \leq 1.0$ radian. The tracking requirement for the Shuttle/GPS is $\sigma_{\phi 2} = 0.524$ radian. In Figure 56, the composite AFC/Costas loop tracking performance is the same as the conventional Costas loop when $B_{LF}/B_{L1} \leq 0.01$ for $f_cT = 0.415$ and when $B_{LF}/B_{L1} \leq 0.001$ for $f_cT = 10$. In Figure 47, the composite AFC/Costas loop tracking performance is the same as the conventional Costas loop when $B_{LF}/B_{L1} \leq 0.001$ for $f_cT = 0.415$ and when $B_{LF}/B_{L1} \leq 10^{-4}$ for $f_cT = 10$. Comparing Figures 56 and 57 with Figures 51 and 52, one immediately observes the trade-off between acquisition and tracking performance of the composite loop as the B_{LF}/B_{L1} bandwidth ratio is varied. Alternately, after acquisition, the AFC discriminator input to the VCO can be switched off and the Costas loop arm filter and loop filter bandwidths can be readjusted for tracking. In this case, with a little more complexity, the acquisition and tracking performance can be optimized separately. In fact, many GPS user sets do switch the AFC loop off and change the filter bandwidths for tracking.

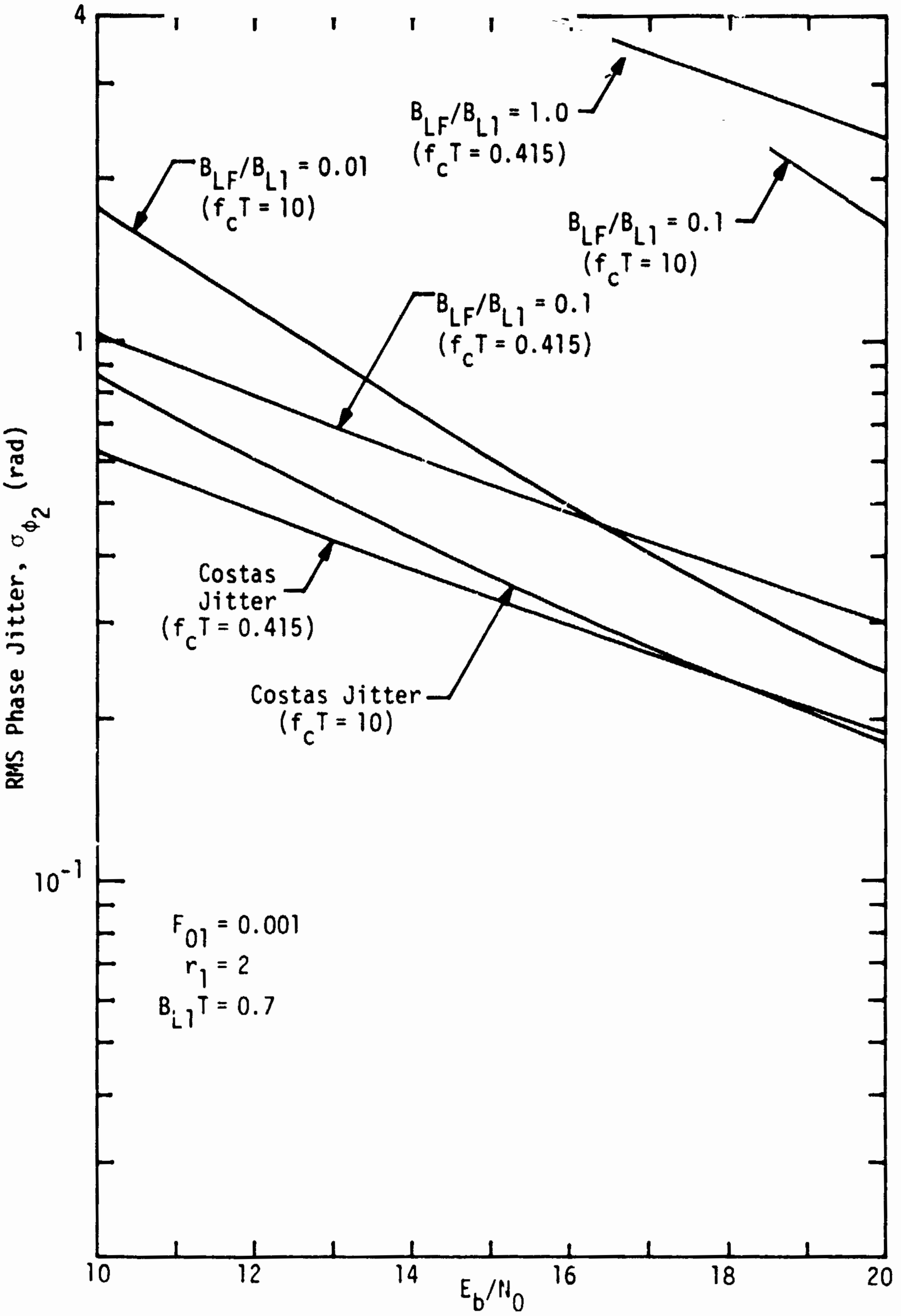

Figure 56. Tracking Jitter Performance for Composite AFC/Costas Loop ($B_{L1}T = 0.7$)

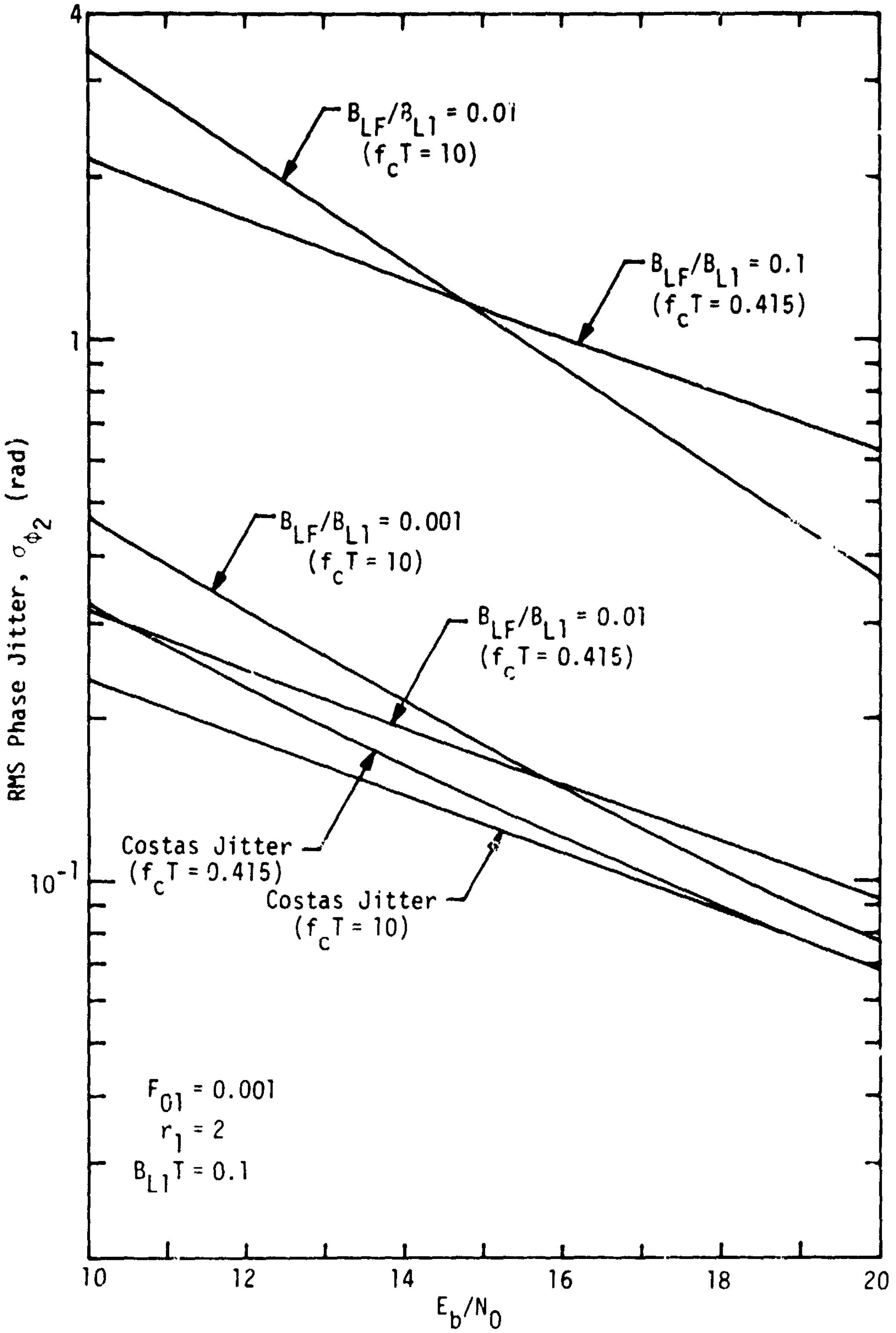

Figure 57. Tracking Jitter Performance for Composite AFC/Costas Loop ($B_{L1}T = 0.1$)

8.0 GPS RECEIVER CLOCK MODEL

8.1 Introduction

Oscillators used for timing in the GPS user set and satellite are characterized by long-term instability and short-term instability. Long-term instability is based on measurement intervals of hours or days or longer; short-term instability is based on measurement intervals of minutes or seconds or shorter. Short-term instability accounts for the random and relatively rapid frequency (or phase) fluctuations that occur. Long-term instability accounts for the constant frequency error and relatively slow frequency drifts that occur due to aging. This section provides the quantitative characterization of oscillator stability that is necessary for specifying the Shuttle GPS receiver oscillator.

9.2 Technical Discussion

A typical sample function of the radian frequency process of an oscillator is illustrated in Figure 58. For a square clock signal, the oscillator outputs $s\big(t,\Phi(t)\big)$ can be represented as

$$s\big(t,\Phi(t)\big) = \sin \Phi(t)$$

where

$$\dot{\Phi}(t) = \omega_0 + \Omega t + \dot{\psi}(t)$$

and ω_0 = frequency if the oscillator were perfect

Ωt = drift or long-term component

$\dot{\psi}(t)$ = short-term component or phase noise.

Thus,

$$\Phi(t) \triangleq \int_{t_0}^{t} \dot{\Phi}(\lambda)\, d\lambda$$

$$= \omega_0(t - t_0) + \Omega(t - t_0)^2 + \psi(t) - \psi(t_0)$$

characterizes the instantaneous phase accumulations. Figure 59 shows a typical aging curve for a fairly good quartz crystal oscillator. Least squares fits of the straight lines to the two parts of Figure yield aging rates of 0.536×10^{-10} per day and 0.515×10^{-10} per day, respectively.

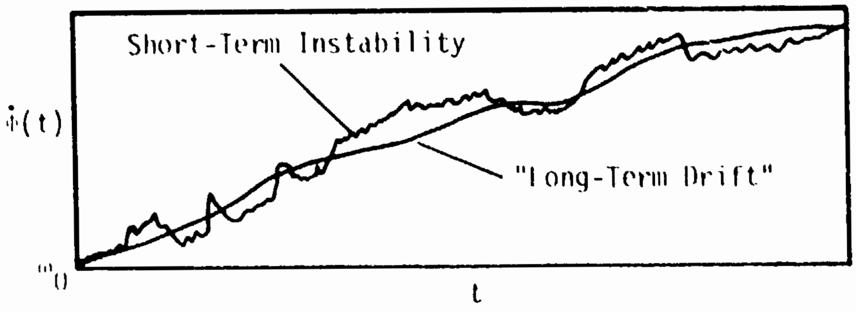

Figure 58. Typical Instantaneous Frequency Fluctuations of an Oscillator

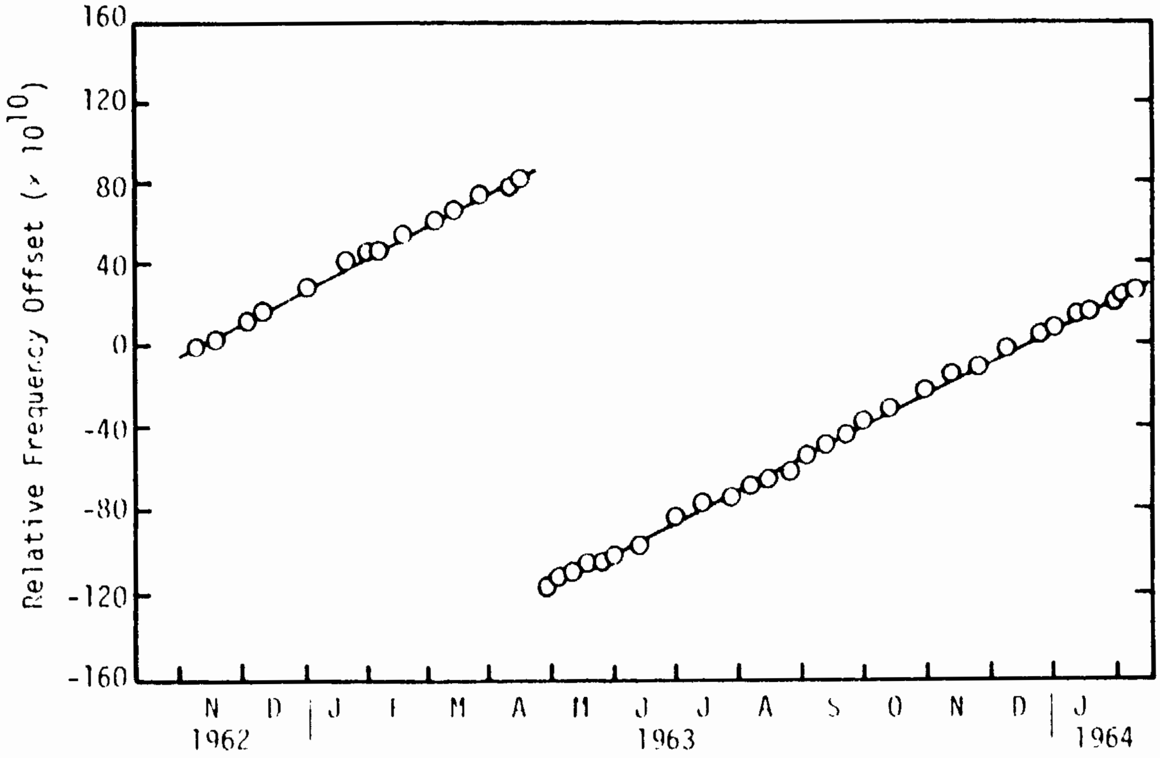

Figure 59. Frequency Aging of a Good Quartz Crystal Oscillator (taken from J. A. Barnes, Proceedings of the IEEE, February 1966)

For the GPS clocks, both settability error and long-term drift contribute to the long-term elapsed time error. Settability is defined as the precision to which two clock standards can be set to the same frequency. Just how accurately two clocks can be set to the same initial frequency is determined by F, the fractional frequency offset coefficient. The accumulated time error ΔT_s due to settability is given by

$$\Delta T_s = 8.64 \times 10^{10}\ FT,$$

where ΔT_s is in microseconds, F is less than 10^{-7} but greater than 10^{-13} in parts per 10^{-x} per day, and T is the elapsed time in days.

Long-term drift arises from slow changes in the average frequency of the clock due to changes in the clock resonator. The accumulated time error due to long-term instability is

$$\Delta T_L = 4.32 \times 10^{10}\ F'T^2,$$

where ΔT_L is in microseconds, $F' = \Omega/2\pi$ and is less than 10^{-7} but greater than 10^{-13} in parts per 10^{-x} per day, and T is the elapsed time in days. The total accumulated time error after T days is

$$\Delta T = 8.64 \times 10^{10}\ FT + 4.32 \times 10^{10}\ F'T^2.$$

Table 21 summarizes the characteristics of several oscillators that are used as clocks. The frequency-time standards are usually of 1 MHz, 5 MHz or 10 MHz. The oscillator used by the GPS satellites is the Efratom Rubidium 10 MHz with characteristics shown in Table .

The short-term instability is of more interest in the use of the GPS than long-term instability because the operation of calculating pseudo range and other processes of time in the navigation filter are on the order of 0.1 second to a few seconds. Therefore, $\dot{\psi}(t)$ must also be considered. In general, the radian frequency is characterized by

$$\dot{\psi}(t) = \alpha + \dot{\phi}(t)$$

with α an independent random variable and $\dot{\phi}(t)$ a zero mean stationary random process. The phase accumulated in τ seconds is

$$\psi(t+\tau) - \psi(t) = \alpha\tau + \phi(t+\tau) - \phi(t)$$

Table 21. Characteristics of Precision-Time Standards

Manufacturer	Type	Long-Term Instability (days)	Short-Term Stability			Settability
			0.1 sec	1 sec	10 sec	
Frequency Electronics	Quartz TCXO 5 MHz	7×10^{-7}	5×10^{-10}	----	----	1×10^{-7}
Bliley-OSC Cox-Oven LLI & T	Quartz OCXO 5 MHz	1×10^{-10}	5×10^{-12}	5×10^{-12}	----	1×10^{-11}
Frequency Electronics	Quartz OCXO 5 MHz	2×10^{-11}	9×10^{-12}	8×10^{-13}	----	5×10^{-12}
Efratom	Rubidium 10 MHz	1×10^{-12}	----	2×10^{-11}	5×10^{-12}	1×10^{-12}
Hewlett-Packard	Cesium 5 MHz, 1 MHz	----	----	7×10^{-11}	2.2×10^{-11}	2×10^{-12}

which has a mean square value of

$$D_{\psi}(\tau) = \overline{\alpha^2}\,\tau^2 + D_{\phi}(\tau)$$

where the overbar denotes the statistical expectation. Let the average phase instability (or change in phase over a measurement of τ seconds) be denoted by $\delta\psi(\tau)/\omega_0\tau$, then

$$\frac{\delta\psi(\tau)}{\omega_0\tau} = \frac{\sqrt{\overline{\alpha^2}\,\tau^2 + D_{\phi}(\tau)}}{\omega_0\tau} . \tag{200}$$

There are several models for the $D_{\phi}(\tau)$ of an oscillator which characterize (1) RC-type frequency instabilities, (2) Gaussian-type frequency instabilities, (3) flicker-type instabilities, (4) perturbation noise, and (5) oscillator spur and vibration noise. For example, with RC-type frequency instabilities

$$D_{\phi}(\tau) = \sigma_{\dot{\phi}}^2\,\tau_0\{\tau + \tau_0[\exp(-\tau/\tau_0) - 1]\} ,$$

where $\sigma_{\dot{\phi}}$ is the rms frequency deviation of the oscillator and τ_0 is the correlation time. For short-term instability, $D_{\phi}(\tau)$ has an asymptote of

$$D_{\phi}(\tau) = \sigma_{\dot{\phi}}^2\,\tau^2 ; \qquad \tau/\tau_0 < 1.$$

Therefore, from (200),

$$\frac{\delta\psi(\tau)}{\omega_0\tau} = \frac{\sqrt{\overline{\alpha^2} + \sigma_{\dot{\phi}}^2}}{\omega_0\tau}$$

and the rms elapsed time error due to short-term instability is

$$\Delta T_{\psi} = 10^9\,\sqrt{\overline{\alpha^2} + \sigma_{\dot{\phi}}^2}\,\tau = 10^9\,f\tau ,$$

where ΔT_{ψ} is in nanoseconds, τ is in seconds, and $f = \sqrt{\overline{\alpha^2} + \sigma_{\dot{\phi}}^2}$ is given in Table 21 under short-term instability for 1 second averaging time. Note for this model of oscillator instability, the short-term instability for 0.1 second averaging time in Table 21 can be used when τ is less than 0.3 second.

9.0 SHUTTLE GPS INTERFACE CONTROL DOCUMENT

Because of the criticality of the Shuttle navigation function and because GPS navigation entails elements external to the Space Shuttle Transportion System (STS), it is necessary to establish an Interface Control Document (ICD) between the GPS system and the Shuttle. Examples of the external elements include the NDS Space Vehicle Navigation Subsystem and the PRN Navigation Assembly signal characteristics.

Such an ICD has been established for the conventional user system segment, which does not include the Space Shuttle or any other space-borne users of GPS. This ICD, MH08-00002-400, Space Vehicle Navigation Subsystem and NTS PRN Navigation Assembly/User System Segment and Monitor Station, is a valid starting point for the GPS/Shuttle ICD. It alone, however, is not sufficient to guarantee the succcessful utilization of GPS by the Shuttle. An example of one shortcoming is that this ICD specifies the GPS signal power level at the earth's surface but not at the orbital altitudes at which the Shuttle operates. The current ICD for earth-bound users reflects the fact that the GPS satellite antenna patterns are shaped to provide a maximum power density approximately uniformly over the earth's surface, with rapid fall-off beyond the edge of the earth. The Shuttle/GPS ICD must specify the equivalent "pointing loss" for several Shuttle orbital altitudes or must specify the Effective Isotropic Radiated Power (EIRP) versus angle of the satellite/earth centerline.

A preliminary outline of the Shuttle/GPS ICD is given in Table 22. This outline will be expanded and the ICD written according to the expanded version during the forthcoming follow-on contract.

Table 22. Preliminary Outline - Shuttle/GPS ICD

1.0	SCOPE
2.0	APPLICABLE DOCUMENTS
3.0	REQUIREMENTS
3.1	Interface Definition
3.1.1	GPS Satellite Navigation Subsystem
3.1.2	GPS Signal RF Characteristics
3.1.3	GPS Signal Baseband Characteristics
3.1.4	GPS Time
3.1.5	Space Shuttle Navigation Subsystem
3.2	Interface Identification
3.2.1	GPS System
3.2.2	Space Shuttle System
3.3	GPS Satellite Constellation Definition
3.3.1	Orbital Characteristics
3.3.2	Deployment Schedule
3.3.3	Maintenance/Replacement Schedule
3.4	Radio Frequency Characteristics
3.4.1	RF Signal Structure
3.4.2	Navigation Data Update
3.4.3	GPS Satellite Operating Modes
3.4.4	Frequency Plan
3.4.5	Out-of-Band Emissions
3.4.6	In-Band Spurious Emissions
3.4.7	Signal Coherence
3.4.8	Carrier Phase Noise
3.5	Code Waveform Characteristics
3.5.1	Pulse-to-Pulse Jitter
3.5.2	Incidental AM
3.6	Group Delay Variations
3.7	Timing Accuracy
3.8	Antenna Polarization
3.9	Shuttle Received RF Signal Levels
3.9.1	On-Orbit
3.9.1.1	L1 Navigation Signal
3.9.1.2	L2 Navigation Signal
3.9.2	In-Atmosphere
3.9.2.1	L1 Navigation Signal
3.9.2.2	L2 Navigation Signal
3.9.3	Pointing Loss Slope
3.10	Navigation Signal Structure
3.10.1	P Code Generation
3.10.2	C/A Code Generation
3.10.3	P Code Acquisition From C/A Code
3.11	Frequency Standard
3.11.1	Accuracy
3.11.2	Drift
3.12	Signal Data
3.12.1	Data Waveform Characteristics
3.12.2	Data Format Characteristics
3.12.3	Data Block Contents
3.13	GPS Denial of Accuracy
3.13.1	Algorithm
3.13.2	Shuttle Navigation Accuracy

REFERENCES

1. P. W. Nilsen. "Investigation and Evaluation of Shuttle/GPS Navigation System," Final Report (Contract NAS 9-15387A), Axiomatix Report No. R7710-3, October 15, 1977.

2. J. K. Holmes and C. C. Chen. "Acquisition Time Performance of PN Spread Spectrum Systems," IEEE Transactions on Communications (Special Issue on Spread Spectrum Communications), Vol. COM-25, No. 8, August 1977, pp. 778-784.

3. J. I. Marcum. "A Statistical Theory of Target Detection by Pulsed Radar: Mathematical Appendix," The Rand Corporation Report ASTIA AD 101882, July 1, 1948.

4. B. D. Trumpis. "Sequential Detection for the Ku-Band Despreader," TRW IOC, November 3, 1975.

5. J. H. Park, Jr. "An FM Detector for Low S/N," IEEE Transactions on Communication Technology, Vol. COM-18, April 1970, pp. 110-118.

6. W. C. Lindsey and M. K. Simon. "Optimum Design and Performance of Costas Receivers Containing Soft Bandpass Limiters," IEEE Transactions on Communications, Vol. COM-25, No. 8, August 1977, pp. 822-831.

7. W. C. Lindsey. Synchronization Systems in Communication and Control. Englewood Cliffs, N.J.: Prentice-Hall, Inc., 1972.

8. M. K. Simon and W. C. Lindsey. "Optimum Performance of Suppressed Carrier Receivers With Costas Loop Tracking," IEEE Transactions on Communications, Vol. COM-25, No. 2, February 1977, pp. 215-227.

APPENDIX A

MEASUREMENT OF TACAN TRANSMITTER PULSE SPECTRUM

The following is a description of the measurement performed by JSC of the TACAN pulse spectrum.

The TACAN used was a Hoffman AN/ARN84 operating on channel 26 (X mode) in the search mode (150 pulse pairs per second). The test equipment used is shown in Figures A-1 and A-2.

The transmit twin pulses were recorded as shown in Photograph A-1 using the test equipment configuration as shown in Figure A-1. The pulse jitter technique used for coding caused some synchronization problems but the pulses obtained are typical of those described in the TACAN literature.

Photograph A-2, the transmit spectrum, was obtained as shown in Figure A-2. The total of 63 dB attenuation was required in order to protect the spectrum analyzer from burnout. The photograph shows the main spectral component at 1150 MHz and no discernible component at the 1226 MHz region. Photograph A-3 is the same configuration as Photograph A-2 except that the baseline clipper control on the analyzer was turned to minimum. This caused the trace to bloom on the scope. The scope was readjusted to remove the bloom which caused the main component to fade and leave only the baseline noise as desired to enable seeing any small signals. The approximate frequency shown in the photograph was from 1130 to 1330 MHz. Scan time on Photograph A-2 was 2 seconds/division and 20 milliseconds/division for Photograph A-3. Amplitude was 10 dB/division.

Photograph A-4 is the spectrum of the transmit pulse with the peak approximately 60 dB above the baseline. Some asymmetry is noted but no explanation was found to cause this. The spectrum was expected to be symmetrical. Photograph A-5 is the same as Photograph A-4 except for removal of baseline clipping. Scan time was again 2 seconds and 20 milliseconds/division. Amplitude was 10 dB/division.

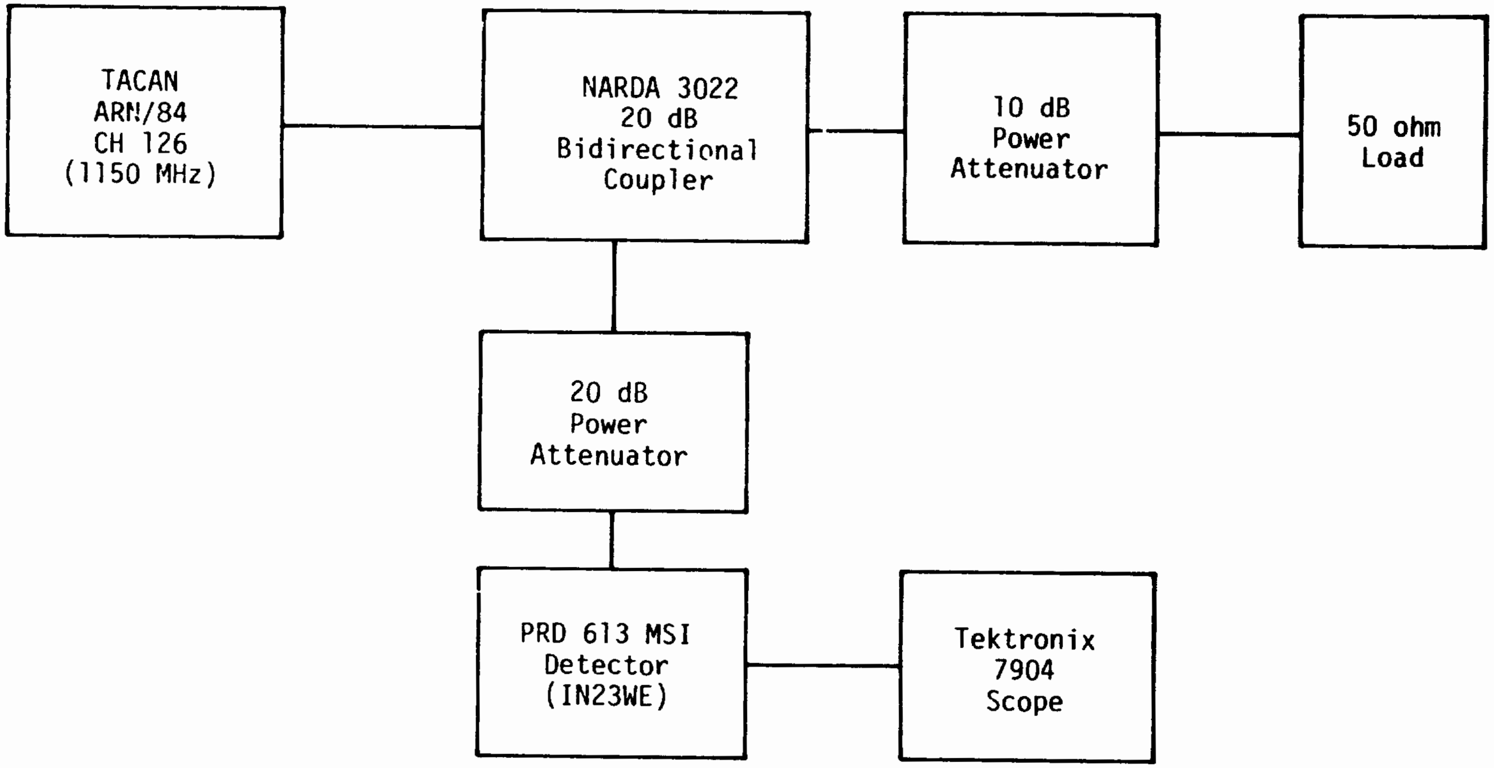

Figure A-1. Test Configuration for Obtaining Detected Pulse Photographs

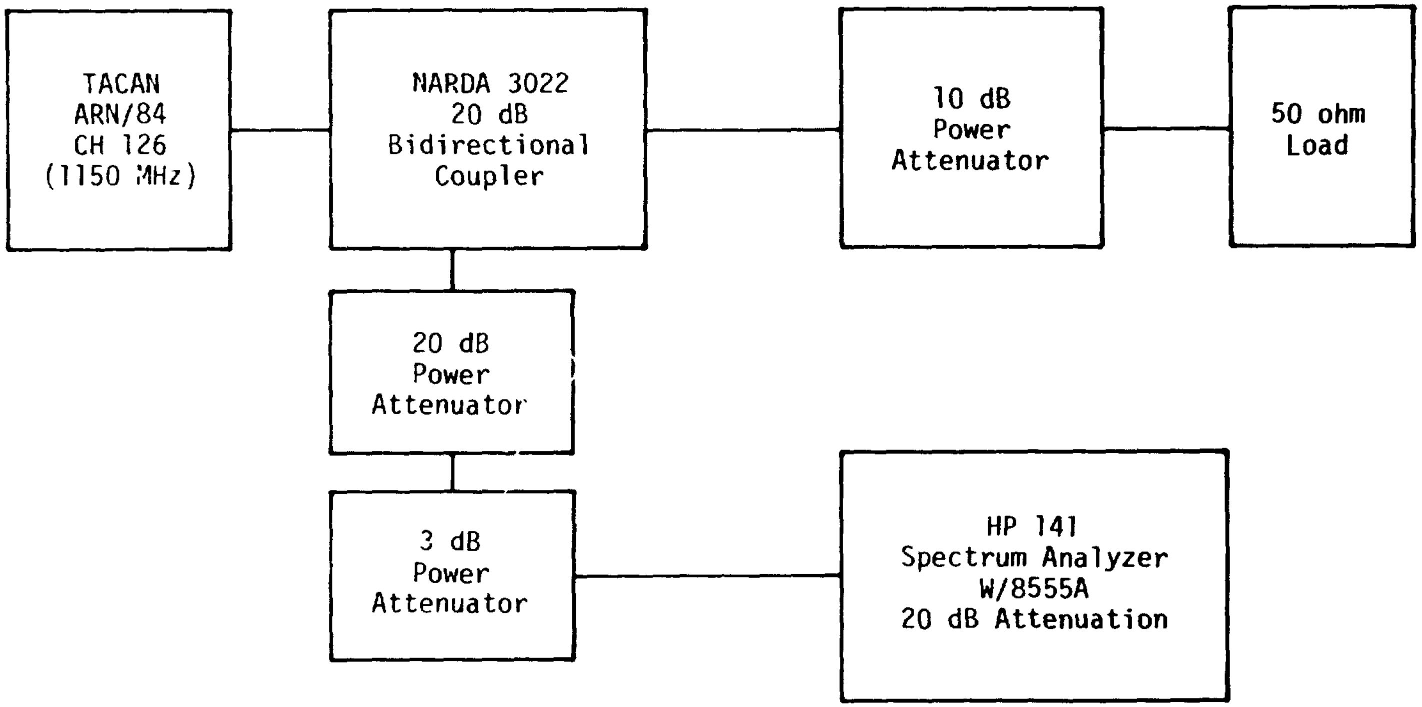

Bandwidth: 110 kHz
Scan: 0.5 MHz/division
Total Attenuation: 63 dB
Amplitude: 10 dB/division

Figure A-2. Test Configuration for Obtaining Spectrum Photographs

PHOTOGRAPH A-1. DETECTED TWIN TRANSMITTER PULSES

SWEEP 2 MICROSECONDS/DIVISION
AMPLITUDE 100 MILLIVOLTS/DIVISION

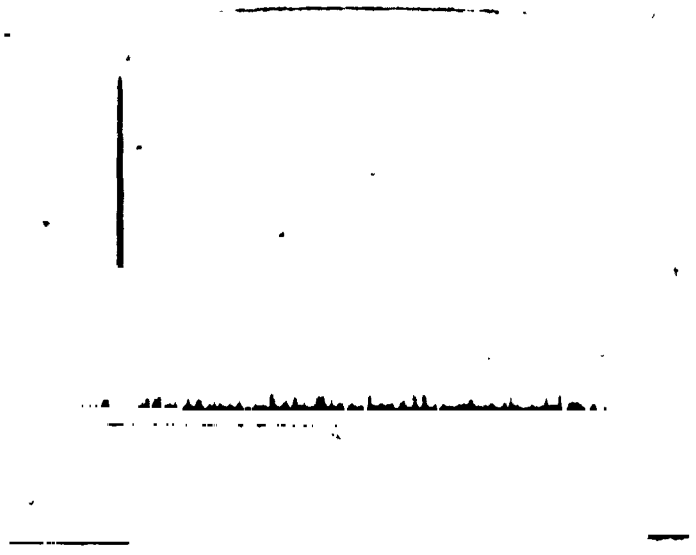

PHOTOGRAPH A-2. TRANSMIT SPECTRUM
SCAN 1130 MHz to 1330 MHz (20 MHz/DIV.)
AMPLITUDE 10 dB/DIV.
SCAN TIME 2 SEC/DIV.

PHOTOGRAPH A-3. TRANSMIT SPECTRUM
BASELINE CLIPPER MINIMUM
1130 MHz to 1330 MHz (20 MHz/DIV.)
AMPLITUDE 10 dB/DIV.
SCAN TIME 20 mSEC/DIV.

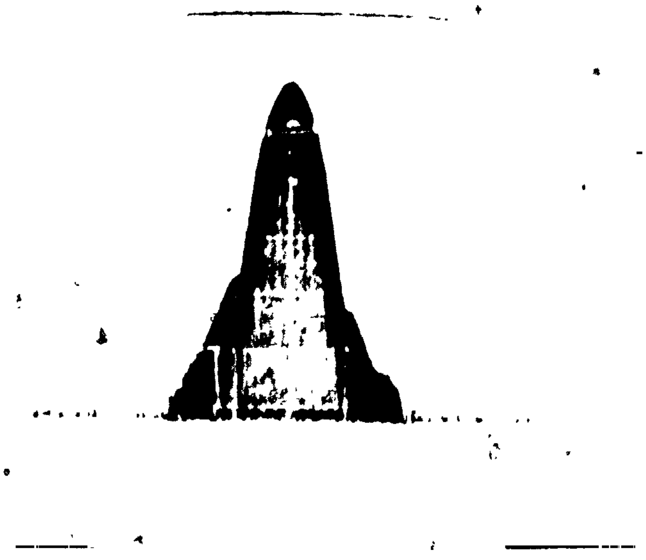

PHOTOGRAPH A-4. TRANSMIT SPECTRUM
BANDWIDTH 100 KHz
SCAN 0.5 MHz/DIV.
SCAN TIME 2 SEC/DIV.
AMPLITUDE 10 dB/DIV.

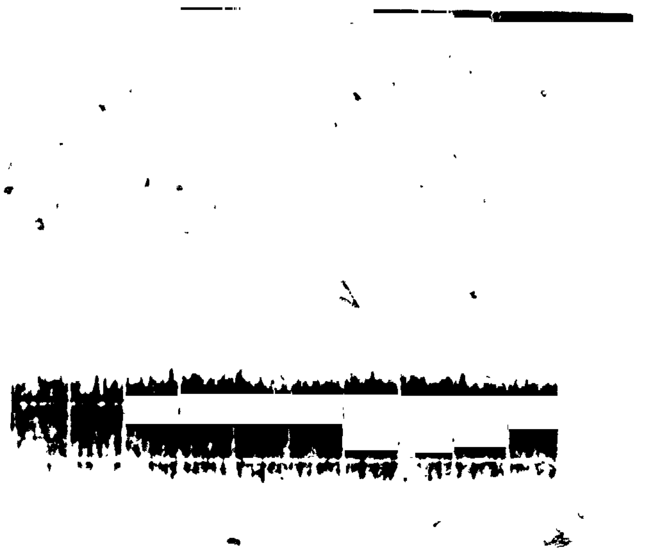

PHOTOGRAPH A-5. TRANSMIT SPECTRUM
BASELINE CLIPPER MINIMUM
BANDWIDTH 100 KHz
SCAN 0.5 MHz/DIV.
SCAN TIME 20 mSEC/DIV.
AMPLITUDE 10 dB/DIV.